

Weakly Coupled Oscillators in a Slowly Varying World

Youngmin Park*& Bard Ermentrout

Department of Mathematics
University of Pittsburgh
Pittsburgh PA 15260

February 23, 2016

Abstract

We extend the theory of weakly coupled oscillators to incorporate slowly varying inputs and parameters. We employ a combination of regular perturbation and an adiabatic approximation to derive equations for the phase-difference between a pair of oscillators. We apply this to the simple Hopf oscillator and then to a biophysical model. The latter represents the behavior of a neuron that is subject to slow modulation of a muscarinic current such as would occur during transient attention through cholinergic activation. Our method extends and simplifies the recent work of Kurebayashi [17] to include coupling. We apply the method to an all-to-all network and show that there is a waxing and waning of synchrony of modulated neurons.

Keywords Modulation - weak coupling - oscillators - Traub model - slowly varying parameters

1 Introduction

The theory of weakly coupled oscillators [8, 9, 16] has served very well as a predictor of the dynamics in networks of coupled neural oscillators (for a comprehensive review, see [24]). In the application of this theory, one generally assumes that, while the oscillators may have different intrinsic frequencies, these frequencies are fixed as are the uncoupled limit-cycle oscillators. However, more generally, local regions of the nervous system are constantly modulated by extrinsic inputs and by slow processes such as the accumulation of extracellular ions. Thus, synchronization and other properties are

*Corresponding author. Email yop6@pitt.edu

likely to change due to this modulation which can change the frequency, conductances, and even the synapses within an oscillatory network [21].

Neuronal modulators such as acetylcholine, norepinephrine [20], and dopamine [11] are known to alter the firing properties of neurons. These properties, in turn, could alter the synchronization behavior of neurons and more formally, the form that the weak coupling equations take. One of the key components to understanding synchronization of neuronal oscillators is the phase response curve (PRC) which describes how the phase of an oscillator is shifted by the timing of inputs. The PRC plays the key role in determining whether or not a pair of coupled neuronal oscillators will synchronize or not. In [26, 27], the authors directly demonstrated that cholinergic modulation of a cortical pyramidal neuron had a profound effect on the shape of the PRC. Acetylcholine is known to directly act on the so-called M-type potassium current and in [5], they showed how changing the strength of this current made a huge difference on the shape of the PRC as well as in the ability of synaptically coupled neurons to synchronize. Neuronal properties are also affected by the extracellular milieu, notably, concentration of extracellular potassium which can profoundly alter excitability of neurons [2]. Rubin et al [23] showed that the synchronization between two coupled neurons was strongly dependent on the mean concentration of extracellular potassium. Jeong and Gutkin [13] showed the changes in the reversal potential of GABAergic conductances changed the ability of neurons to synchronize; the reversal potential is mainly driven by extracellular chloride. Thus, since many neuromodulators as well as the ionic concentrations are constantly changing, it is important to see how this time varying environment alters the ability of neurons to synchronize.

In two recent papers Kurebayashi et al [17, 18], extended the notion of phase reduction to oscillators that are subject to large slowly varying parameters. They demonstrated that the evolution of the phase depended, not just on the instantaneous frequency of the oscillator, but, also on the rate of change of the slowly varying parameter. In this paper, we re-derive the phase equation in [17] by using the method of adiabatic invariance [14] (Chapter 12.1.2) and incorporate the slow variation of parameters into weak coupling of oscillators using the Fredholm alternative. Thus we have a theory to predict synchrony and antiphase along with stability, in the presence of a slowly varying parameter. Moreover, because we only assume the parameter to be slowly varying, our theory is shown to accurately predict phase differences with periodic, quasi-periodic, and stochastic slowly varying parameters.

We first derive the equations for the phases and the phase-differences for a pair of coupled oscillators that are subject to slow changes in a parameter. Next, we apply the theory to the Hopf oscillator (so-called $\lambda - \omega$ system, [15]) where all of the required functions for our analysis can be exactly derived. We then consider a biophysical Hodgkin-Huxley model for pyramidal neurons (the simplified “Traub” model [5]). This model includes

an M-type potassium current, so in our analysis and simulations, we allow the conductance to slowly change as a model for cholinergic modulation. We conclude with a discussion and contrast the results with fast modulation.

2 Methods

2.1 Weakly Coupled Oscillators With a Slowly Varying Parameter

We consider a pair of weakly coupled slowly-varying oscillators:

$$\begin{aligned}\frac{dX^a}{dt} &= F(X^a, q(\epsilon t)) + \epsilon G_a(X^b, X^a) \\ \frac{dX^b}{dt} &= F(X^b, q(\epsilon t)) + \epsilon G_b(X^a, X^b)\end{aligned}\quad (1)$$

where $0 < \epsilon \ll 1$ is a small parameter. We assume that the slowly varying parameter, q , lies in an interval $Q := [q^-, q^+]$ such that for each $q \in Q$, the system:

$$\frac{dX}{dt} = F(X, q)$$

has an asymptotically stable limit cycle with frequency $\omega(q)$. The period of the oscillators is just $T(q) = 2\pi/\omega(q)$. Thus, each of the two oscillators is modulated by a common slowly varying signal, $q(\epsilon t)$ that can alter the shape and frequency of the rhythm but does not destroy its existence. The functions $G_{a,b}$ represent the weak coupling between the two oscillators. If there is no modulation of the oscillations, then, we can regard equation (1) as a standard weakly coupled system. However, the slow modulation changes the dynamics and interactions in a way that we will now demonstrate. We point out that [17] derived the phase modulation for a single slowly varying oscillator using successive changes of variables and showed that the “naive” phase approximation was not valid. More precisely, the term $\beta(\tau)$ defined in equation (9) accounts for possibly large variations in the slowly varying parameter. Therefore, omitting this term (the “naive” approximation) from equations (7)–(8) results in a poor phase approximation in the case of a single forced oscillator. Here, we introduce a simpler way to derive the same equations using a standard adiabatic approximation [14], and extend the results to coupled oscillators. In the coupled oscillator case, the “naive” phase approximation is valid.

Clearly, there are two time scales in this problem, a slow time scale, $\tau = \epsilon t$ and a fast time scale, s that is related to t . To put everything on a similar fast time scale, we generally allow that

$$\frac{ds}{dt} = g(\tau, \epsilon)$$

and expand to get a relationship between s and t that is τ -dependent. However, we need only terms in the lowest order in the fast time scale, so we will simply cut to the chase and write $s = \omega(q)t$, so that the oscillators are all 2π -periodic in s . (For the time being, we have suppressed the implicit τ dependence of the fast time scale, by just putting the parameter q in the frequency, but, in fact, q is just shorthand notation for $q(\tau)$.)

Before continuing with the perturbation, we introduce some additional notation. Let $U_0(s, q)$ be the limit cycle solution to the uncoupled system

$$\omega(q) \partial U / \partial s = F(U, q), \quad (2)$$

and let $A(s, q) := D_U F(U_0, q)$ be the linearization of the uncoupled system evaluated at the limit cycle. By taking the derivative with respect to s on both sides of equation (2), we see that the linear equation

$$L(s, q)Y := \omega(q) \frac{\partial Y}{\partial s} - A(s, q)Y = 0 \quad (3)$$

has a periodic solution given by $\partial_s U_0(s, q)$ where the notation, ∂_s means differentiation with respect to the first component in U_0 . Associated with the set of 2π -periodic functions is an inner product defined as

$$\langle Y_1(s), Y_2(s) \rangle = \int_0^{2\pi} Y_1(s) \cdot Y_2(s) ds,$$

where $Y_1 \cdot Y_2$ is the standard Euclidean dot product. With this inner product, the linearized equation has a well-defined adjoint operator:

$$L^*(s, q)Y := \omega(q) \frac{\partial Y}{\partial s} + A^T(s, q)Y, \quad (4)$$

from which we attain the adjoint equation,

$$\omega(q) \frac{\partial Y^*}{\partial s} = -A^T(s, q)Y^*$$

where A^T is the transpose. There is a unique 2π -periodic solution to the adjoint equation, which we call $Z(s, q)$ such that

$$Z(s, q) \cdot \frac{\partial U_0(s, q)}{\partial s} = 1.$$

Finally, the linearization has the Fredholm alternative property [14]. That is, there is a 2π -periodic solution to:

$$L(s, q)Y = b(s) \quad (5)$$

where $b(s)$ is 2π -periodic and L is defined in (3) if and only if

$$\int_0^{2\pi} Z(s, q) \cdot b(s) ds = 0.$$

With these preliminaries defined, we are now ready to analyze weak coupling of slowly varying oscillators.

We assume that the solutions to equation (1) can be expressed in a series in ϵ and have the form

$$\begin{aligned} X^a(t, \epsilon) &= X_0^a(s, \tau) + \epsilon X_1^a(s, \tau) + \dots \\ X^b(t, \epsilon) &= X_0^b(s, \tau) + \epsilon X_1^b(s, \tau) + \dots. \end{aligned}$$

To lowest order, we must have

$$\omega(q(\tau)) \frac{\partial X_0^{a,b}(s, \tau)}{\partial s} = F(X_0^{a,b}(s, \tau), q(\tau)).$$

The 2π -periodic limit cycle solution to this problem is

$$X_0^{a,b}(s, \tau) = U_0(s + \theta^{a,b}(\tau), q(\tau))$$

where $\theta^{a,b}(\tau)$ are slowly varying arbitrary phase shifts due to the time-translation invariance of the limit cycle. Our goal is to now derive equations for the slow evolution of the phase. Using the chain rule, we see that $d/dt = \omega \partial/\partial s + \epsilon \partial/\partial \tau$. Thus, after a bit of rearranging, the next order equations are:

$$\begin{aligned} L(s, q(\tau)) X_1^a(s, \tau) &= -\partial_s U_0(s + \theta^a(\tau), q(\tau)) \frac{\partial \theta^a}{\partial \tau} \\ &\quad - \partial_q U_0(s + \theta^a(\tau), q(\tau)) \frac{dq}{\partial \tau} \\ &\quad + G_a[U_0(s + \theta^b(\tau), q(\tau)), U_0(s + \theta^a(\tau), q(\tau))], \end{aligned} \tag{6}$$

where $L(s, q(\tau))$ is defined by (3). There is a similar equation for $X_1^b(s, \tau)$. Finally, we see that this equation has the form of (5), so that there is a 2π -periodic solution if and only if the right-hand side is orthogonal to the adjoint. This leads to the following equations for the phases:

$$\frac{\partial \theta^a}{\partial \tau} = -\beta(\tau) + h_a(\theta^b - \theta^a, \tau) \tag{7}$$

$$\frac{\partial \theta^b}{\partial \tau} = -\beta(\tau) + h_b(\theta^a - \theta^b, \tau), \tag{8}$$

where,

$$\beta(\tau) = \int_0^{2\pi} Z(s, q(\tau)) \cdot \partial_q U_0(s, q(\tau)) \frac{\partial q}{\partial \tau} ds \tag{9}$$

$$h_{a,b}(\phi, \tau) = \int_0^{2\pi} Z(s, q(\tau)) \cdot G_{a,b}[U_0(s + \phi, q(\tau)), U_0(s, q(\tau))] ds. \tag{10}$$

The extra $\beta(\tau)$ term arises due to the fact that the parameter q is slowly varying. Notice in its definition through equation (9), that it is proportional

to the time derivative of $q(\tau)$. This is the term that [17] emphasized in their analysis. That is, we recover their results if we ignore coupling. We remark that the phase-interaction functions, $h_{a,b}(\cdot)$ are exactly those that would be obtained from standard weak-coupling theory with all parameters held fixed. In absence of coupling, the total phase evolves as

$$\theta(t) = \theta(0) + \omega(q(\tau))t - \epsilon \int_0^t \beta(\epsilon t') dt'.$$

If both oscillators are subject to the exact same slowly varying inputs, then the β term becomes irrelevant to their phase difference, $\phi := \theta^b - \theta^a$ which satisfies the simple scalar slowly varying equation [24]:

$$\frac{d\phi}{d\tau} = h_b(-\phi, \tau) - h_a(\phi, \tau) := G(\phi, \tau) \quad (11)$$

Equation (11) will be our main tool for comparing the phase reduced model to the full model. We remark that the interaction functions are τ -dependent, so that the reduced system for the phase-difference is no longer autonomous and we will not be able to write exact solutions. However, if $h_a = h_b$, then the right-hand side of equation (11) is, for each τ , an odd periodic function of ϕ , so that $\phi = 0, \pi$ will always be equilibrium points. That is $G(0, \tau) = G(\pi, \tau) = 0$ for all τ . In this symmetric case, we define H_{odd} to be the odd part of the function h_a .

2.2 Mode Truncation

In order to study the phase-reduced equations, we need to get formulae for the τ -dependent interaction functions, $h_{a,b}$. For our first application of the method, these functions are explicitly computable since the oscillation and the adjoint are simple sine and cosine functions. However, for the neural model that we also study (and which gives more interesting results), we need to somehow approximate the required slowly varying functions. To this end, we use XPPAUT [4] to numerically compute the adjoint and interaction functions. For each interaction function we perform a mode truncation (that is, we keep just a few of the Fourier terms). We finish the approximation by deriving a q -dependent equation for the coefficients of the Fourier series expansion; generally piecewise-linear. This approximation serves particularly well for our problem because only two sine coefficients are required to preserve the change in synchrony, bistability between synchrony and antiphase (π -phase difference), and other interesting phenomena.

3 Results

We apply our theory to the Lambda-Omega system and a modified Traub model with adaptation. For each model, we consider three types of slowly

varying parameters, which we briefly discuss before delving into the details of each model. We remark that all figure code and relevant data files are available on github at https://github.com/youngmp/park_and_ermontout_2016

3.1 Slowly Varying Parameters

The slowly varying parameter, $q(\tau)$, is explicitly written as three types of slowly varying parameters: periodic (q_p), quasi-periodic (q_{qp}), and stochastic (q_s):

$$\begin{aligned} q_p(\tau) &:= q_0 + q_1 \cos(f\tau), \\ q_{qp}(\tau) &:= q_0 + (q_1/2)(\cos(f\tau) + \cos(f\tau\sqrt{2})), \\ q_s(\tau) &:= q_0 + q_1 z(\tau). \end{aligned} \quad (12)$$

The terms q_i , f , and ε depend on the system. For the Lambda-Omega system, we choose $f = 1$ and various combinations of q_0 and q_1 because the choice of q_i affects the asymptotic dynamics. Surveying multiple values of q_i provides a more complete demonstration of the dynamics and the accuracy of our theory. For the Traub model, we chose by default $q_0 = 0.3$, $q_1 = 0.2$, and $f = 5$ unless otherwise stated (as in figure 8). The default choice of parameters represents a biophysically realistic parameter range, while the slightly different parameter choice in figure 8 demonstrates the accuracy of our theory when we avoid slow stability changes.

The noisy parameter, z , is an Ornstein-Uhlenbeck (OU) process satisfying the stochastic differential equation

$$\mu dz = -z dt + \sqrt{\mu} dW,$$

where $\mu = 1000$. The raw random noise data is normalized so that

$$z(\tau) \in [-1, 1], \quad \forall \tau,$$

and this data is used in all noisy simulations. The OU data may be reproduced by using XPP seeds 1–4.

3.2 Lambda-Omega System

We first apply our result to the $\lambda-\omega$ system [15] with weak diffusive coupling,

$$\begin{pmatrix} \dot{x}_j \\ \dot{y}_j \end{pmatrix} = \begin{pmatrix} \lambda(r_j) & -\omega(r_j, q(\tau)) \\ \omega(r_j, q(\tau)) & \lambda(r_j) \end{pmatrix} \begin{pmatrix} x_j \\ y_j \end{pmatrix} + \varepsilon \begin{pmatrix} 1 & -\kappa \\ \kappa & 1 \end{pmatrix} \begin{pmatrix} x_k - x_j \\ y_k - y_j \end{pmatrix} \quad (13)$$

where $j, k = 1, 2$ and $k \neq j$; $r_j := \sqrt{x_j^2 + y_j^2}$; and

$$\begin{aligned} \lambda(r) &= 1 - r^2 \\ \omega(r, q) &= 1 + q(r^2 - 1). \end{aligned}$$

When $\varepsilon = 0$, equation (13) is equivalent to the Hopf oscillator in polar coordinates,

$$\begin{aligned}\dot{r}_j &= r_j \lambda(r_j) \\ \dot{\theta}_j &= \omega(r_j, q(\tau)).\end{aligned}$$

One can verify the limit cycle for uncoupled system is

$$U_0(s, \tau) = [\cos(s), \sin(s)]^T,$$

and the solution to the adjoint equation (the iPRC) is

$$Z(t) = [q(\tau) \cos(t) - \sin(t), q(\tau) \sin(t) + \cos(t)]^T.$$

Finally, Equation (11) for the $\lambda - \omega$ system is

$$\frac{d\phi}{d\tau} = 2(\kappa q(\tau) - 1) \sin(\phi). \quad (14)$$

Note that synchrony ($\phi = 0$) is indeed a fixed point of Eq. 14. For a brief stability analysis, we note that equation (14) is a separable equation and solve for an implicit solution the differential equation:

$$\tan(\phi/2) = c \exp \left[\int_0^\tau (\kappa q(s) - 1) ds \right]. \quad (15)$$

We can write the inside of the exponential as $\tau Q(\tau)$ where $Q(\tau) = (1/\tau) \int_0^\tau [\kappa q(s) - 1] ds$. $Q(\tau)$ is the running average of the integrand. Since the integrand is bounded and continuous, the limit of $Q(\tau)$ exists as $\tau \rightarrow \infty$. If this limit is positive then the exponential diverges to $+\infty$ and the phase $\phi \rightarrow \pm\pi$. Similarly, if the limit is negative, then the exponential goes to zero and ϕ converges to 0 as well.

Figure 1 shows the result of simulating equation (13) for different functions of $q(\tau)$. In the left column (labeled a,c,e) the mean value of $q(\tau)$ is less than 1, so that we expect that the phase differences will go to synchrony. In the right panels, the mean value of $q(\tau) > 1$ so that the theory predicts that phase-differences will go to π . This is clearly evident from the simulations of the full model. Furthermore, the approach to equilibrium predicted by the phase model is almost identical to that of the full simulations. There is very little error even in the stochastic cases (panels e,f). Even though this is a highly nonlinear system, the system goes to the stable state that is appropriate for the *average* of the slowly varying parameter. If we break the homogeneity, then the dynamics is more complex and interesting.

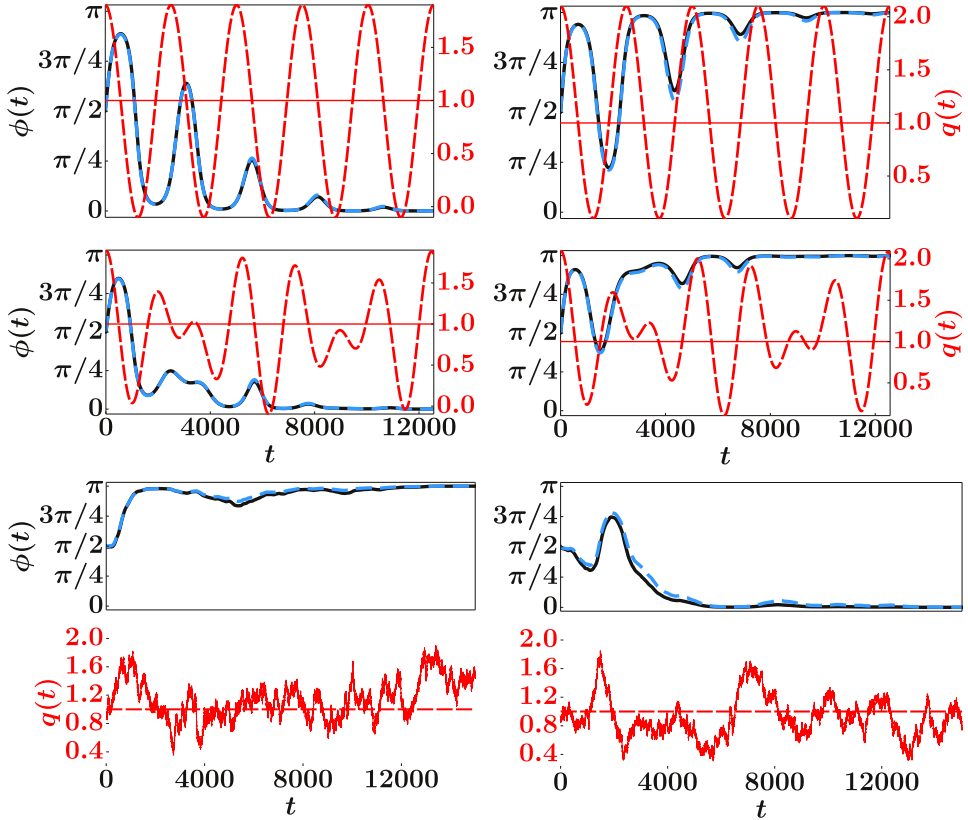


Figure 1: Periodic ((a),(b)), quasi-periodic ((c),(d)) and stochastic ((e),(f)) slowly varying parameters. The phase difference $\phi = \theta_2 - \theta_1$ theory (light blue dashed line) is plotted on top of experiment (black solid line). The slow periodic parameter is shown as a dashed red line. The horizontal line represents the parameter value q at which there is onset or offset of synchrony. For all subfigures, $\varepsilon = 0.0025$, $f = \kappa = q_1 = 1$. (a) Periodic, $q_0 = 0.9$, $\mathbb{E}[q] < 1$. (b) Periodic, $q_0 = 1.1$, $\mathbb{E}[q] > 1$. (c) Quasi-periodic, $q_0 = 0.9$, $\mathbb{E}[q] < 1$. (d) Quasi-periodic, $q_0 = 1.1$, $\mathbb{E}[q] > 1$. (e) Stochastic (OU), $q_0 = 0.85$, $\mathbb{E}[q] = 0.913$, XPP seed 2. (f) Stochastic (OU), $q_0 = 0.9$, $\mathbb{E}[q] = 1.145$, XPP seed 1.

Heterogeneities.

So far, the model derivation assumes that both oscillators are identical. However, in general, this will not necessarily be the case. If the differences are $O(\varepsilon)$ (that is, small) then we will get some additional terms in the phase equations. To account for this, in general, we add terms to equation (1) of the form:

$$\varepsilon f_{a,b}(X^{a,b}, \tau) \quad (16)$$

where we could also include some τ -dependence in the heterogeneity. For example, in the $\lambda - \omega$ system, we could set

$$\omega_{a,b}(r, q) = 1 + q(\tau)(r^2 - 1) + \epsilon[d_{a,b} + c_{a,b}(\tau)(r^2 - 1)]$$

where the subscripts refer again to the two oscillators. Here, the parameters $d_{a,b}$ are just constants that affect the baseline frequency and $c_{a,b}(\tau)$ are modulatory. With the addition of the terms (16), the phase equations we get are like equations (7-8) but have additional terms:

$$\begin{aligned}\frac{\partial \theta^a}{\partial \tau} &= -\beta(\tau) + \eta_a(\tau) + h_a(\theta^b - \theta^a, \tau) \\ \frac{\partial \theta^b}{\partial \tau} &= -\beta(\tau) + \eta_b(\tau) + h_b(\theta^a - \theta^b, \tau),\end{aligned}$$

where

$$\eta_{a,b}(\tau) = \int_0^{2\pi} Z(s, q(\tau)) \cdot f_{a,b}(U_0(s, q(\tau)), \tau) ds.$$

Subtracting the two equations yields the more general phase equation with heterogeneities:

$$\frac{d\phi}{d\tau} = \eta_b(\tau) - \eta_a(\tau) + h_b(-\phi, \tau) - h_a(\phi, \tau) := G(\phi, \tau). \quad (17)$$

We have still eliminated the common $O(1)$ slow variation $\beta(\tau)$, but the explicit heterogeneities appear through the differences $\eta_b(\tau) - \eta_a(\tau)$.

With this extension, we now alter the simple model by introducing a small frequency difference in the oscillators. For oscillator 2, we replace $\omega(r, q) = 1 + q(1 - r^2)$ with $\omega(r, q) = 1 + \epsilon d + q(1 - r^2)$, so that in absence of coupling, there is an order ϵ frequency difference, ϵd . In this case the equation for ϕ becomes

$$\frac{d\phi}{d\tau} = d + 2(\kappa q(\tau) - 1) \sin(\phi). \quad (18)$$

This means that $\phi(\tau)$ will no longer generally approach a steady state. In figure 2 we show two simulations with different values of ϵ when there is a slight difference in frequency. For $\epsilon = 0.025$, the solutions match for most of the time, but there are places in each segment, where the solutions are about π out of phase. On the other hand, when we reduce ϵ by factor of 10, the solutions to the full model and the phase model are indistinguishable.

As the effects of heterogeneities are rather interesting, even in this simple case, we will now examine equation (18) in more detail in order to explain the behavior in figure 2. We can rewrite equation (18) as a system with the time rescaled:

$$\begin{aligned}\phi' &= (d + 2(q(s) - 1) \sin \phi)/f \\ s' &= 1.\end{aligned}$$

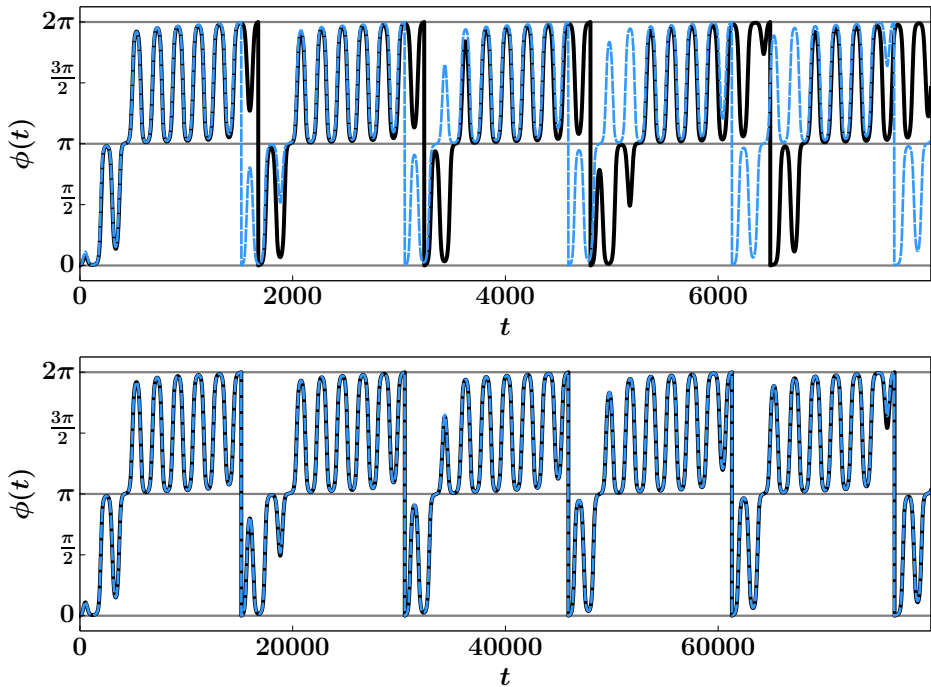


Figure 2: The effects of inhomogeneity on slowly modulated solutions. The slowly varying parameter is chosen to be periodic with $q_0 = 1.1, q_1 = 2, f = 1.3, d = 0.05, \kappa = 1$. (a) $\epsilon = 0.025$ (b) $\epsilon = 0.0025$. Black is the full model and blue dashed is the phase-reduced model. The solid gray lines at $\phi(t) = 0 \equiv 2\pi$ ($\phi(t) = \pi$) represent synchrony (anti-phase).

This is an equation on the torus and so the behavior is fairly restricted; in particular, the ratio $\rho = \lim_{\tau \rightarrow \infty} \phi/\tau$, called the rotation number is a continuous function of the parameters. We find three different behaviors as the inhomogeneity d and the frequency f vary. Figure 3 shows the behavior as these parameters are varied. In the upper left part of the diagram (high frequency), above the red curve, $\phi(\tau)$ has a winding number of 0. That is, $\phi(\tau + 2\pi) = \phi(\tau)$. This means that the phase-difference, ϕ between the two oscillators is bounded between two values and one oscillator is consistently ahead of the other. In the lower right part of the diagram (low frequency), $\phi(\tau + 2\pi) = \phi(\tau) + 2\pi$, that is, ϕ has winding number 1. This means that the phase-difference between the two neurons stays close to 0 for about half a cycle and close to π for the other half and makes these switches rapidly and periodically; it does not get “stuck” at synchrony or anti-phase. Finally, the middle region (and also the choice used in figure 2) shows that the phase makes rapid transition, first between π and 2π and then between π and 0. This explains the switching back and forth observed in figure 2. In sum, heterogeneity (even in the simplest form) can add good deal of complexity to the dynamics.

3.3 Traub Model with Adaptation

The membrane potential dynamics of the Traub model, V , satisfies

$$\begin{aligned} C\dot{V} &= -g_{Na}m^3h(V - E_{Na}) - (g_kn^4 + q(\tau)w)(V - E_k) - g_l(V - E_l) + I \\ &\equiv f(V, q(\tau)), \end{aligned} \tag{19}$$

where $q(\tau)$ is the slowly varying parameter with $q \in [0.1, 0.5]$, $q_0 = 0.3$, $q_1 = 0.2$, and gating variables n, m, h, w satisfying

$$\begin{aligned} \dot{n} &= a_n(V)(1 - n) - b_n(V)n, \\ \dot{m} &= a_m(V)(1 - m) - b_m(V)m, \\ \dot{h} &= a_h(V)(1 - h) - b_h(V)h, \\ \dot{w} &= (w_\infty(V) - w)/t_w(V). \end{aligned}$$

We introduce weak coupling by adding a synaptic conductance

$$\begin{aligned} \frac{dV_1}{dt} &= f(V_1, q(\tau)) + \varepsilon g s_2(E_{syn} - V_1), \\ \frac{dV_2}{dt} &= f(V_2, q(\tau)) + \varepsilon g s_1(E_{syn} - V_2), \end{aligned}$$

where s_i is the synaptic conductance of V_i and satisfies

$$\dot{s}_i = \alpha(V_i)(1 - s_i) - s_i/\tau_s.$$

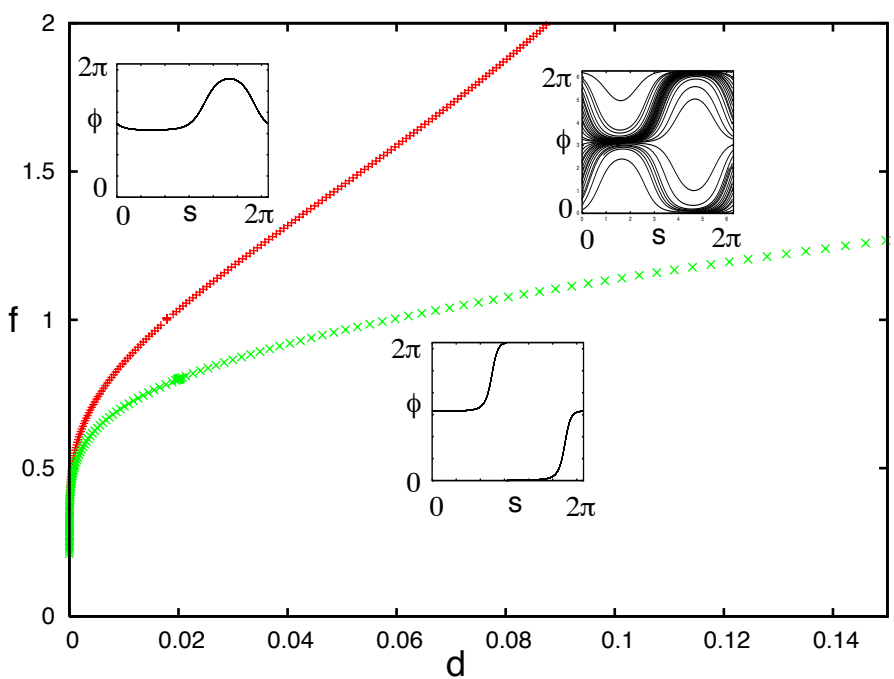


Figure 3: The behavior of equation (18) for periodic modulation as a function of the homogeneity, d and the modulation frequency, f . Green points show the border for $1 : 1$ locking; red points show the border for $0 : 1$ locking and between these are mixed solutions. Typical phase-planes are shown in each region.

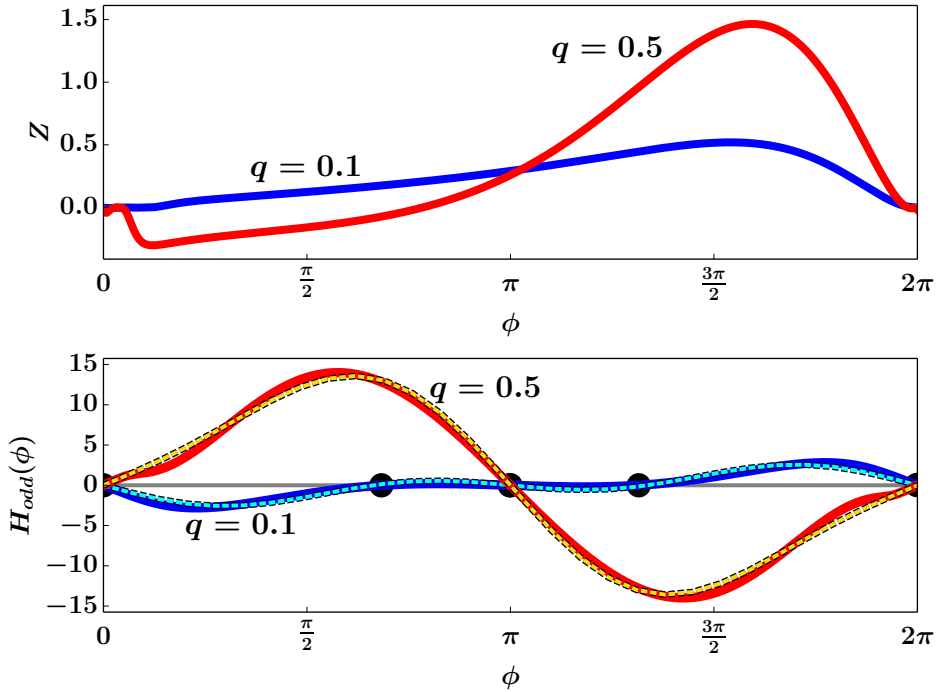


Figure 4: The Traub model (equation (19)) for two fixed values of q , the M-type potassium current. (a) the adjoints for $q = 0.1$ and $q = 0.5$; (b) The odd part of the interaction functions for $q = 0.1, 0.5$ (thick lines) and two-term sine fit (thin dashed lines) of $H_{odd}(\phi)$. Zero crossings in (b) are denoted by black circles.

Here $\alpha(V) = 4/(1 + \exp(-v/5))$ [29]. Adaptation in this model is controlled by the magnitude of the M -type potassium current. This low-threshold, slow current can drastically affect the dynamics of the Traub model [5] changing it from Class I excitable (oscillation arises via a saddle-node infinite cycle or SNIC) to class II excitable (oscillation arises via a sub-critical Hopf bifurcation). Because of that change, the adjoint, $Z(t)$ can also drastically change [1, 6] and thus, the interaction function will also be strongly affected. Biologically, this current is quite important since it is altered by acetylcholine, a neuromodulator. Thus, since neuromodulators tend to operate at much slower time scales than the firing rates of neurons, the slow alteration of the M -type potassium current is an ideal example of the methods we have developed in this paper.

Figure 4 shows the results of a numerical computation of the adjoint and the odd part of the interaction function. For small values of the M-current ($q = 0.1$) the adjoint (a) is almost strictly positive which is typical for so-called Class I excitable systems where the periodic orbit arises as a SNIC.

On the lower panel (b) we see that the $H_{odd}(\phi)$ is small and that synchrony is unstable. (Recall that the phase model satisfies, $\phi' = -2H_{odd}(\phi)$, so that a negative (positive) slope at an equilibrium is unstable (stable).) Anti-phase ($\phi = \pi$) is also unstable, but there are two stable fixed points that are near anti-phase. When there is sufficient M-current ($q = 0.5$), the adjoint has a large negative lobe right after the spike. This qualitative change in the shape of the adjoint leads to the stabilization of the synchronous state (panel b). Thus, as q is varied from a low to high value, we expect that the phase-difference will move toward synchrony (at high values) and away from synchrony (at lower values). Panel b also shows that a two-term sine approximation is reasonable and captures the qualitative (and to some extent, quantitative) shape of the functions. In particular, the full $H_{odd}(\phi)$ and the two-term sine approximation have the same equilibrium point properties. For this reason, we make a simple linear interpolation using a two term sine expansion of the interaction as q slowly varies. The approximation is thus:

$$-2H_{odd} \approx 2(b_1(q(\tau)) \sin(\phi) + b_2(q(\tau)) \sin(2\phi)),$$

where a linear approximation to $b_i(q)$ passing through the points $(0.1, b_i(0.1))$ and $(0.3, b_i(0.3))$ predicts onset and offset of synchrony sufficiently well:

$$b_i(q) = 5(\hat{b}_i(0.3) - \hat{b}_i(0.1))q + 1.5\hat{b}_i(0.1) - 0.5\hat{b}_i(0.3), \quad i = 1, 2.$$

The number represented by $\hat{b}_i(x)$ is the actual coefficient value at $q = x$ (see section 6.1).

In order to compare the slowly varying phase model to the full model, we need a way to extract the phase from the full model. For the simple $\lambda - \omega$ model, we could get the exact phase since the limit cycle is circle with a constant angular velocity. One method that is commonly used is to apply a Hilbert transform to the voltage and then extract the phase from this. However, for the Traub model (and, in fact, any model), we have more than just the voltage, so we can extract an approximate phase by picking a point on the unperturbed limit cycle that is closest to the point whose phase we wish to determine. (This is a fairly crude approximation; ideally, we would determine which isochron the point lies on by integrating the initial data forward for several periods and then matching the point. This method is very time consuming [3], so we have opted for the simpler approximation.) Figure 5 shows how this is done. We take the (V, n) coordinates of the simulation and find the value of (V, n) on the projected limit cycle that is closest in distance to the point on the actual trajectory. Since the voltage (V) spans a region of about 150 and the recovery (n) spans values between 0 and 1, we scale the distance metric accordingly. We compute the variance of $V_0(t), n_0(t)$ over one cycle of the unperturbed limit cycle, call these (σ_V^2, σ_n^2) . Thus the distance is:

$$\text{dist}(\Delta V, \Delta n) := \sqrt{(\Delta V)^2/\sigma_V^2 + (\Delta n)^2/\sigma_n^2}$$

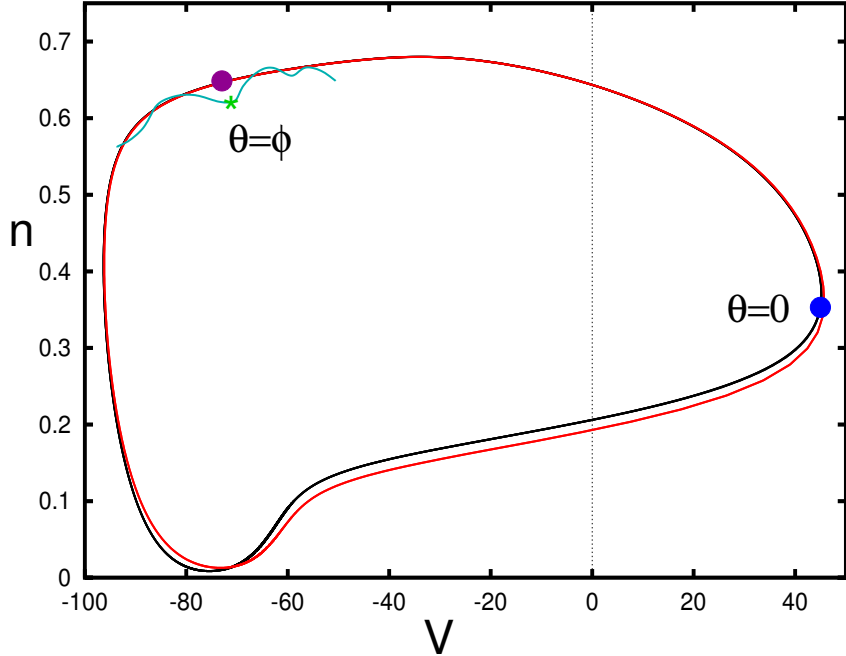


Figure 5: How the phase is extracted. A trajectory in green is shown near the limit cycle (red, for $q = 0.1$). The point (asterisk) on the trajectory is closest to the magenta point on the limit cycle which has phase ϕ , so we assign this phase. The black curve is the projection of the limit cycle for $q = 0.5$.

We define the phase of a point $(V(t), n(t))$ to be the value ϕ that minimizes:

$$\text{dist}(V(t) - V_0(\phi T/(2\pi)), n(t) - n_0(\phi T/(2\pi))),$$

where T is the natural period of the unperturbed limit cycle. We pick the comparison limit cycle (V_0, n_0) for a fixed value of the slowly varying parameter that is the mean value. However, as the figure shows, the phase portrait is very similar for two different values of q . As we will see later, this method produces a very reasonable approximation of the phase.

The next three figures compare the approximated phase model with the approximated phase extracted from the full model. That is, there are several levels of approximation to compare the theory to the full model. As described above, we approximate the function $G(\phi, \tau)$ in equation (11) by two sine terms whose coefficients are τ -dependent (cf Figure 4b). We apply the same slowly varying function for the conductance of the adaptation current to get the τ -dependence for the phase model. We extract the approximate phase-difference from the full model and compare the result with

the phase-difference derived from equation (11). Figure 6 shows the result of letting q vary periodically in time; the period is 5 seconds. The dashed red curves show the modulation and the red line shows the mean value. The light blue curve is the phase-difference as predicted by equation (11) and the black dots are the instantaneous approximate phase-differences from the model equations. Each dot represents the phase value at approximately 1/300 of one period. Because the period of the oscillation varies from 12.65s to 24.6s as a function of the slowly varying parameter, we can not give a precise total number of cycles. However, based on the total times one oscillator passes through zero phase, we estimate that there are 245 total cycles.

On the falling phase of the modulation (say, $t = 2.5 - 5$, $t = 8 - 10$, etc) the phase model and the full model agree very closely. On the rising phase, the reduced system lags the full system by quite a bit. Since both the rising and falling parts of the stimulus include all ranges of q , this difference cannot be due to a bad approximation of the interaction functions. As we noted above, the synchronous solution is a fixed point and for a range of q , it is attracting. Because synchrony is a fixed point and we are slowly changing from stable to unstable, there is great sensitivity at the transition. Small changes (such as ignoring small higher order terms in the perturbation) can have drastic effects on the “jump-up” time as synchrony loses stability. This is an example of a slow passage through a bifurcation [19]. To see what we mean here, we simulate the phase-model with the periodic stimulus and perturb the phase-difference, ϕ by slightly increasing it when it is close to 0. Figure 7 shows the result of such a manipulation. By increasing $\phi(t = 164)$ from, say, 10^{-14} to 10^{-4} (this is still an order of magnitude smaller than the ϵ used in the simulations), we can advance the “jump-up” time by almost an eighth of the cycle. The inset of the figure shows that $d\phi/dt$ is very small at this point. For this reason, we can expect that the main error will be on the up-jump since ϕ has to escape from the equilibrium point at zero. We will see similar, although less drastic, effects in the subsequent comparisons. By reducing the range of the slow parameter so that it is never close to the value for which synchrony is an attractor, we can do a much better job of tracking the phase-difference through the reduced model. Figure 8 shows an example where the modulated adaptation never gets to a region where synchrony is stable. In this case, the phase-difference for the phase-reduced model never gets close to 0 and the modulation stays away from any bifurcation points.

Figure 9 is similar to figure 6, except that the modulation is quasi-periodic. As with the periodic modulation, the phase model follows the full model quite closely once the system jumps away from the synchronous equilibrium. However, like the periodic case, the phase model has a delayed jump-up from synchrony relative to the full model; this is especially evident at $t \approx 25$.

Finally, in Figure 10, we use a slowly varying stochastic signal that is generated by an Ornstein-Uhlenbeck process and then rescaled so that the

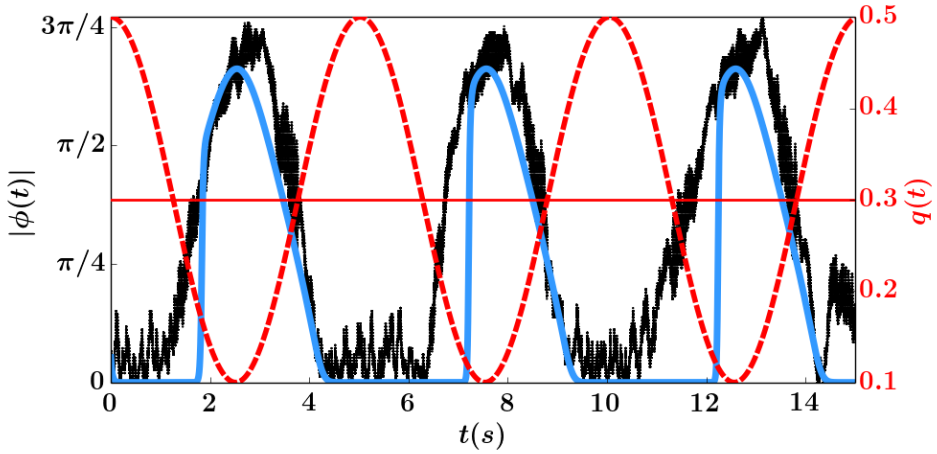


Figure 6: Periodic slowly varying parameter. Absolute value of phase difference $|\phi| = |\theta_2 - \theta_1| \in [0, 2\pi]$ theory (light blue) vs numerics (black dots). The slow periodic parameter is shown as a dashed red line. The horizontal line represents the parameter value q at which there is onset or offset of synchrony. $\varepsilon = 0.0025$, $f = 5$. 245 cycles.

range is $[-1, 1]$. As in figures 6 and 9, the phase model does a fairly good job of tracking the full model. Similarly, the jump up from synchrony is often delayed (especially evident for $t \in [2.5, 4]$) as was the case in all the previous simulations.

The slowly modulated interaction function works well in spite of the many approximations that we have made in the biophysical model.

3.4 Networks and synchrony

The methods we have described have, so far, been applied only to two coupled oscillators. There is no reason why we cannot apply them to networks as well. In this case, it is interesting to consider the idea of global synchronization in the presence of modulation. Here we consider (for simplicity) a population of N (we take $N = 51$, here) globally coupled neurons that are subject to slow modulation of the M -current as in the previous sections. We weakly couple the Traub model neurons with excitatory coupling and slow periodic modulation of the adaptation. Coupling is all-all and divided by the total number of neurons. Thus, each includes the synaptic current, $I_{syn} = g_{syn}s_{tot}(t)(V - E_{syn})$, where

$$s_{tot}(t) = \frac{1}{51} \sum_{j=0}^{50} s_j(t) \quad (20)$$

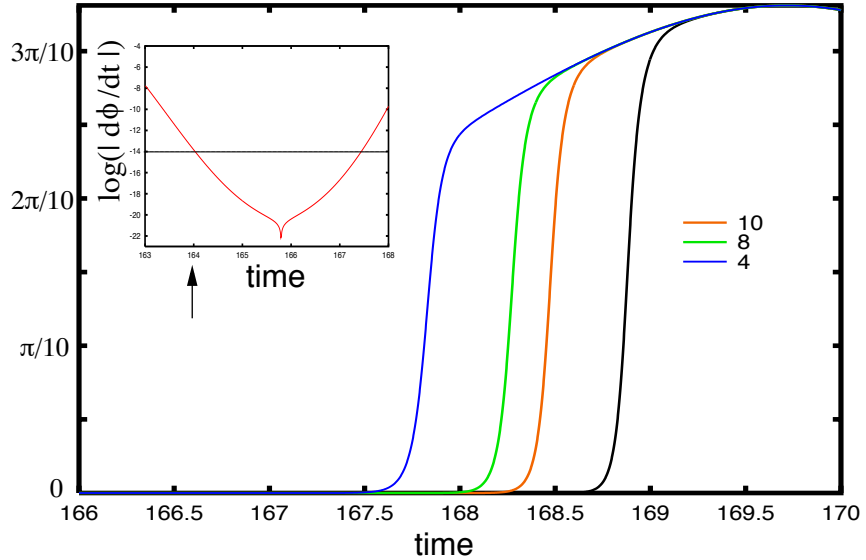


Figure 7: Small perturbations of the phase model near the transition. At $t = 164$, the value of ϕ is increased for 10^{-14} to $10^{-10}, 10^{-8}, 10^{-4}$ (red,green,blue), leading to an earlier jump-up time. Inset shows the log of $d\phi/dt$.

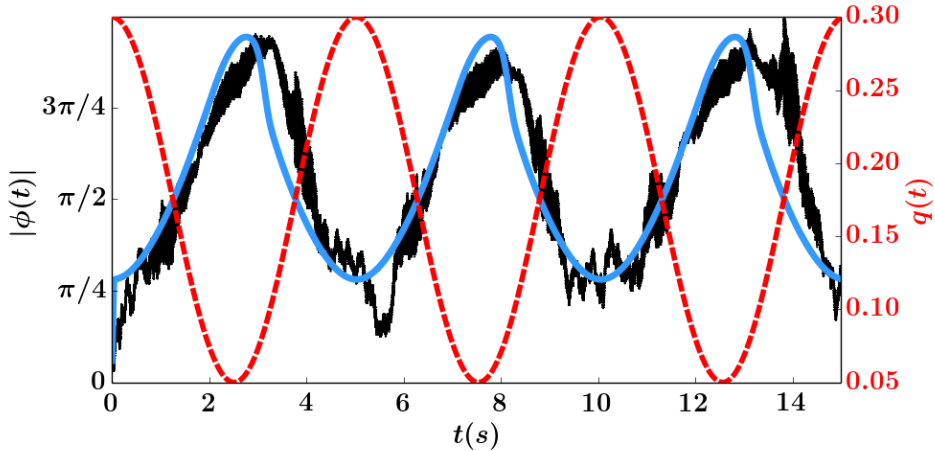


Figure 8: Periodic slowly varying parameter. Absolute value of phase difference $|\phi| = |\theta_2 - \theta_1| \in [0, 2\pi]$ theory (light blue) vs numerics (black dots). The slow periodic parameter is shown as a dashed red line. The slowly varying parameter constants are $q_0 = 0.175, q_1 = 0.125, \varepsilon = 0.0025, f = 5$. 219 cycles.

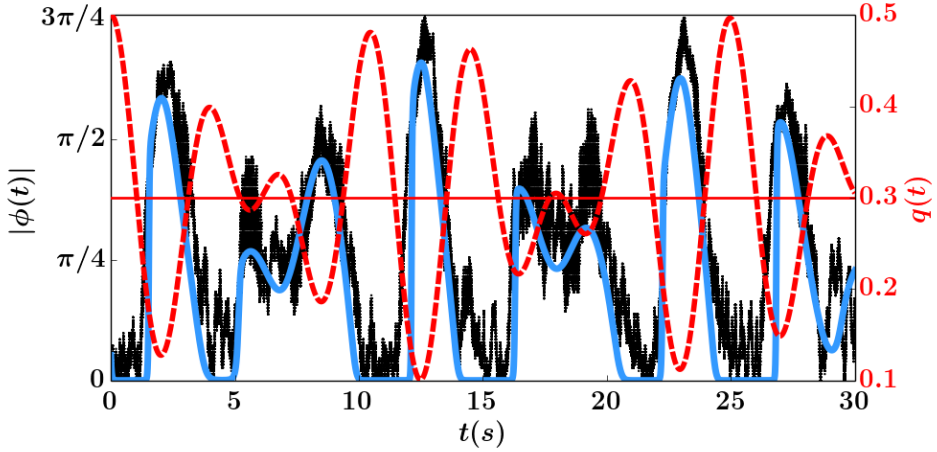


Figure 9: Quasi-periodic slowly varying parameter. The absolute value of phase difference $|\phi| = |\theta_2 - \theta_1| \in [0, 2\pi)$ in theory (light blue) vs numerics (black dots). The quasi-periodic parameter is shown as a dashed red line. $\varepsilon = 0.0025$, $f = 5$. 444 cycles.

and $s_j(t)$ are the individual synaptic gating variables for each neuron. Figure 11 shows the result of the simulation. As a surrogate for, say, the local field potential, we look at the total voltage of all the oscillators, $V_{tot} = (1/N) \sum_j V_j(t)$. Panel A shows the full picture of $V_{tot}(t)$ over 12 seconds. It is difficult to see the synchronization, but can be roughly judged by looking at the variance of V_{tot} : larger variance means greater synchrony. (If the oscillators were completely asynchronous, their sum would be close to a constant and so the variance of the sum will be small. If they are completely synchronized, then the variance of the sum will be large as the voltage swings over a 150 mV range.) To better illustrate this point, we have also computed the spectrogram (panel B) over this period of time. Notice the large red band that starts at the peak of $q(t)$ and tails off as $q(t)$ tends to zero. Higher bands represent harmonics of the oscillations. This panel also illustrates the dramatic effect that adaptation has on the frequency of the rhythm which ranges between 40 and 100 Hz. Higher frequencies correspond to lower adaptation and weaker synchrony. We can apply the same phase reduction methods to this model to get a system of phase equations:

$$\theta'_i = \frac{1}{N+1} \sum_{j=0}^N H(\theta_j - \theta_i, \tau) + \sigma \xi_j$$

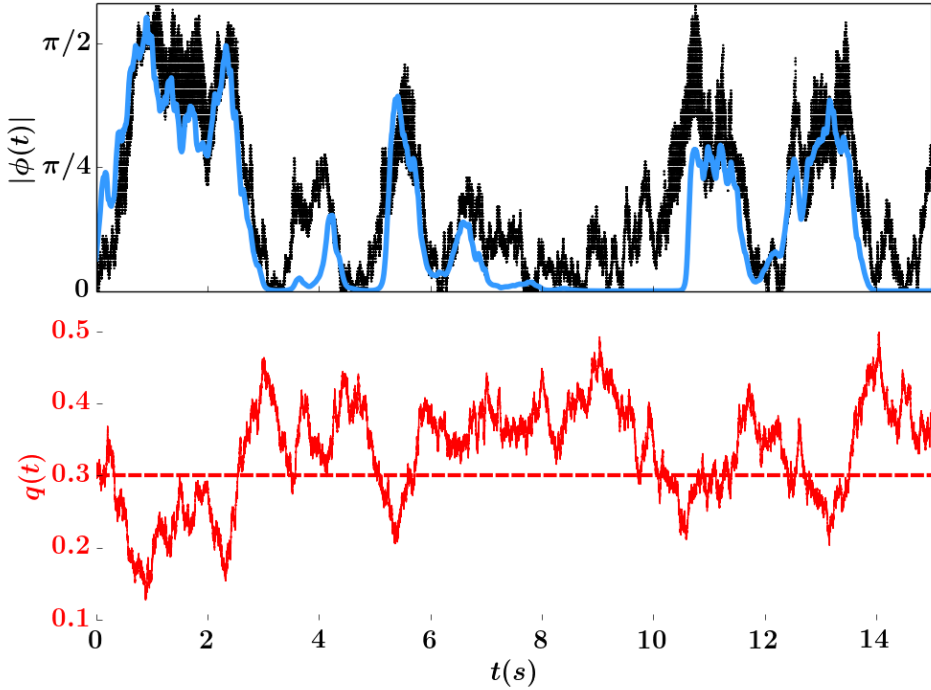


Figure 10: Noisy slowly varying parameter. Absolute value of phase difference $|\phi| = |\theta_2 - \theta_1| \in [0, 2\pi]$ theory (light blue) vs numerics (black dots). The noisy parameter is shown as a dashed red line. XPP seed 4. $\varepsilon = 0.0025$, $f = 5$. 404 cycles.

where we have added some weak noise, σ to push off the invariant synchrony manifold. To quantify the synchronization, we look at the order parameter:

$$\text{OP} = \frac{1}{N+1} \left| \sum_{j=0}^N e^{i\theta_j} \right|.$$

Figure 11c shows the clear periodic waxing and waning of OP as the slowly varying potassium conductance goes from large to small. When $q(t)$ is close to zero (no adaptation), the OP is also near zero and as $q(t)$ tends to its maximum value of 0.5, OP gets very close to 1. Thus, we see that slow modulation of this type of network shows transitions in and out of synchrony. We expect similar effects for non-periodic modulation as long as it is sufficiently slow.

4 Discussion

We have shown that it is possible to still accurately apply weak coupling theory and phase reduction to oscillators even in a changing environment

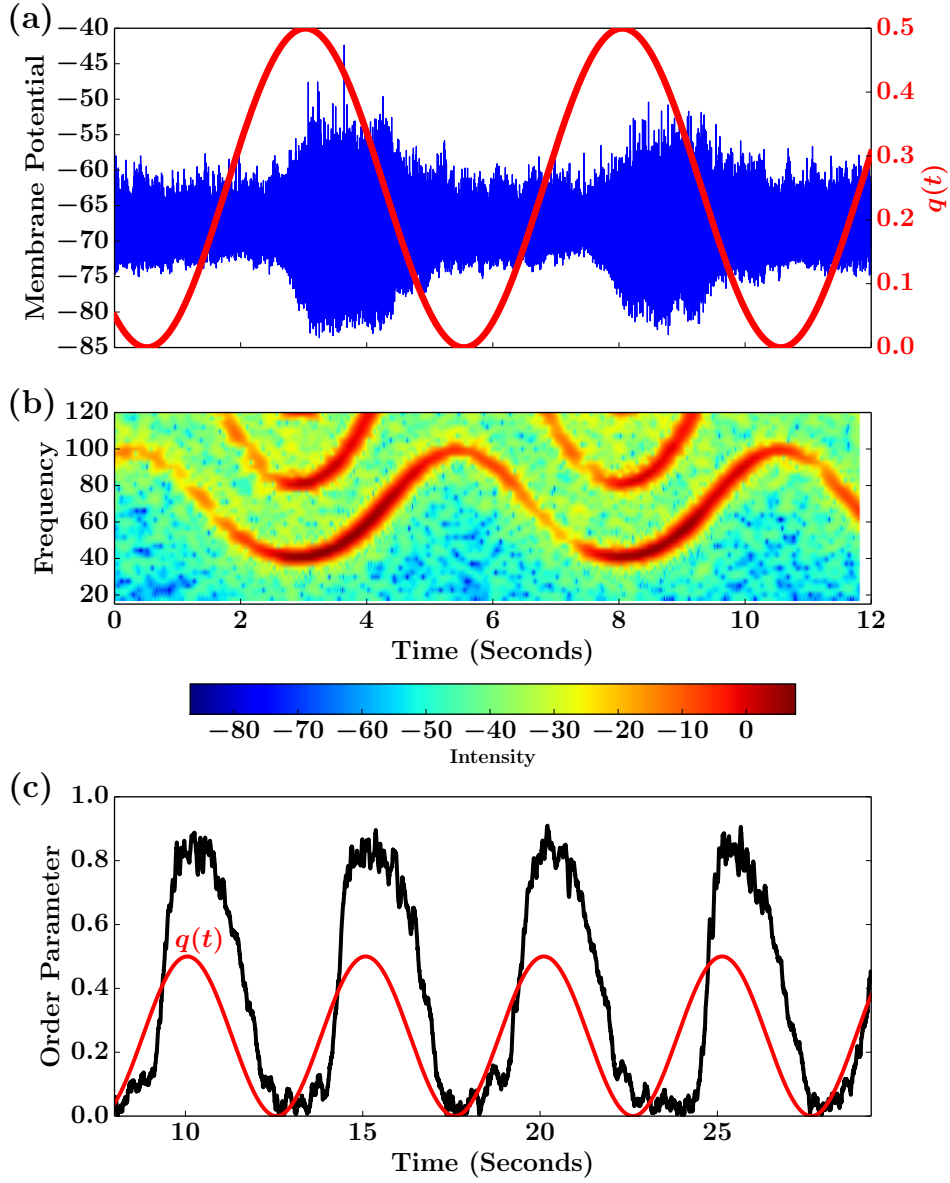


Figure 11: Network of 51 Traub oscillators all-all coupled as in previous figures. (a) Summed voltage $V_{tot} = \sum_j V_j(t)$ along with the modulation of the potassium conductance; (b) Spectrogram showing greatly increased power when the conductance is high; (c) Order parameter from the phase reduction showing a similar increase

when the changes are occurring at a sufficiently slow time scale. In a previous paper [23], we showed that slow *coupling* between oscillators was equivalent to weak coupling and that when the slow parameters were frozen, then

the spike-to-spike synchrony in some moderate interval of time could be predicted by the corresponding interaction function. Here, we formalize this notion and demonstrate that the interaction functions are time-dependent (with respect to the slowly varying parameter) and thus, we do not need to freeze any parameters. In the present theory, the slow forcing was exogenous and imposed on the system. In contrast, in bursting systems, the slow modulation is internally generated as the slow variable goes through various bifurcations between quiescence and oscillations. In [25], Sherman studied two weakly coupled bursters and observed that during the spiking phase (when the fast system is periodic), spikes did not synchronize but were driven to asymmetric and out-of-phase oscillations. The methods we have developed here require the existence of a limit cycle, so they cannot be applied globally to the spike synchronization during autonomous bursting. However, if we make the reasonable assumption that during the quiescent stage of the burst, the two cells are drawn to the slowly changing equilibrium, then, when they jump up, they will be nearly synchronous (but, not quite; if they were precisely synchronous, then they would stay that way for all time). We can then use the theory developed here to study the dynamics of the spike-to-spike synchrony during the active period of the burst and thus explain in a more formal matter Sherman's results.

Gutkin et al [12] looked at how spiking neural oscillators subjected to a slowly varying input responded to brief perturbations given between spikes. They measured the inter-spike interval (ISI) without the perturbation and then fixed the input so the oscillator had the same period as the ISI. With this fixed oscillator, they computed the phase response curve (the function $Z(t)$ solving the adjoint problem) and used this to predict how the perturbation would affect the spike time in the slowly varying system. The method developed here, could be used to improve this estimate since we know both the slowly varying frequency and the slowly varying function $Z(t; \tau)$. This type of correction was, in fact, the goal of [17].

Slowly varying inputs differ in ways both quantitative and, more importantly, qualitative from faster inputs. For example, suppose that two oscillators receive identical periodic inputs that have a frequency close to the unforced frequency of the oscillators. Then for some range of input amplitudes, we can expect the oscillators to lock in a 1:1 manner with each other and thus be completely synchronized even in absence of coupling. Similarly, weak identical noise applied to two uncoupled oscillators will also synchronize them [7, 22, 28], but the noise has to be sufficiently fast; synchrony falls off rapidly as the time constant of the noise slows down [10]. Thus, fast common rapidly changing inputs will tend to synchronize uncoupled oscillators. But the slow modulations we study here have no such properties. Indeed, looking at equations (7-8), the common *slow* input cannot move the phase-difference without direct coupling. It would be interesting to look at the synchronization between two slowly varying oscillators that are sub-

jected to fast correlated noise and derive some equations for the expected phase-difference.

5 Conclusion

The Fredholm alternative provides a useful proof method to re-derive the phase equation in Kurebayashi et al. After obtaining the phase equation, we use the theory of weakly coupled oscillators to derive the interaction function, from which we can study the stability of synchrony and anti-synchrony.

Despite the phase estimation and the mode truncation, our theory accurately predicts the phase of the Traub model with periodic, quasi-periodic, and stochastic slowly varying parameters (we have similar positive results for the $\lambda - \omega$ system). Because the mode truncation depends on the accuracy of the numerically derived interaction functions, and because the interaction functions in turn depend only on the coupling terms and the iPRC, we can apply the mode truncation method (and subsequently our result) to any autonomous system for which the iPRC and coupling terms are known. The methods here show that we can extend the notion of weak coupling and synchronization of nonlinear neural oscillators to the more realistic scenario in which the environment is changing.

Acknowledgments BE and YMP were partially supported by NSF DMS 1219753

6 Traub Model With Adaptation

All other equations for the Traub model are defined as follows

$$\begin{aligned} t_w(V) &= \tau_w / (3.3 \exp((V - V_{wt})/20) + \exp(-(V - V_{wt})/20)) \\ w_\infty(V) &= 1 / (1 + \exp(-(V - V_{wt})/10)) \\ a_m(V) &= 0.32(54 + V) / (1 - \exp(-(V + 54)/4)) \\ b_m(V) &= 0.28(V + 27) / (\exp((V + 27)/5) - 1) \\ a_h(V) &= 0.128 \exp(-(V - V_{hn})/18) \\ b_h(V) &= 4 / (1 + \exp(-(V + 27)/5)) \\ a_n(V) &= 0.032(V + 52) / (1 - \exp(-(V + 52)/5)) \\ b_n(V) &= 0.5 \exp(-(57 + V)/40) \\ \alpha(V) &= a_0 / (1 + \exp(-(V - V_t)/V_s)) \end{aligned}$$

6.1 Fourier Coefficients

The Fourier coefficients used in the approximation are shown in Table 2

Table 1: Traub parameter values

Parameter	Value
C	$1\mu\text{F}/\text{cm}^2$
g	$5\text{mS}/\text{cm}^2$
ε	0.0025
f	$0.5(\frac{1000\varepsilon}{2\pi}\text{Hz})$
I	$3\mu\text{A}/\text{cm}^2$
V_{wt}	-35mV
τ_w	100ms
E_k	-100mV
E_{Na}	50mV
E_l	-67mV
g_l	$0.2\text{mS}/\text{cm}^2$
g_k	$80\text{mS}/\text{cm}^2$
g_{Na}	$100\text{mS}/\text{cm}^2$
V_{hn}	-50mV
a_0	4
τ	4ms
V_t	0mV
V_s	5mV
E_{syn}	0mV
q_0	$0.3\text{mS}/\text{cm}^2$
q_1	$0.2\text{mS}/\text{cm}^2$

Table 2: Traub Fourier Coefficients

Cosine	Sine
$a_0(0.1) = 19.6011939665$	-
$a_0(0.3) = 17.4255017198$	-
$a_1(0.1) = -3.32476526025$	$b_1(0.1) = 0.721387113706$
$a_1(0.3) = -6.97305767558$	$b_1(0.3) = -1.5028098729$
$a_2(0.1) = -0.255371105623$	$b_2(0.1) = 0.738312597998$
$a_2(0.3) = 0.83690237427$	$b_2(0.3) = 1.03494013487$

References

- [1] Eric Brown, Jeff Moehlis, and Philip Holmes. On the phase reduction and response dynamics of neural oscillator populations. *Neural Computation*, 16(4):673–715, 2004.
- [2] John R Cressman Jr, Ghanim Ullah, Jokubas Ziburkus, Steven J Schiff, and Ernest Barreto. The influence of sodium and potassium dynamics on excitability, seizures, and the stability of persistent states: I. single neuron dynamics. *Journal of Computational Neuroscience*, 26(2):159–170, 2009.
- [3] Per Danzl, Robert Hansen, Guillaume Bonnet, and Jeff Moehlis. Partial phase synchronization of neural populations due to random Poisson inputs. *Journal of Computational Neuroscience*, 25(1):141–157, 2008.
- [4] Bard Ermentrout. *Simulating, analyzing, and animating dynamical systems: a guide to XPPAUT for researchers and students*, volume 14. SIAM, 2002.
- [5] Bard Ermentrout, Matthew Pascal, and Boris Gutkin. The effects of spike frequency adaptation and negative feedback on the synchronization of neural oscillators. *Neural Computation*, 13(6):1285–1310, 2001.
- [6] G Bard Ermentrout, Bryce Beverlin II, and Theoden Netoff. Phase response curves to measure ion channel effects on neurons. In *Phase response curves in neuroscience*, pages 207–236. Springer, 2012.
- [7] G Bard Ermentrout, Roberto F Galán, and Nathaniel N Urban. Reliability, synchrony and noise. *Trends in neurosciences*, 31(8):428–434, 2008.
- [8] G.Bard Ermentrout. n:m phase-locking of weakly coupled oscillators. *Journal of Mathematical Biology*, 12(3):327–342, 1981.

- [9] George Bard Ermentrout and Nancy Kopell. Frequency plateaus in a chain of weakly coupled oscillators, I. *SIAM Journal on Mathematical Analysis*, 15(2):215–237, 1984.
- [10] Roberto F Galán, G Bard Ermentrout, and Nathaniel N Urban. Optimal time scale for spike-time reliability: theory, simulations, and experiments. *Journal of Neurophysiology*, 99(1):277–283, 2008.
- [11] Natalia Gorelova, Jeremy K Seamans, and Charles R Yang. Mechanisms of dopamine activation of fast-spiking interneurons that exert inhibition in rat prefrontal cortex. *Journal of Neurophysiology*, 88(6):3150–3166, 2002.
- [12] Boris S Gutkin, G Bard Ermentrout, and Alex D Reyes. Phase-response curves give the responses of neurons to transient inputs. *Journal of Neurophysiology*, 94(2):1623–1635, 2005.
- [13] Ho Young Jeong and Boris Gutkin. Synchrony of neuronal oscillations controlled by GABAergic reversal potentials. *Neural Computation*, 19(3):706–729, 2007.
- [14] James P Keener. *Principles of applied mathematics*. Addison-Wesley, 1988.
- [15] N. Kopell and L.N. Howard. Plane wave solutions to reaction diffusion equations. 52:291–328, 1973.
- [16] Y. Kuramoto. *Chemical oscillations, waves, and turbulence*. Springer-Verlag, New York, 1984.
- [17] Wataru Kurebayashi, Sho Shirasaka, and Hiroya Nakao. Phase reduction method for strongly perturbed limit cycle oscillators. *Physical Review Letters*, 111:214101, Nov 2013.
- [18] Wataru Kurebayashi, Sho Shirasaka, and Hiroya Nakao. A criterion for timescale decomposition of external inputs for generalized phase reduction of limit-cycle oscillators. *Nonlinear Theory and Its Applications, IEICE*, 6(2):171–180, 2015.
- [19] GJM Marée. Slow passage through a pitchfork bifurcation. *SIAM Journal on Applied Mathematics*, 56(3):889–918, 1996.
- [20] David A McCormick. Cellular mechanisms underlying cholinergic and noradrenergic modulation of neuronal firing mode in the cat and guinea pig dorsal lateral geniculate nucleus. *The Journal of Neuroscience*, 12(1):278–289, 1992.

- [21] Benjamin Pfeuty, Germán Mato, David Golomb, and David Hansel. Electrical synapses and synchrony: the role of intrinsic currents. *The Journal of Neuroscience*, 23(15):6280–6294, 2003.
- [22] Arkady Pikovsky, Michael Rosenblum, and Jürgen Kurths. *Synchronization: a universal concept in nonlinear sciences*, volume 12. Cambridge University Press, 2003.
- [23] Jonathan J. Rubin, Jonathan E. Rubin, and G. Bard Ermentrout. Analysis of synchronization in a slowly changing environment: How slow coupling becomes fast weak coupling. *Physical Review Letters*, 110:204101, May 2013.
- [24] Michael A Schwemmer and Timothy J Lewis. The theory of weakly coupled oscillators. In *Phase Response Curves in Neuroscience*, pages 3–31. Springer, 2012.
- [25] Arthur Sherman. Anti-phase, asymmetric and aperiodic oscillations in excitable cells—I. coupled bursters. *Bulletin of Mathematical Biology*, 56(5):811–835, 1994.
- [26] Klaus M Stiefel, Boris S Gutkin, and Terrence J Sejnowski. Cholinergic neuromodulation changes phase response curve shape and type in cortical pyramidal neurons. *PloS One*, 3(12):e3947–e3947, 2008.
- [27] Klaus M Stiefel, Boris S Gutkin, and Terrence J Sejnowski. The effects of cholinergic neuromodulation on neuronal phase-response curves of modeled cortical neurons. *Journal of Computational Neuroscience*, 26(2):289–301, 2009.
- [28] Jun-nosuke Teramae and Dan Tanaka. Robustness of the noise-induced phase synchronization in a general class of limit cycle oscillators. *Physical Review Letters*, 93(20):204103, 2004.
- [29] Xiao-Jing Wang and György Buzsáki. Gamma oscillation by synaptic inhibition in a hippocampal interneuronal network model. *The Journal of Neuroscience*, 16(20):6402–6413, 1996.

Scalar Reduction of a Neural Field Model with Spike Frequency Adaptation

Youngmin Park* & Bard Ermentrout
Department of Mathematics
University of Pittsburgh
Pittsburgh PA 15260

January 18, 2018

Abstract

We study a deterministic version of a one- and two-dimensional attractor neural network model of hippocampal activity first studied by Itskov et al 2011. We analyze the dynamics of the system on the ring and torus domain with an even periodized weight matrix, assuming weak and slow spike frequency adaptation and a weak stationary input current. On these domains, we find transitions from spatially localized stationary solutions (“bumps”) to (periodically modulated) solutions (“sloshers”), as well as constant and non-constant velocity traveling bumps depending on the relative strength of external input current and adaptation. The weak and slow adaptation allows for a reduction of the system from a distributed partial integro-differential equation to a system of scalar Volterra integro-differential equations describing the movement of the centroid of the bump solution. Using this reduction, we show that on both domains, sloshing solutions arise through an Andronov-Hopf bifurcation and derive a normal form for the Hopf bifurcation on the ring. We also show existence and stability of constant velocity solutions on both domains using Evans functions. In contrast to existing studies, we assume a general weight matrix of Mexican-hat type in addition to a smooth firing rate function.

1 Introduction

Spatially coherent activity states exist during normal brain function including mammalian path integration, head direction tracking, visual hallucination, working memory, spatial object location, and object orientation [4, 5, 12]. Neural field models (also called continuous attractor neural networks) are one way to understand the mechanism underlying such spatially

*Corresponding author. Email yop6@pitt.edu

coherent phenomena [17, 15, 16]. In neural recordings and field models, these spatio-temporal dynamics manifest as traveling waves, spirals, or single or multiple localized “bumps” or “pulses” of activity [4].

Extensive literature exists on the analysis of these behaviors. In particular, [32] show the existence and stability of traveling bumps using multiple-layer neural fields. Several other studies use one of or a combination of short term depression and spike frequency adaptation. In [24], the authors show that traveling pulses exist in a model with synaptic depression and adaptation when synaptic depression is sufficiently weak. For stronger synaptic depression, the traveling pulse ceases to exist via a saddle-node bifurcation. In [15] the authors show that spontaneous motion of a bump solution exists for a neural field with only spike frequency adaptation, and in a similar neural field model with only short term synaptic depression. The authors in [28] show the existence of a traveling pulse solution in a neural field model with spike frequency adaptation. The previous two studies also show the existence of traveling wavefronts in their respective neural field models.

In addition to the analysis of traveling bumps or wavefronts, rich oscillatory solutions of neural fields are also possible. For example, with spatially localized input current and spike frequency adaptation, a bump solution may oscillate in diameter (breathers)[3, 11, 12, 13], which may play a role in generating epileptiform activity [13] and the processing of sensory stimuli [12]. There also exist studies of a combination of traveling and breathing pulses in an inhibitory-excitatory neural field [10]. In addition to breathers, there exist pulse-emitting neural fields [24, 23], oscillatory wavefronts [2, 3], and spiral waves [23].

Despite this large body of literature, the analyses often require particular assumptions. For example, the existence of “sloshing” solutions – bump solutions that oscillate periodically in the centroid – that arise through a Hopf bifurcation is known under certain assumptions. In early work, sloshers are shown to exist numerically using a rate model with a threshold nonlinearity [18]. In recent work, the authors of [6] show the existence of a Hopf bifurcation with a cosine kernel and a particular choice of smooth firing rate function. In [9], Folias computes a normal form for the Hopf bifurcation using a general kernel, but for a Heaviside firing rate function.

Proving existence of other phenomena also require special assumptions. In [8], the authors consider a neural field model on the real line with synaptic depression and prove the existence of a traveling pulse without a Heaviside assumption, but use the particular choice of a normalized exponential kernel. In [22], the authors use a center manifold reduction to analyze the existence of moving bump solutions. They allow the firing rate to be sigmoidal or a Heaviside, but require a cosine kernel. Similar assumptions are made in [], where they assume a hyperbolic tangent firing rate function and a cosine kernel.

The most general of such studies, [28], considers a neural field model

on the real line with spike frequency adaptation and a singular perturbation approach to construct a constant velocity traveling pulse on the real line with a general firing rate function and a general kernel. However, the existence of other phenomena are not shown.

In this paper, we introduce a method to analyze the dynamics of a neural field model on a one- and two-dimensional domain with periodic boundary conditions and assume a smooth firing rate and an even, periodic kernel. Using our method, with standard numerical and analytical dynamical systems tools, we show existence and stability of traveling pulse solutions and oscillatory dynamics. In particular, we analyze sloshing solutions on the ring and torus.

The neural field we consider in this paper is defined as

$$\begin{aligned} \frac{\partial u(\mathbf{x}, t)}{\partial t} &= -u(\mathbf{x}, t) + \int_{\Omega} K(\mathbf{x} - \mathbf{y}) f(u(\mathbf{y}, t)) d\mathbf{y} \\ &\quad + \varepsilon \left[qI(\mathbf{x}) + \int_{\Omega} w(\mathbf{x}, \mathbf{y}) f(u(\mathbf{y}, t)) d\mathbf{y} - gz(\mathbf{x}, t) \right], \end{aligned} \quad (1)$$

$$\frac{\partial z(\mathbf{x}, t)}{\partial t} = \varepsilon\beta[-z(\mathbf{x}, t) + u(\mathbf{x}, t)], \quad (2)$$

where the parameter ε is small, $0 < \varepsilon \ll 1$, and $\mathbf{x}, \mathbf{y} \in \mathbb{R}^n$. For $n = 2$, the kernel function K is an even function in the sense that, $K(-x, y) = K(x, -y) = K(x, y)$, and doubly periodic in the sense that $K(x + 2n\pi, y + 2m\pi) = K(x, y)$, for any integers n, m . The function w represents heterogeneity of neural connections, and q, g, β are constants. For convenience, we will denote the domain $\Omega = [-\pi, \pi]^m$, with $m = 1, 2$. Thus in one-dimension the domain is a ring and in two-dimensions a torus. The variable $z(\mathbf{x}, t)$ represents linear adaptation [28] and $I(\mathbf{x})$ an external input to the network. External inputs represent persistent stimuli that can be used to entrain the bump and move it to a specific location ([1]. We have chosen to make both the timescale of adaptation and *its magnitude* to be small. While there is good biological justification for the former assumption as there are many forms of slow adaptation ([20] section 7.4), the assumption that the adaptation is small is less biological. For the existence of traveling waves, adaptation need not be small ([28]), but in order to study how the adaptation interacts with stimuli, we need both the adaptation and the stimuli to be the same order of magnitude. The effects of large stimuli to general neural field models are not easy to analyze, so that by treating them as perturbations, we are able to consider the effects in a great deal of detail. Thus, one can regard this assumption as a starting point for the continuation of these phenomena to large amplitude stimuli and adaptation.

Our goal in this paper is to analyze Equations (1),(2) when ε is small. When $\varepsilon = 0$, there is a stable ‘‘bump’’ attractor, $u_0(\mathbf{x})$, in the scalar neural field (1), i.e., a local stationary peak of $u(\mathbf{x}, t)$ centered at $\mathbf{x} = 0$. The bump

attractor satisfies

$$u_0(\mathbf{x}) = \int_{\Omega} K(\mathbf{x} - \mathbf{y}) f(u_0(\mathbf{y})) d\mathbf{y},$$

where u_0 is nonconstant and even.

Although we allow for a general even, doubly periodic kernel in one- and two-dimensions and a general smooth threshold nonlinearity f , we make particular choices for numerical simulations. We choose f as

$$f(x) = \frac{1}{\exp(-r(x - u_{th}))},$$

where $r = 15$, $u_{th} = 0.25$. In the one-dimensional case, we choose the kernel to be $K(x) = A + B \cos(x)$ with $A = -0.5$, $B = 3$ unless stated otherwise. In the two-dimensional case, we form the Mexican-hat function,

$$\hat{K}(r) = Ae^{-(r/\sigma_e)^2} - Be^{-(r/\sigma_i)^2},$$

where $r \equiv r(x, y, n, m) = \sqrt{(x + 2\pi n)^2 + (y + 2\pi m)^2}$. We make the function \hat{K} periodic in two dimensions using the definition

$$K(x, y) = \sum_{m=-\infty}^{\infty} \sum_{n=-\infty}^{\infty} \hat{K}(r(x, y, n, m)).$$

The parameters here are

$$A = \frac{1}{\sqrt{\pi}\sigma_e}, \quad B = \frac{1}{\sqrt{\pi}\sigma_i},$$

where $\sigma_e = 2$, and $\sigma_i = 3$. For numerical simulations, we find it sufficient to replace the infinite sum with a finite sum from $n, m = -5$ to $n, m = 5$. This is because the function $\hat{K}(r)$ is a decaying exponential and therefore negligible for large r . For example, if a bump solution remains close to the origin, contributions from terms a distance of 10π (i.e., n or $m=5$) are negligible because $\exp(-(10\pi)^2) \approx 2 \times 10^{-429}$.

To analyze particular dynamics in more detail, we numerically compute the period kernel above, then take the Fourier truncation of this doubly periodic kernel,

$$K(x, y) = k_0 + k_1(\cos x + \cos y) + k_2 \cos x \cos y.$$

We now outline the organization of the paper, as follows: We reduce Equations (1),(2) to a set of integro-differential equations for the centroid of the bump solution on the ring and torus. We study bifurcations of these equations using numerical and analytical techniques to show existence and stability of constant velocity traveling bumps and sloshing bumps. Depending on the parameter values g, q , these traveling bumps may traverse the

domain periodically or exhibit chaos. Next we turn to the torus domain and perform similar analyses: we study bifurcations of these equations using numerical and analytical techniques to show existence and stability of constant velocity traveling bumps. In addition to the sloshing solutions found in the one-dimensional model, we also find several types of traveling bumps and modulated traveling bumps that densely fill the torus. We also find chaotic motion in some cases. We conclude with a discussion and some contrasts to previous analyses. We remark that all figure generation code and relevant data files with documentation is available on GitHub at https://github.com/youngmp/park_and_ermanntrout_2017

2 Derivation of the Phase Equation

We start with Equations (1),(2). Let $\tau = \varepsilon t$ be a slow timescale and assume that both z and u depend only on (\mathbf{x}, τ) . In this case, we can integrate equation (2) to obtain:

$$z(\mathbf{x}, \tau) = z(\mathbf{x}, 0)e^{-\beta\tau} + \beta \int_0^\tau e^{-\beta(\tau-s)} u(\mathbf{x}, s) ds.$$

Since we are mainly interested in long term behavior, we can ignore the first exponentially decaying term. With these assumptions, we obtain the following scalar integro-differential equation:

$$\begin{aligned} \varepsilon \frac{\partial u(\mathbf{x}, \tau)}{\partial \tau} &= -u(\mathbf{x}, \tau) + \int_{\Omega} K(\mathbf{x} - \mathbf{y}) f(u(\mathbf{y}, \tau)) d\mathbf{y} \\ &+ \varepsilon \left[qI(\mathbf{x}) + \int_{\Omega} w(\mathbf{x}, \mathbf{y}) f(u(\mathbf{y}, \tau)) d\mathbf{y} - g\beta \int_0^\tau e^{-\beta(\tau-s)} u(\mathbf{x}, s) ds \right]. \end{aligned} \quad (3)$$

We will assume $u(\mathbf{x}, \tau) = U(\mathbf{x}, \tau, \varepsilon)$ and expand U as a power series in ε to get an approximate solution. Thus,

$$U(x, \tau, \varepsilon) = U_0(\mathbf{x}, \tau) + \varepsilon U_1(\mathbf{x}, \tau) + O(\varepsilon^2).$$

Substituting this power series into (3), we get (with a bit of re-arrangement):

$$0 = -U_0(\mathbf{x}, \tau) + \int_{\Omega} K(\mathbf{x} - \mathbf{y}) f(U_0(\mathbf{y}, \tau)) d\mathbf{y} \quad (4)$$

$$(LU_1)(\mathbf{x}, \tau) = \frac{\partial U_0(\mathbf{x}, \tau)}{\partial \tau} - R_1(\mathbf{x}, \tau), \quad (5)$$

where

$$(Lv)(\mathbf{x}, \tau) = -v(\mathbf{x}, \tau) + \int_{\Omega} K(\mathbf{x} - \mathbf{y}) f'(U_0(\mathbf{y}, \tau)) v(\mathbf{y}, \tau) d\mathbf{y},$$

and

$$R_1(\mathbf{x}, \tau) = qI(\mathbf{x}) + \int_{\Omega} w(\mathbf{x}, \mathbf{y}) f(U_0(\mathbf{y}, \tau)) d\mathbf{y} - g\beta \int_0^{\tau} e^{-\beta(\tau-s)} U_0(\mathbf{x}, s) ds.$$

The equation for $U_0(\mathbf{x}, \tau)$ is the equation for the bump solution and since it is translation invariant, we see that

$$U_0(\mathbf{x}, \tau) = u_0(\mathbf{x} + \boldsymbol{\theta}(\tau))$$

where $\boldsymbol{\theta}(\tau)$ is a τ -dependent phase shift of the bump. Our goal, then is to determine the dynamics of $\boldsymbol{\theta}(\tau)$. Figure 1 shows typical examples of the stationary bump $U_0(x)$ for one- and two-dimensions.

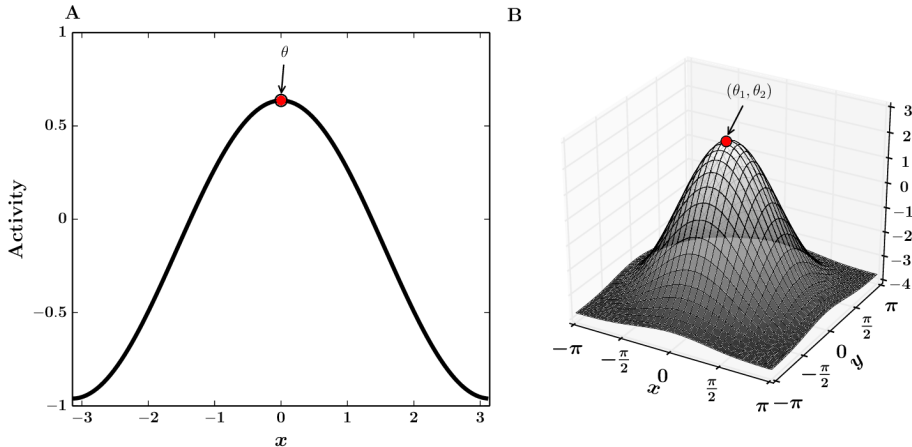


Figure 1: Numerically computed stationary bump solutions on the ring A:, and torus B:. The red circle denotes the centroid of each bump solution. On the ring, we denote the centroid by θ , while we denote the centroid of the bump on the torus by (θ_1, θ_2) . Our phase model (Equation (9)) describes shifts in the centroid.

Before continuing with the perturbation calculation, we establish a few preliminaries. We define the compact linear operator

$$(L_0 v)(\mathbf{x}) = -v(\mathbf{x}) + \int_{\Omega} K(\mathbf{x} - \mathbf{y}) f'(u_0(\mathbf{y})) v(\mathbf{y}) d\mathbf{y}$$

and establish several properties of it. Recall that the bump, $u_0(\mathbf{x})$ satisfies

$$-u_0(\mathbf{x}) + \int_{\Omega} K(\mathbf{x} - \mathbf{y}) f(u_0(\mathbf{y})) d\mathbf{y} = 0.$$

By making a change of variables and noting that all functions are periodic in \mathbf{x} (that is, periodic in each of the components of \mathbf{x}), then $u_0(\mathbf{x})$ satisfies

$$-u_0(\mathbf{x}) + \int_{\Omega} K(\mathbf{y}) f(u_0(\mathbf{x} - \mathbf{y})) d\mathbf{y} = 0. \quad (6)$$

Recalling that the domain is $\Omega = [-\pi, \pi]^m$, with $m = 1, 2$, we center u_0 at the origin. Thus, $u_0(\mathbf{x})$ is an even periodic function of \mathbf{x} , component-wise. Let $\partial_i u(\mathbf{x})$ denote the partial derivative of $u(\mathbf{x})$ along the x_i direction where $\mathbf{x} = (x_1, x_2)$. If we differentiate (6) along one of the axes, we see that

$$-\partial_i u_0(\mathbf{x}) + \int_{\Omega} K(\mathbf{y}) f'(u_0(\mathbf{x} - \mathbf{y})) \partial_i u_0(\mathbf{x} - \mathbf{y}) d\mathbf{y} = 0.$$

and changing variables again, we rewrite this as

$$-\partial_i u_0(\mathbf{x}) + \int_{\Omega} K(\mathbf{x} - \mathbf{y}) f'(u_0(\mathbf{y})) \partial_i u_0(\mathbf{y}) d\mathbf{y} = 0, \quad (7)$$

so we see that $L_0 \partial_i u_0(\mathbf{x}) = 0$. In other words, the linear operator, L_0 has an m -dimensional nullspace spanned by the principle directional derivatives of $u_0(\mathbf{x})$. With the natural inner product

$$\langle u(\mathbf{x}), v(\mathbf{x}) \rangle = \int_{\Omega} u(\mathbf{x}) v(\mathbf{x}) d\mathbf{x}$$

the operator L_0 has an adjoint

$$(L^* v)(\mathbf{x}) = -v(\mathbf{x}) + f'(u_0(\mathbf{x})) \int_{\Omega} K(\mathbf{x} - \mathbf{y}) v(\mathbf{y}) d\mathbf{y}.$$

By multiplying equation (7) by $f'(u_0(\mathbf{x}))$, we see that the nullspace of L^* is spanned by $v_i^*(\mathbf{x}) = f'(u_0(\mathbf{x})) \partial_i u_0(\mathbf{x})$. Since $u_0(\mathbf{x})$ is an even periodic function, componentwise, we note that $\partial_1 u_0(\mathbf{x})$ is even in x_2 and odd in x_1 where $\mathbf{x} = (x_1, x_2)$; $v_1^*(\mathbf{x})$ has the same property, while $\partial_2 u_0(\mathbf{x}), v_2^*(\mathbf{x})$ are even in x_1 and odd in x_2 . These properties imply the $\langle \partial_i u_0(\mathbf{x}), v_k^*(\mathbf{x}) \rangle = 0$ when $i \neq k$. We also have

$$\langle \partial_i u_0(\mathbf{x}), v_i^*(\mathbf{x}) \rangle = \int_{\Omega} f'(u_0(\mathbf{x})) [\partial_i u_0(\mathbf{x})]^2 d\mathbf{x} = \mu > 0.$$

Finally, the Fredholm alternative holds for L_0 . That is, for any continuous periodic function $b(\mathbf{x})$,

$$(L_0 v)(\mathbf{x}) = b(\mathbf{x})$$

has a bounded solution if and only if

$$\langle v_i^*(\mathbf{x}), b(\mathbf{x}) \rangle = 0$$

for $i = 1, \dots, m$ [21].

With these technical issues aside, we turn to equation (5), which we can rewrite as

$$(L_0 U_1)(\mathbf{x}, \tau) = (\partial_1 u_0(\mathbf{x} + \boldsymbol{\theta}(\tau)), \partial_2 u_0(\mathbf{x} + \boldsymbol{\theta}(\tau))) \cdot \frac{d\boldsymbol{\theta}(\tau)}{d\tau} - R_1(\mathbf{x}, \tau)$$

Writing $\boldsymbol{\theta}(\tau) = (\theta_1(\tau), \theta_2(\tau))$ and applying the m conditions for the Fredholm alternative, we arrive at

$$\mu \frac{d\theta_i}{d\tau} = q J_i(\boldsymbol{\theta}) + W_i(\boldsymbol{\theta}) - g\beta \int_0^\tau e^{-\beta(\tau-s)} H_i(\boldsymbol{\theta}(s) - \boldsymbol{\theta}(\tau)) ds \quad (8)$$

where

$$\begin{aligned} \mu &= \int_{\Omega} f'(u_0(\mathbf{x})) [\partial_i u_0(\mathbf{x})]^2 d\mathbf{x}, \\ J_i(\boldsymbol{\theta}) &= \int_{\Omega} f'(u_0(\mathbf{x} + \boldsymbol{\theta})) \partial_i u_0(\mathbf{x} + \boldsymbol{\theta}) I(\mathbf{x}) d\mathbf{x}, \\ W_i(\boldsymbol{\theta}) &= \int_{\Omega} f'(u_0(\mathbf{x} + \boldsymbol{\theta})) \partial_i u_0(\mathbf{x} + \boldsymbol{\theta}) \int_{\Omega} w(\mathbf{x}, \mathbf{y}) f(u_0(\mathbf{y})) d\mathbf{y} d\mathbf{x}, \\ H_i(\boldsymbol{\theta}) &= \int_{\Omega} f'(u_0(\mathbf{x})) \partial_i u_0(\mathbf{x}) u_0(\mathbf{x} + \boldsymbol{\theta}) d\mathbf{x}. \end{aligned}$$

We note that because of the symmetry of $u_0(\mathbf{x})$, the functions, $H_i(\boldsymbol{\theta})$ have a similar symmetry which we will exploit in the analysis of Equation (8). The derivation here has been fairly general and holds in any dimension although we will focus only on one- and two-dimensional bumps in this model. Since both W_i and J_i have no explicit time dependence and act mainly as heterogeneities, we will ignore W_i and focus on J_i which is conveniently parameterized by q . Figure 2 shows the functions $H(\theta)$, $J(\theta)$ in the one-dimensional case, while Figure 3 shows the functions $H_i(\theta)$, $J_i(\theta)$ in the two-dimensional case.

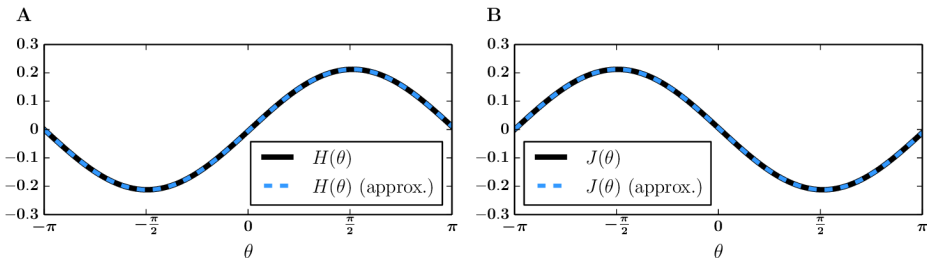


Figure 2: Numerically computed functions for the one-dimensional phase model. A: H (black solid), plotted against sine-function approximation (light blue, dashed). B: J (black solid), plotted against its sine-function approximation (light blue, dashed). Parameters: $I(x) = u_0(x)$ and $K(x) = A + B \cos(x)$, $A = -0.5$, $B = 3$.

We have reduced the problem of the bump dynamics to slow timescale phase shifts of the bump solution, represented as an integro-differential equation. For simplicity and convenience, we ignore transients by changing the

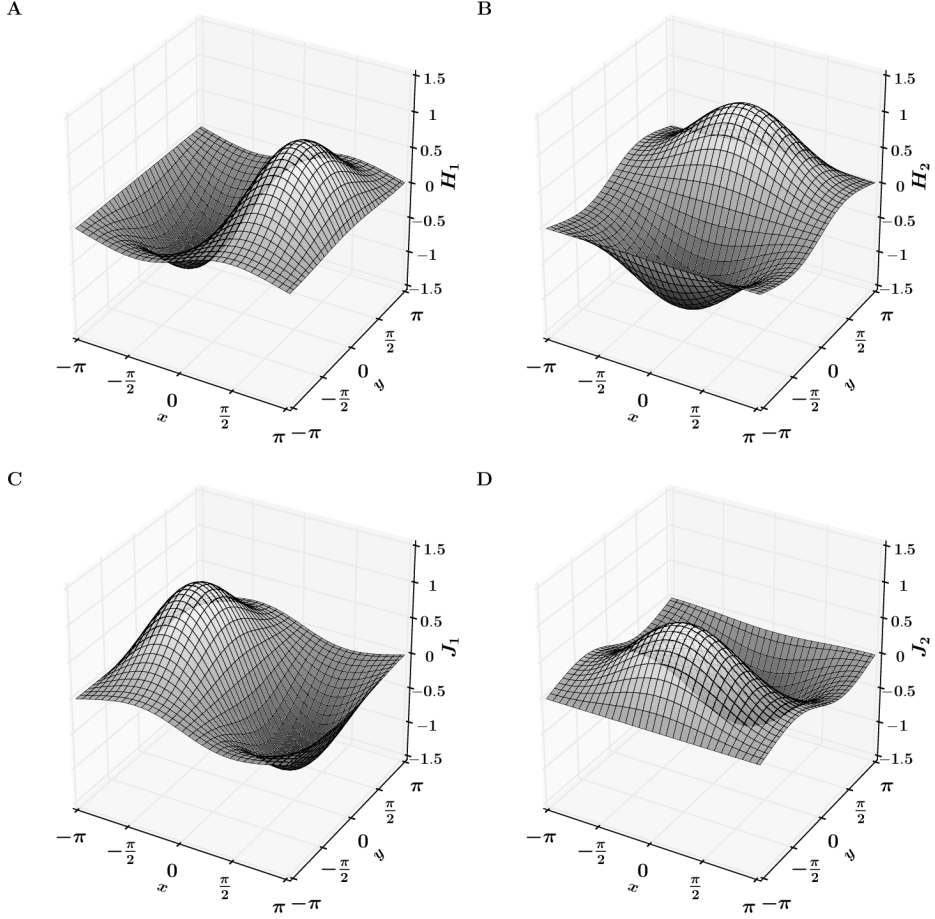


Figure 3: Numerically computed functions for the two-dimensional phase model A: H_1 , B: H_2 , C: J_1 , D: J_2 . Note that $H_2(x, y) = H_1(y, x)$. We always choose $I(x) = u_0(x)$. That is, we always use the steady-state bump as the pinning function. With this choice, $J_i = -H_i$ in 1- and 2-dimensions.

limits of integration in Equation (8) from $[0, \tau]$ to $(-\infty, \tau]$, and apply the change of variables $\xi = \tau - s$, yielding

$$\mu \frac{d\theta_i}{d\tau} = qJ_i(\boldsymbol{\theta}) - g\beta \int_0^\infty e^{-\beta\xi} H_i(\boldsymbol{\theta}(\tau - \xi) - \boldsymbol{\theta}(\tau)) d\xi.$$

With a trivial change of notation, we arrive at the equations

$$\mu \frac{d\theta_i}{d\tau} = qJ_i(\boldsymbol{\theta}) - g\beta \int_0^\infty e^{-\beta s} H_i(\boldsymbol{\theta}(\tau - s) - \boldsymbol{\theta}(\tau)) ds, \quad i = 1, \dots, m. \quad (9)$$

We study stability properties and bifurcations in this form. Note that H_i is implicitly a function of the kernel K .

To facilitate calculations, we first prove the following statements:

1. Each function H_i is odd, i.e., $H_i(-\theta_1, -\theta_2) = -H_i(\theta_1, \theta_2)$. In particular, H_1 is odd in the first coordinate and even in the second coordinate.
2. $H_1(\theta_1, \theta_2) = H_2(\theta_2, \theta_1)$.
3. If the input current $I(\mathbf{x})$ is defined as the steady-state bump solution, then $H_i(\boldsymbol{\theta}) = -J_i(\boldsymbol{\theta})$.

For the first statement, fix θ_1, θ_2 and consider the sum $H_1(-\theta_1, \theta_2) + H(\theta_1, \theta_2)$. By definition this sum is the sum of integrals

$$\int_{\Omega} f'(u_0(\mathbf{x})) \partial_1 u_0(\mathbf{x}) [u_0(x_1 + \theta_1, x_2 + \theta_2) + u_0(x_1 - \theta_1, x_2 + \theta_2)] d\mathbf{x}.$$

Given x_2 , and for the sake of clarity, consider the temporary function $\Phi(x_1) := [u_0(x_1 + \theta_1, x_2 + \theta_2) + u_0(x_1 - \theta_1, x_2 + \theta_2)]$. $\Phi(x_1)$ is an even function in x_1 because

$$\begin{aligned} \Phi(-x_1) &\equiv u_0(-x_1 + \theta_1, x_2 + \theta_2) + u_0(-x_1 - \theta_1, x_2 + \theta_2) \\ &= u_0(x_1 - \theta_1, x_2 + \theta_2) + u_0(x_1 + \theta_1, x_2 + \theta_2) \\ &\equiv \Phi(x_1). \end{aligned}$$

These lines follow by the even assumption on each coordinate of the bump solution u_0 . The remaining terms in the integrand, $\partial_1 u_0(\mathbf{x})$, and $f'(u_0(\mathbf{x}))$, are odd and even in x_1 , respectively. Thus, the integrand is odd in x_1 and the integral evaluates to zero for each x_2 (and indeed, for each θ_1, θ_2). It follows that $H_1(-\theta_1, \theta_2) + H(\theta_1, \theta_2) = 0$, i.e., that the first coordinate is odd.

To show that the second coordinate is even, we use a similar argument. Again, fix θ_1, θ_2 and consider the sum $H_1(\theta_1, -\theta_2) - H(\theta_1, \theta_2)$. By definition, this sum is the sum of integrals

$$\int_{\Omega} f'(u_0(\mathbf{x})) \partial_1 u_0(\mathbf{x}) [u_0(x_1 + \theta_1, x_2 - \theta_2) - u_0(x_1 + \theta_1, x_2 + \theta_2)] d\mathbf{x}.$$

Given x_1 , we redefine our temporary function Φ as $\Phi(x_2) := [u_0(x_1 + \theta_1, x_2 - \theta_2) - u_0(x_1 + \theta_1, x_2 + \theta_2)]$ and show that it is an odd function in x_2 .

$$\begin{aligned} \Phi(-x_2) &\equiv u_0(x_1 + \theta_1, -x_2 - \theta_2) - u_0(x_1 + \theta_1, -x_2 + \theta_2) \\ &= u_0(x_1 + \theta_1, x_2 + \theta_2) - u_0(x_1 + \theta_1, x_2 - \theta_2) \\ &= -[u_0(x_1 + \theta_1, x_2 - \theta_2) - u_0(x_1 + \theta_1, x_2 + \theta_2)] \\ &\equiv -\Phi(x_2). \end{aligned}$$

Again, these lines follow by the even assumption on each coordinate of the bump solution u_0 . The integrand term $\partial_1 u_0(\mathbf{x})$ is even in the second coordinate as is the term $f'(u_0(\mathbf{x}))$. Thus, the integrand is odd in x_2 and the

integral evaluates to zero for each x_1 (and indeed, for each θ_1, θ_2). It follows that $H_1(\theta_1, -\theta_2) - H(\theta_1, \theta_2) = 0$, i.e., that the second coordinate is even.

We have shown that H_1 is an odd function that is odd in the first coordinate and even in the second coordinate. The proof of H_2 being an odd function that is even in the first coordinate and odd in the second follows using the same arguments, or by using the second statement, which we prove next.

To prove the second statement, we proceed by definition.

$$H_1(\theta_1, \theta_2) = \int_{\Omega} f'(u_0(x_1, x_2)) \partial_1 u_0(x_1, x_2) u_0(x_1 + \theta_1, x_2 + \theta_2) dx_1 dx_2.$$

The steady-state bump solution is invariant under reflections about the unit line, and due to the radial symmetry of the bump solution, its partial derivatives are related by $\partial_1 u_0(x_1, x_2) = \partial_2 u_0(x_2, x_1)$. Thus,

$$= \int_{\Omega} f'(u_0(x_2, x_1)) \partial_2 u_0(x_2, x_1) u_0(x_1 + \theta_1, x_2 + \theta_2) dx_1 dx_2.$$

Next we relabel the coordinates and flip the order of integration

$$= \int_{\Omega} f'(u_0(x_1, x_2)) \partial_2 u_0(x_1, x_2) u_0(x_2 + \theta_1, x_1 + \theta_2) dx_1 dx_2.$$

Then we flip the coordinates of u_0 , and the resulting integral is by definition $H_2(\theta_2, \theta_1)$:

$$\begin{aligned} &= \int_{\Omega} f'(u_0(x_1, x_2)) \partial_2 u_0(x_1, x_2) u_0(x_1 + \theta_2, x_2 + \theta_1) dx_1 dx_2 \\ &= H_2(\theta_2, \theta_1). \end{aligned}$$

To prove the third statement, suppose that a function \hat{h} on a periodic two-dimensional domain $[0, 2\pi] \times [0, 2\pi]$ is odd in the first coordinate and even in the second so that $\hat{h}(x_1, x_2) = \hat{h}(x_1, -x_2) = -\hat{h}(-x_1, x_2)$. In particular, it follows that for a given value x_2 ,

$$\int_0^{2\pi} \hat{h}(x_1, x_2) dx_1 = 0,$$

and therefore

$$\int_{\Omega} \hat{h}(\mathbf{x}) d\mathbf{x} = 0.$$

This integral property holds when \hat{h} is even in the first coordinate and odd in the second with a similar argument.

If we choose $I(\mathbf{x})$ to be the steady-state bump, then

$$\begin{aligned} J_i(\boldsymbol{\theta}) &= \int_{\Omega} f'(u_0(\mathbf{x} + \boldsymbol{\theta})) \partial_i u_0(\mathbf{x} + \boldsymbol{\theta}) u_0(\mathbf{x}) \, d\mathbf{x} \\ &= \int_{\Omega} f'(u_0(\mathbf{x})) \partial_i u_0(\mathbf{x}) u_0(\mathbf{x} - \boldsymbol{\theta}) \, d\mathbf{x}. \end{aligned}$$

Then taking the sum $H_i(\boldsymbol{\theta}) + J_i(\boldsymbol{\theta})$ yields

$$H_i(\boldsymbol{\theta}) + J_i(\boldsymbol{\theta}) = \int_{\Omega} f'(u_0(\mathbf{x})) \partial_i u_0(\mathbf{x}) [u_0(\mathbf{x} + \boldsymbol{\theta}) + u_0(\mathbf{x} - \boldsymbol{\theta})] \, d\mathbf{x}.$$

For a given $\boldsymbol{\theta}$, the term $[u_0(\mathbf{x} + \boldsymbol{\theta}) + u_0(\mathbf{x} - \boldsymbol{\theta})]$ in the integrand is even in both coordinates. The remaining term, $f'(u_0(\mathbf{x})) \partial_i u_0(\mathbf{x})$, when $i = 1$ ($i = 2$), is odd (even) in the first coordinate and even (odd) in the second. Therefore, when $i = 1$ ($i = 2$), the integrand is an odd function in the first (second) coordinate and the integral evaluates to zero. It follows trivially that

$$H_i(\boldsymbol{\theta}) = -J_i(\boldsymbol{\theta}). \quad (10)$$

This property remains true on the ring using the same argument.

These statements will come in useful in the sections to follow. We now proceed with an analysis of the reduced equations on the ring domain.

Remark We have assumed *linear* adaptation in our derivation of the reduced model, but, this is not necessary. We could replace Equation (2) by

$$\frac{\partial z(\mathbf{x}, t)}{\partial t} = \varepsilon \beta [-z(\mathbf{x}, t) + M(u(\mathbf{x}, t))]$$

where $M(u)$ is an arbitrary monotonically increasing continuously differentiable function. In this case, we find

$$H_i(\boldsymbol{\theta}) = \int_{\Omega} f'(u_0(\mathbf{x})) \partial_i u_0(\mathbf{x}) M(u_0(\mathbf{x} + \boldsymbol{\theta})) \, d\mathbf{x}.$$

The new version of H_i has exactly the same properties as the linear case since $M(u_0(x))$ is an even function and its derivative with respect to x is an odd function.

3 The Ring Domain

In this section, we choose the domain Ω to be the ring. First, we thoroughly analyze the full neural field model through a bifurcation analysis. We then turn to Equation (9) on the ring and perform the same bifurcation analysis and through analytical study.

3.1 Equivalent Neural Field Model on the Ring

To classify the bifurcations of the full neural field model on the ring, we transform the equations to an equivalent 6-dimensional system of ODEs, allowing us to use dynamical systems software and techniques to analyze the model. Recall that for numerical simulations on the ring, we choose a cosine kernel $K(x) = A + B \cos(x)$. This technique and choice of kernel is the same as that used in [25], where as part of the study they analyze a rate model similar to the model in the current study, but in contrast, the adaptation and input current terms are input directly to the firing rate function. They provide sufficient detail with regards to transforming their rate model to a system of ODEs, but as the details differ from our model, we include the derivation of our model here (in particular they include a phase lag between the peak of the bump activity u and the peak of the adaptation activity z which results in slightly different equations).

Note that with this choice of kernel, the bump solution is also sinusoidal and without loss of generality takes the form $u_0(x) = C + D \cos(x)$. For simplicity we choose $J(x) = u_0(x)$. We are now ready to transform the equations.

Since the functions $u(x, t), z(x, t)$ are periodic in x , we expand them in a Fourier series,

$$u(x, t) = \hat{a}_0(t) + \sum_{n=1}^{\infty} \hat{a}_n(t) \cos nx + \hat{b}_n(t) \sin nx,$$

$$z(x, t) = \hat{c}_0(t) + \sum_{n=1}^{\infty} \hat{c}_n(t) \cos nx + \hat{d}_n(t) \sin nx.$$

and plug into equations (1),(2). First, a direct substitution into the dynamics of u yields

$$\begin{aligned} & \hat{a}'_0 + \sum_{n=1}^{\infty} \hat{a}'_n \cos(nx) + \hat{b}_n \sin(nx) \\ &= -\hat{a}_0 - \left[\sum_{n=1}^{\infty} \hat{a}_n \cos nx + \hat{b}_n \sin nx \right] \\ &+ A \int_{\Omega} f(u(y, t)) dy \\ &+ B \cos(x) \int_{\Omega} \cos(y) f(u(y, t)) dy \\ &+ B \sin(x) \int_{\Omega} \sin(y) f(u(y, t)) dy \\ &+ \varepsilon \left[q(C + D \cos(x)) - g \left(\hat{c}_0(t) + \sum_{n=1}^{\infty} \hat{c}_n(t) \cos nx + \hat{d}_n(t) \sin nx \right) \right]. \end{aligned}$$

We have used the elementary trigonometric identity $\cos(x-y) = \cos(x)\cos(y) + \sin(x)\sin(y)$ to separate the kernel into multiple integrals. A direct substitution into the dynamics of z yields

$$\begin{aligned}\hat{a}'_0 &+ \sum_{n=1}^{\infty} \hat{a}'_n \cos(nx) + \hat{b}_n \sin(nx) \\ &= \varepsilon\beta \left[-\hat{c}_0(t) - \sum_{n=1}^{\infty} \hat{c}_n(t) \cos nx + \hat{d}_n(t) \sin nx \right. \\ &\quad \left. + \hat{a}_0(t) + \sum_{n=1}^{\infty} \hat{a}_n(t) \cos nx + \hat{b}_n(t) \sin nx \right]\end{aligned}$$

Next, we group like terms in the Fourier basis, starting with the Fourier coefficients of u :

$$\begin{aligned}\hat{a}'_0 &= -\hat{a}_0 + A \int_{\Omega} f(u(y, t)) dy + \varepsilon[qC - g\hat{c}_0] \\ \hat{a}'_1 &= -\hat{a}_1 + B \cos(x) \int_{\Omega} \cos(y) f(u(y, t)) dy + \varepsilon[qD - g\hat{c}_1] \\ \hat{a}'_2 &= -\hat{a}_2 + \varepsilon[-g\hat{c}_2] \\ \hat{a}'_3 &= -\hat{a}_3 + \varepsilon[-g\hat{c}_3] \\ &\vdots\end{aligned}$$

and

$$\begin{aligned}\hat{b}'_1 &= -\hat{b}_1 + B \sin(x) \int_{\Omega} \sin(y) f(u(y, t)) dy + \varepsilon[-g\hat{d}_1] \\ \hat{b}'_2 &= -\hat{b}_2 + \varepsilon[-g\hat{d}_2] \\ \hat{b}'_3 &= -\hat{b}_3 + \varepsilon[-g\hat{d}_3] \\ &\vdots\end{aligned}$$

We repeat this grouping for the Fourier coefficients of z :

$$\begin{aligned}\hat{c}_0 &= \varepsilon\beta(-\hat{c}_0 + \hat{a}_0) \\ \hat{c}_1 &= \varepsilon\beta(-\hat{c}_1 + \hat{a}_1) \\ &\vdots\end{aligned}$$

and

$$\begin{aligned}\hat{d}_0 &= \varepsilon\beta(-\hat{d}_0 + \hat{b}_0) \\ \hat{d}_1 &= \varepsilon\beta(-\hat{d}_1 + \hat{b}_1) \\ &\vdots\end{aligned}$$

The pattern is clear at this point: The coefficients of all Fourier modes greater than 1 satisfy

$$\begin{aligned} a'_i &= -a_i - \varepsilon g b_i, \\ b'_i &= \varepsilon \beta (-b_i + a_i), \end{aligned}$$

where a_i are placeholders for the Fourier coefficients of u and b_i are placeholders for the Fourier coefficients of z . Through an elementary stability analysis, all solutions to these equations decay to zero so they are unnecessary to consider. We proceed with the remaining nontrivial terms,

$$\begin{aligned} u(x, t) &= a_0(t) + a_1(t) \cos x + a_2(t) \sin x, \\ z(x, t) &= b_0(t) + b_1(t) \cos x + b_2(t) \sin x. \end{aligned}$$

Note that these are still the first two Fourier modes, but we have dropped the hat notation and relabeled the coefficients. Using this notation, we have the system

$$\begin{aligned} a'_0 &= -a_0 + A \int_{\Omega} f(u(y, t)) dy + \varepsilon(qC - g b_0), \\ a'_1 &= -a_1 + B \int_{\Omega} \cos(y) f(u(y, t)) dy + \varepsilon(qD - g b_1), \\ a'_2 &= -a_2 + B \int_{\Omega} \sin(y) f(u(y, t)) dy - \varepsilon g b_2, \\ b'_i &= \varepsilon \beta (-b_i + a_i), \quad i = 0, \dots, 2. \end{aligned}$$

Note that we do not need to explicitly write the full Fourier series of f or extract any of its coefficients. In fact, the Fourier modes of $f(u)$ greater than 1 vanish as we will now show.

Consider the Fourier series of $f(u(x, t))$:

$$f(u(x, t)) = \hat{\alpha}_0(t) + \sum_{n=1}^{\infty} \hat{\alpha}_n(t) \cos(nx) + \hat{\beta}_n(t) \sin(nx)$$

This expansion exists because f is bounded and integrable on $[0, 2\pi]$. We now evaluate each integral, $\int_{\Omega} f(u(y, t)) dy$, $\int_{\Omega} \cos(y) f(u(y, t)) dy$, and $\int_{\Omega} \sin(y) f(u(y, t)) dy$ in turn. First,

$$\begin{aligned} \int_{\Omega} f(u(y, t)) dy &= \int_{\Omega} \alpha_0 + \sum_{n=1}^{\infty} \alpha_n \cos(ny) + \beta_n \sin(ny) dy \\ &= \alpha_0 \int_{\Omega} dy + \sum_{n=1}^{\infty} \alpha_n \int_{\Omega} \cos(ny) dy + \beta_n \int_{\Omega} \sin(ny) dy \\ &= 2\pi \alpha_0. \end{aligned}$$

Next,

$$\begin{aligned}
\int_{\Omega} \cos(y) f(u(y, t)) dy &= \cos x \int_{\Omega} \cos(y) \left[\alpha_0 + \sum_{n=1}^{\infty} \alpha_n \cos(ny) + \beta_n \sin(ny) \right] dy \\
&= \alpha_0 \cos x \int_{\Omega} \cos(y) dy + \sum_{n=1}^{\infty} \alpha_n \int_{\Omega} \cos(y) \cos(ny) dy + \beta_n \int_{\Omega} \cos(y) \sin(ny) dy \\
&= \pi \alpha_1
\end{aligned}$$

and finally,

$$\begin{aligned}
\int_{\Omega} \sin(y) f(u(y, t)) dy &= \sin x \int_{\Omega} \sin(y) \left[\alpha_0 + \sum_{n=1}^{\infty} \alpha_n \cos(ny) + \beta_n \sin(ny) \right] dy \\
&= \alpha_0 \sin x \int_{\Omega} \sin(y) dy + \sum_{n=1}^{\infty} \alpha_n \int_{\Omega} \sin(y) \cos(ny) dy + \beta_n \int_{\Omega} \sin(y) \sin(ny) dy \\
&= \pi \beta_1.
\end{aligned}$$

Thus, the nonlinearity f in the integrand only appears in the dynamics of the first few Fourier coefficients. At each time step in the numerics, we compute the integrals $\int_{\Omega} f(u(y, t)) dy$, $\int_{\Omega} \cos(y) f(u(y, t)) dy$, and $\int_{\Omega} \sin(y) f(u(y, t)) dy$ using Riemann integration at each time step as it is more straightforward than extracting the necessary Fourier coefficients.

We focus our numerical studies on the coefficients a_1 and a_2 because they produce the most salient features of the bump solution (the a_0 coefficient changes as a function of time, but only up to order $O(\varepsilon)$, while the b_i terms represent aggregate behavior of the adaptation variable z). By following the fixed points and oscillatory behavior in a_1 and a_2 , we produce a bifurcation diagram of this system in Figure 4.

Figure 4 shows that there are three main solution types: the pinned or stationary bump, the sloshing bump, and the traveling bump, which traverses the ring at some finite speed. In addition there are small regions of bistability between the sloshing bump and the traveling bump.

3.2 Phase Model on the Ring

We now turn to the analysis of the phase dynamics on the ring. The analysis to follow depends on proving the following statements:

1. $H(0) = 0$,
2. $H'(0) > 0$,
3. If $K(x) = A + B \cos(x)$, then $H(\theta) = A' \sin(\theta)$, $A' > 0$, where A' depends on the parameters A, B .

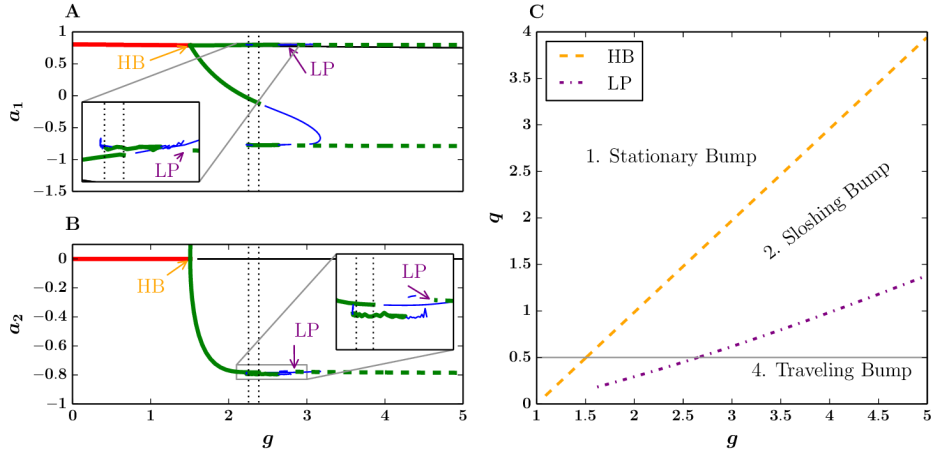


Figure 4: 1- and 2-parameter bifurcation diagrams of the neural field model on the ring. Solid red lines: Stable equilibrium. Solid Green: Stable periodic solutions. Solid blue: Unstable periodic solutions. Solid black: unstable equilibrium. (A,B) Bifurcation diagram in a_1 and a_2 for fixed $q = 0.5$. As g increases from 0 to 5, the system undergoes a Hopf bifurcation (HB, orange). Solutions here slosh with a small deviation from the origin. By increasing g , we see a region of bistability (shown in the insets with the interval of bistability marked by vertical dotted black lines), marking the emergence of large-sloshing solutions alongside sloshing solutions. Next, the system reaches a limit point (LP, purple) beyond which there exists a traveling bump solution. For panel B, the branches of the Hopf bifurcation are symmetric over the x -axis, thus we only show one branch. C: Two parameter bifurcation diagram in g and q . To the left of the Hopf bifurcation (HB, dashed orange line), there is only a stationary bump solution (1.). Motion exists to the right of this dividing line in the form of sloshes (2.) and a traveling bump solution (4.).

Recall the scalar version of the functions $H_i(\boldsymbol{\theta})$ and $v_i^*(\mathbf{x})$:

$$H(\theta) = \int_{\Omega} u^*(y) u_0(y + \theta) dy$$

$$u^*(x) = f'(u_0(x)) u'_0(x),$$

Because u_0 is even, it follows that $f'(u_0)$ is even, u'_0 is odd, and therefore u^* is odd. Noting that

$$H(0) = \int_{\Omega} u^*(y) u_0(y) dy,$$

where the function $u^*(y) u_0(y)$ is odd, the first statement follows.

For the second statement, we follow the definitions to arrive at

$$H'(0) = \int_{\Omega} f'(u_0(y)) u'_0(y) u'_0(y) dy.$$

The function f is an increasing sigmoidal, thus $f' > 0$. In addition, $u_0'^2 > 0$. Thus, $H'(0) > 0$.

Next, we prove the third statement. With the kernel choice $K(x) = A + B \cos(x)$, the steady-state bump solution is some shifted multiple of cosine, $u_0(x) = C + D \cos(x)$, where C, D implicitly depend on the kernel parameters A, B . Plugging this u_0 into $H(\theta)$ yields

$$H(\theta) = \int_{-\pi}^{\pi} f'(C + D \cos(y)) [-D \sin(y)] [C + D \cos(y + \theta)] dy.$$

Let $h(y) = f'(C + D \cos(y)) [D \sin(y)]$, which is an odd function. Recalling that $\cos(y + x) = \cos(y) \cos(x) - \sin(y) \sin(x)$, H simplifies to

$$H(\theta) = -C \int_{-\pi}^{\pi} h(y) dy - \int_{-\pi}^{\pi} h(y) D [\cos(y) \cos(\theta) - \sin(y) \sin(\theta)] dy.$$

Because $h(y)$ is odd, some integrals cancel, and we are left with

$$H(\theta) = A' \sin(\theta),$$

where $A' = D \int_{-\pi}^{\pi} h(y) \sin(y) dy$.

From these statements, it follows that $\frac{dJ}{d\theta}|_{\theta=\bar{\theta}} < 0$ and $J(\bar{\theta}) = 0$ where $\bar{\theta}$ represents a steady-state bump peak. WLOG, we let $\bar{\theta} = 0$ because we generally choose the center of the steady-state bump to be the origin.

Remark: For the more general adaptation (c.f. above), as long as $M(u)$ is differentiable and monotonically increasing, we still have that $H'(0) > 0$.

3.2.1 Equivalent Phase Model on the Ring

We next show that there are really only two relevant parameters. We can rescale time to obtain

$$\mu\beta \frac{d\theta}{d\tau} = qJ(\theta) - g \int_0^\infty e^{-s} H(\theta(\tau-s) - \theta(\tau)) ds,$$

where we have re-used τ as the now scaled time $\beta\tau$. Next, divide by $\mu\beta$ to obtain

$$\frac{d\theta}{d\tau} = \hat{q}J(\theta) - \hat{g} \int_0^\infty e^{-s} H(\theta(\tau-s) - \theta(\tau)) ds, \quad (11)$$

with $\hat{q} = \frac{q}{\mu\beta}$ and $\hat{g} = \frac{g}{\mu\beta}$. This rearrangement shows that making adaptation slower by decreasing β is equivalent to increasing the rescaled parameters

\hat{g} and \hat{q} . For analytic calculations, we will often reference this equation without the hats on the parameters.

For numerical studies of bifurcations in this system, we let $H(\theta) = A' \sin \theta$, from which J follows immediately (see Equation (10) and statement 2 above). We once more abuse notation and absorb A' into \hat{g} and into \hat{q} , then drop the hats. So we will now study

$$\frac{d\theta}{d\tau} = -q \sin(\theta) - g \int_0^\infty e^{-s} \sin(\theta(\tau-s) - \theta(\tau)) ds,$$

To numerically integrate this phase equation, we rewrite this differential equation as a system of three equations by exploiting basic differentiation properties of integrals. To begin, we use a trigonometric identity to rewrite the integral in the right-hand side

$$\begin{aligned} \frac{d\theta}{d\tau} &= -q \sin(\theta) - g \int_0^\infty e^{-s} \sin(\theta(\tau-s) - \theta(\tau)) ds \\ &= -q \sin(\theta) - g[\cos(\theta)S(\tau) - \sin(\theta)C(\tau)], \end{aligned}$$

where

$$\begin{aligned} S(\tau) &= \int_0^\infty e^{-s} \sin(\theta(\tau-s)) ds, \\ C(\tau) &= \int_0^\infty e^{-s} \cos(\theta(\tau-s)) ds. \end{aligned}$$

With the change of variables $s' = \tau - s$, S, C become

$$\begin{aligned} S(\tau) &= \int_{-\infty}^{\tau} e^{-(\tau-s')} \sin(\theta(s')) ds', \\ C(\tau) &= \int_{-\infty}^{\tau} e^{-(\tau-s')} \cos(\theta(s')) ds'. \end{aligned}$$

By differentiating, we rewrite S and C as ODEs:

$$\begin{aligned} \frac{dS}{d\tau} &= -S(\tau) + \sin \theta, \\ \frac{dC}{d\tau} &= -C(\tau) + \cos \theta. \end{aligned}$$

We have transformed a single integro-differential equation into a system of three ODEs, simplifying the numerics considerably:

$$\begin{aligned} \frac{d\theta}{d\tau} &= -q \sin(\theta) - g[\cos(\theta)S(\tau) - \sin(\theta)C(\tau)] \\ \frac{dS}{d\tau} &= -S(\tau) + \sin \theta, \\ \frac{dC}{d\tau} &= -C(\tau) + \cos \theta. \end{aligned}$$

The bifurcation diagram in Figure 5 summarizes the dynamics of the phase model on the ring. On the left panel, we fix a parameter value $q = 0.5$ and as we vary the parameter g , the system transitions from steady-state to sloshing solutions, then to a co-existence of large-amplitude and relatively small amplitude sloshing solutions, and eventually to a steady traveling pulse. On the right panel, we find that the parameter space is separated into several regions. In particular, for $q \geq 0$ arbitrarily small, there exists a traveling bump for some nonzero g .

In the following sections, we analyze the existence of these bifurcations including the Hopf bifurcation leading to sloshing solutions, and the saddle-node bifurcation leads to the constant-velocity traveling bump.

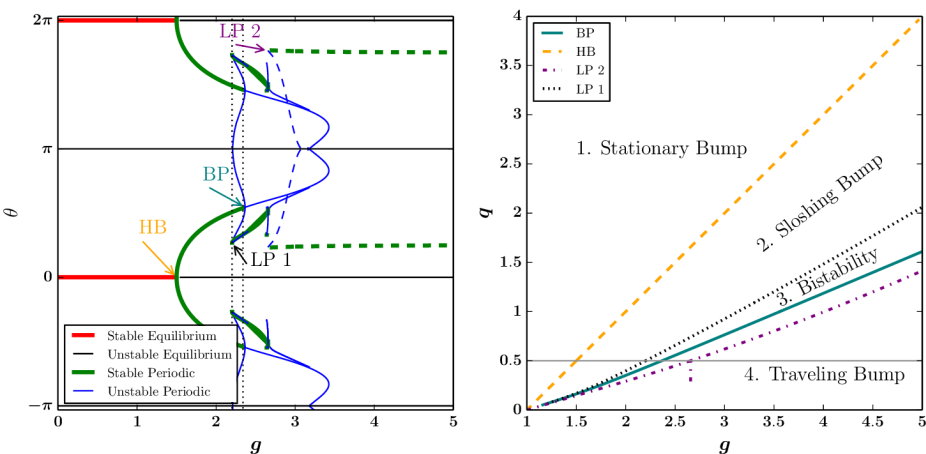


Figure 5: 1- and 2-parameter bifurcation diagrams of the phase equation on the ring. (A,B) Bifurcation diagram in for fixed $q = 0.5$. As g increases from 0 to 5, the system undergoes a Hopf bifurcation (HB, orange) then produces a limit point (LP 1, black), a branch point (BP, teal), and another limit point (LP 2, purple), respectively. Between the limit point LP1 and branch point BP, there is bistability, the interval of which is denoted by vertical dotted black lines. Beyond the second limit point LP2, there exists a traveling bump solution. This traveling bump solution is distinct from the equilibria and periodic solutions denoted by solid lines, thus we label it with a dashed green line. B: Two parameter bifurcation diagram in g and q . To the left of the Hopf bifurcation (HB, dashed orange line), there is only a stationary bump solution (1.). Motion exists to the right of this dividing line in the form of sloshes (2., 3.) and a traveling bump solution (4.).

3.3 Constant Velocity Bump Solution on the Ring

To show the existence of a constant velocity traveling bump solution, we require that $q = 0$ and $g > 0$. For the first part of this analysis, we do not require the kernel to take a particular form. We only require the kernel to be even and admit a steady-state bump solution to Equation (1). We make a traveling bump ansatz, $\theta(\tau) = \nu\tau$, where ν corresponds to the traveling bump velocity. We first determine the existence and stability of the zero velocity bump solution. Plugging the ansatz into Equation (11) yields

$$\begin{aligned}\nu &= -g \int_0^\infty e^{-s} H(-\nu s) ds \\ &= g \int_0^\infty e^{-s} H(\nu s) ds,\end{aligned}\tag{12}$$

where the last line follows by the oddness of H . Because $H(0) = 0$, $\nu = 0$ is a solution. To determine the stability of the zero velocity solution, we consider a small perturbation, $\theta(\tau) = \nu\tau + \varepsilon\psi$. By plugging this perturbation into Equation (11), we extract the dynamics of the perturbed variable ψ ,

$$\frac{d\psi}{d\tau} = -g \int_0^\infty e^{-s} H'(\nu s) [\psi(\tau - s) - \psi(\tau)] ds.\tag{13}$$

Assuming $\psi(\tau) = e^{\lambda\tau}$ and $\nu = 0$, we obtain the stability equation,

$$\lambda = -g \int_0^\infty e^{-s} H'(0) [e^{-\lambda s} - 1] ds.$$

We integrate the right-hand side and rearrange to yield

$$\lambda = gH'(0) \frac{\lambda}{1 + \lambda}.$$

Thus, either $\lambda = 0$, or $\lambda = -1 + gH'(0)$. Moreover, the zero velocity solution becomes unstable when $g > 1/H'(0)$.

In general, we may view the relationship between g and ν by rearranging Equation (12) into the function

$$g = \Gamma(\nu) := \frac{\nu}{\int_0^\infty e^{-s} H(\nu s) ds}.\tag{14}$$

We show examples of Γ in Figure 6. In the left panel, the relationship between the adaptation strength g and bump velocity ν is straightforward: as g increases, there is some critical value ν where a nonzero velocity traveling bump exists. However, the choice of kernel may change the shape of Γ , and therefore change the relationship between g and ν , as well as the stability of traveling bump solutions. For example, a kernel of the form $K(x) = a + b \cos(x) + c \cos(2x)$ results in an H function of the form

$$H(\theta) = a' \sin(\theta) + b' \sin(2\theta).$$

Using this H function to plot Γ results in the right panel of Figure 6. The branch with negative slope represents another traveling bump solution. We now show that if $\Gamma'(\nu) < 0$, then the traveling bump with velocity ν is unstable.

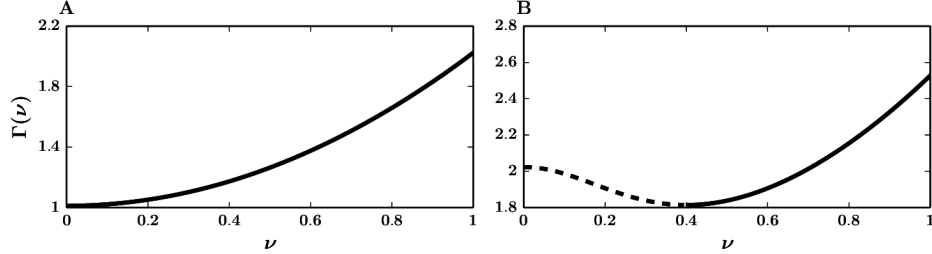


Figure 6: Examples of the function $\Gamma(\nu)$. A: Γ constructed using our usual H function, $H(x) = \sin(x)$. B: Γ constructed using a different H function, $H(x) = \sin(x) - 0.25 \sin(2x)$, resulting from a different choice of kernel. The dashed black line represents an unstable traveling bump velocity.

Recall again Equation (13). Assuming $\psi(\tau) = e^{\lambda\tau}$ and $\nu \neq 0$, we obtain the stability equation,

$$f(\lambda) \equiv 1 + g \int_0^\infty e^{-s} H'(\nu s) \left[\frac{e^{-\lambda s} - 1}{\lambda} \right] ds. \quad (15)$$

To prove the statement, we seek to show that $\lim_{\lambda \rightarrow \infty} f(\lambda) > 0$ and $\lim_{\lambda \rightarrow 0} f(\lambda) < 0$. Then by continuity of f , there exists a positive root to Equation (15). We take each limit in turn, starting with the limit as $\lambda \rightarrow \infty$.

$$\begin{aligned} \lim_{\lambda \rightarrow \infty} f(\lambda) &= 1 + g \int_0^\infty e^{-s} H'(\nu s) \lim_{\lambda \rightarrow \infty} \left[\frac{e^{-\lambda s} - 1}{\lambda} \right] ds \\ &= 1 > 0. \end{aligned}$$

Thus, the positive λ limit is positive. For the other limit, we rearrange Equation (14) into

$$\Gamma(\nu)D(\nu) = \nu,$$

where $D(\nu) = \int_0^\infty e^{-\beta s} H(\nu s) ds$, and differentiate with respect to ν to obtain

$$\Gamma(\nu)D'(\nu) + \Gamma'(\nu)D(\nu) = 1.$$

Solving for $\Gamma'(\nu)$ yields

$$\Gamma'(\nu) = \frac{1 - \Gamma(\nu)D'(\nu)}{D(\nu)}.$$

Note that $D(\nu) > 0$ at least within a neighborhood of $\nu = 0$ since $H(0) = 0$ and $H'(0) > 0$. In addition, $D'(\nu) = \int_0^\infty e^{-s} H'(\nu s) s ds$. Using the hypothesis that $\Gamma'(\nu) < 0$, we have the inequality

$$1 < \Gamma(\nu) D'(\nu).$$

We use this fact in the next limit

$$\begin{aligned} \lim_{\lambda \rightarrow 0} f(\lambda) &= 1 + g \int_0^\infty e^{-s} H'(\nu s) \lim_{\lambda \rightarrow 0} \left[\frac{e^{-\lambda s} - 1}{\lambda} \right] ds \\ &= 1 - g \int_0^\infty e^{-s} H'(\nu s) s ds \\ &= 1 - g D'(\nu) \\ &= 1 - \Gamma(\nu) D'(\nu) < 0. \end{aligned}$$

Thus, the zero λ limit is negative. Because $f(0)$ is negative, and $f(\lambda)$ is positive for asymptotically large values of λ , there exists a positive root λ of $f(\lambda)$ by continuity. It follows that branches of $\Gamma(\nu)$ with negative slope indicate an unstable traveling bump at least within a neighborhood of $\nu = 0$.

For the next part of this analysis, we show how to compute a formula for the velocity of the traveling bump when the kernel is $K(x) = A + B \cos(x)$. With this kernel, the H function is proportional to $\sin(x)$, and Equation (12) becomes explicitly computable. Computing the integral results in a formula for the nontrivial bump velocity ν ,

$$\nu = \pm \sqrt{g - 1}. \quad (16)$$

Equation (16) corresponds to the branches of a pitchfork bifurcation in the velocity of the traveling bump. We show a particular example of a constant-velocity traveling bump in Figure 7A. We note that any odd H will lead to a pitchfork bifurcation to a traveling bump. In particular, it is trivial to derive the following bifurcation equation:

$$\nu^2 = (1 - gH'(0))/gH'''(0).$$

This equation tells us that the pitchfork bifurcation is super-critical if $H'''(0) < 0$ and sub-critical otherwise.

3.4 Andronov-Hopf Bifurcation on the Ring

We now prove the existence of a Hopf bifurcation. For this analysis, we do not require H or J to take a particular form. However, we do require that H and J be sufficiently differentiable, along with the properties $H(0) = J(0) = 0$, $H'(0) > 0$, $J'(0) < 0$, H odd, and $g, q > 0$.

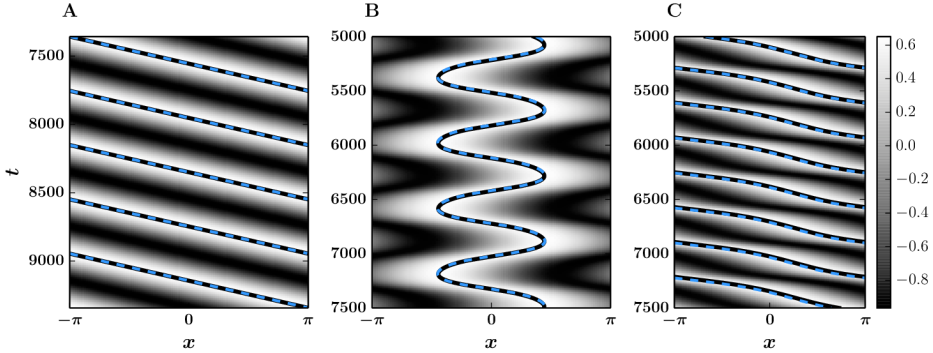


Figure 7: Dynamics of the traveling bump on the ring. Each row represents the bump solution at a particular time. White represents high activity, while black represents low or inhibited activity. The numerical centroid (black solid) is plotted against the analytic prediction (dashed blue). A: A constant-velocity bump, $g = 3.5, q = 0$. B: A sloshing bump, $g = 3, q = 1$. C: A non-constant velocity bump, $g = 5.5, q = 1$. For each panel, we shift the theory along the time axis to show qualitative agreement with the numerics. Parameter $\varepsilon = 0.01$.

Consider again the simplified phase model, Equation (11). Let us fix q and absorb the parameter into J . We write J and H as Taylor expansions,

$$J(\theta) = j_1\theta + j_2\theta^2 + j_3\theta^3,$$

$$H(\theta) = h_1\theta + h_3\theta^3.$$

Then to first order,

$$\frac{d\theta}{d\tau} = j_1\theta - gh_1 \int_0^\infty e^{-s}[\theta(\tau-s) - \theta(\tau)]ds.$$

Letting $\theta = e^{\lambda t}$ and rearranging the resulting equation yields

$$\lambda = j_1 + gh_1 - \frac{gh_1}{\lambda + 1},$$

or equivalently,

$$\lambda^2 + \lambda(1 - j_1 - gh_1) - j_1 = 0.$$

Since $j_1 < 0$ and $h_1 > 0$, there exists a Hopf bifurcation when

$$g^* = \frac{1 - j_1}{h_1}.$$

This bifurcation leads to oscillations in the peak of the bump solution. We show a particular example of this oscillatory behavior in Figure 7B.

3.4.1 Normal Form for the Hopf Bifurcation on the Ring

We wish to analyze the bifurcation to a sloshing pulse for the general integral equation:

$$\frac{d\theta}{d\tau} = -qJ(\theta) - g \int_0^\infty e^{-s} H(\theta(\tau-s) - \theta(\tau)) ds \quad (17)$$

as g increases. For simplicity, we will assume $J(\theta)$ is an odd periodic function (as is the case for $H(\theta)$) and through suitable rescaling of g, q , we will assume:

$$\begin{aligned} J(\theta) &= \theta + j_3\theta^3 + \dots \\ H(\theta) &= \theta + h_3\theta^3 + \dots \end{aligned}$$

We also assume $q > 0$ so that $\theta = 0$ is stable without adaptation. If, we use $H(\theta) = J(\theta) = \sin(\theta)$, then $j_3 = h_3 = -(1/6)$. The linearization about $\theta = 0$ has the form:

$$\theta_\tau = -q\theta - g \int_0^\infty e^{-s} (\theta(\tau-s) - \theta(\tau)) ds$$

which has the general solution, $e^{\lambda\tau}$. After some simplification, we find that

$$\lambda^2 + (1 + q - g)\lambda + q = 0$$

so there is an imaginary eigenvalue, $i\sqrt{q} := i\omega$ when $g = 1 + q \equiv g_0$, so we expect a Hopf bifurcation will occur.

All nonlinearities are odd, so we can assume the multiple timescale expansion

$$g = g_0 + \delta^2 g_2, \quad \theta = \delta\theta_1(\zeta, \xi) + \delta^3\theta_3(\zeta, \xi),$$

where δ is the amplitude of the bifurcating solution, $\zeta = \tau$ is a “fast” time, and $\xi = \delta^2\tau$ is a “slow” time. We detail the remaining steps of the normal form analysis in Appendix A and jump to the conclusion,

$$\alpha \frac{dz}{d\xi} = z[\hat{\gamma}_0 + \hat{\gamma}_3|z|^2] \quad (18)$$

where

$$\begin{aligned} \alpha &= 1 - \frac{g_0}{1 + 2i\omega - \omega^2} = \frac{2}{1 + q}(q + \sqrt{q}i) \\ \hat{\gamma}_0 &= g_2 \frac{i\omega}{1 + i\omega} = \frac{g_2}{1 + q}(q + \sqrt{q}i) \\ \hat{\gamma}_3 &= \frac{3q}{4q + 1} [[q(12h_3 - 4j_3) - j_3] + i18h_3\sqrt{q}] . \end{aligned}$$

To get the actual normal form, we divide (18) by α , to obtain:

$$\frac{dz}{d\xi} = z(g_2/2 + \gamma_3|z|^2)$$

where

$$\gamma_3 = \frac{3}{8q+2} [q(12qh_3 - 4qj_3 - j_3 + 6h_3) + i\sqrt{q}(6qh_3 - 4qj_3 - j_3)].$$

If we assume that $j_3 = h_3$ as would be the case if the input was the bump, itself, then

$$\gamma_3 = h_3 \frac{3q(8q+5)}{8q+2} - ih_3 \frac{3\sqrt{q}(2q-1)}{8q+2}.$$

We compare the normal form calculation to the numerics in Figure 8. We use XPPAUT0 to compute the numerical bifurcation diagram. As expected, the normal form approximation is quite accurate near the bifurcation.

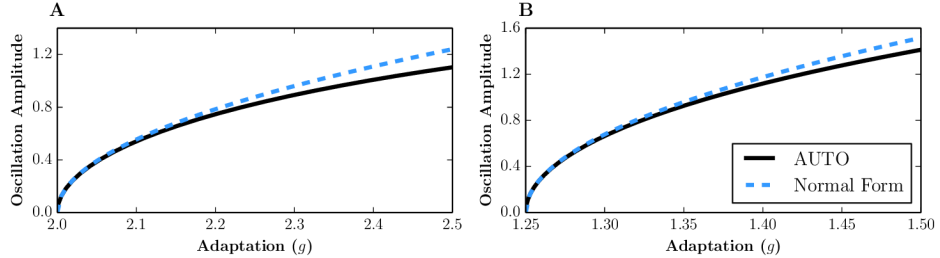


Figure 8: Normal form calculation for the neural field model on the ring. A: Amplitude of oscillations predicted by the normal form calculation (dashed blue) compared to the actual amplitude (solid black). $q = 1$. B: Amplitude of oscillations predicted by the normal form calculation (dashed blue) compared to the actual amplitude (solid black). $q = 0.25$.

3.5 Non-Constant Velocity Bump Solution on the Ring

When adaptation is made even stronger, the solution breaks free from the oscillating state and travels across the periodic domain (Figure 7C. The onset is shown numerically in the bifurcation diagrams of Figures 4 and 5, purple LP2). Due to the pinning term, the velocity of the bump is nonconstant.

Remark. As $q \rightarrow 0$, we see in figure 5B that all the two-parameter curves converge to the point g^* which is the point of onset of the traveling bumps with no input stimulus.

3.6 Chaos on the Ring

With $g, q > 0$, there exists a small parameter range in which the neural field exhibits chaotic movement about the ring. Examples of this behavior are shown in Figure 9. In both panels, the initial conditions differ by 1e-7. The solutions in each panel remain nearly identical for a long time (we have truncated a significant portion of the simulation).

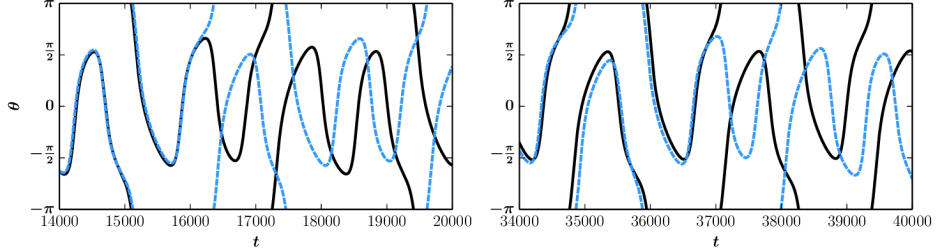


Figure 9: Chaotic dynamics of the traveling bump in the full neural field model (left) and the reduced phase model (right) on the ring. Original solutions are shown in black. Solutions with a different initial condition is shown in dashed blue. For each panel, initial conditions differ by 1e-7. A: $g = 2.65, q = 0.5$. B: $g = 2.661, q = 0.5$. For all simulations in this figure, $\varepsilon = 0.01$.

This section completes our analysis of the one-dimensional case. We have found a good match between the phase-reduced equations and the full neural model. For a fixed amplitude of the external input, we find a transition from a stationary bump to ‘‘sloshers’’, and, finally to bumps that move completely around the ring, modulated traveling bumps. In the sections to follow, we repeat the analytical and numerical analysis for the two-dimensional domain.

4 Torus Domain

In this section, we define the domain Ω as the torus, or the square $[-\pi, \pi] \times [-\pi, \pi]$ with periodic boundary conditions. We seek to analyze the full neural field model on this domain using the same bifurcation analysis performed in the one-dimensional case. We begin by considering simplifications that allow us to use standard bifurcation analysis tools like **XPPAUT0**.

4.1 Approximation of the Neural Field Model on the Torus

In order to numerically investigate the full neural field equation (1-2), we need to either discretize space in two-dimensions or use an approximation of the kernel that is degenerate. (Since the integral operator is compact, it can be approximated to arbitrary precision by a degenerate integral operator ;see section 2.8 [29]). Thus to study the dynamics of the full neural field model on a two-dimensional domain, we take a Fourier truncation of the kernel to make the integral in Equation (3) separable. This truncation allows us to rewrite the infinite dimensional system as a finite system of ODEs and use traditional dynamical systems tools like **XPPAUT0** to analyze the system. To

begin, take the truncated Fourier approximation to the kernel,

$$K(x, y) = k_{00} + k_{10} \cos(x) + k_{01} \cos(y) + k_{11} \cos(x) \cos(y), \quad (19)$$

and plug it into Equation (3):

$$u(\mathbf{x}) = \int_{\Omega} K(x_1 - y_1, x_2 - y_2) f(u(\mathbf{y})) d\mathbf{y}.$$

After expanding the kernel using standard trigonometric identities, we derive the time-varying solutions

$$\begin{aligned} u(\mathbf{x}, t) &= a_{00}(t) + a_{10}(t) \cos(x_1) + a_{01}(t) \cos(x_2) \\ &\quad + b_{10}(t) \sin(x_1) + b_{01}(t) \sin(x_2) \\ &\quad + a_{11}(t) \cos(x_1) \cos(x_2) + b_{11}(t) \sin(x_1) \sin(x_2) \\ &\quad + c_1(t) \sin(x_1) \cos(x_2) + c_2(t) \cos(x_1) \sin(x_2). \end{aligned} \quad (20)$$

$$\begin{aligned} z(\mathbf{x}, t) &= E_{00}(t) + E_{10}(t) \cos(x_1) + E_{01}(t) \cos(x_2) \\ &\quad + F_{10}(t) \sin(x_1) + F_{01}(t) \sin(x_2) \\ &\quad + E_{11}(t) \cos(x_1) \cos(x_2) + F_{11}(t) \sin(x_1) \sin(x_2) \\ &\quad + G_1(t) \sin(x_1) \cos(x_2) + G_2(t) \cos(x_1) \sin(x_2). \end{aligned}$$

where the coefficients satisfy

$$\begin{aligned} a'_{ij} &= -a_{ij} + k_{ij} p_{ij}(t) + \varepsilon(qu_{ij} - gE_{ij}), \\ b'_{ij} &= -b_{ij} + k_{ij} r_{ij}(t) - \varepsilon gF_{ij}, \\ c'_i &= -c_i + k_{11}s_i(t) - \varepsilon gG_i, \\ \xi' &= \varepsilon\beta(-\xi + \zeta), \end{aligned} \quad (21)$$

where $i = 0, 1$ and $j = 0, 1$. The dummy variables ξ, ζ represent each of the pairs (a_{ij}, E_{ij}) , (b_{ij}, F_{ij}) , and (c_i, G_i) . The time-varying functions p_{ij}, r_{ij}, s_i are defined as

$$\begin{aligned} p_{00}(t) &= \int_{\Omega} f(u(\mathbf{y}, t)) d\mathbf{y} & p_{01} &= \int_{\Omega} \cos(y_2) f(u(\mathbf{y}, t)) d\mathbf{y} \\ p_{10}(t) &= \int_{\Omega} \cos(y_1) f(u(\mathbf{y}, t)) d\mathbf{y} & p_{11} &= \int_{\Omega} \cos(y_1) \cos(y_2) f(u(\mathbf{y}, t)) d\mathbf{y} \\ r_{01}(t) &= \int_{\Omega} \sin(y_2) f(u(\mathbf{y}, t)) d\mathbf{y} & r_{10} &= \int_{\Omega} \sin(y_1) f(u(\mathbf{y}, t)) d\mathbf{y} \\ r_{11}(t) &= \int_{\Omega} \sin(y_1) \sin(y_2) f(u(\mathbf{y}, t)) d\mathbf{y} \\ s_1(t) &= \int_{\Omega} \cos(y_1) \sin(y_2) f(u(\mathbf{y}, t)) d\mathbf{y} & s_2 &= \int_{\Omega} \sin(y_1) \cos(y_2) f(u(\mathbf{y}, t)) d\mathbf{y}, \end{aligned}$$

and the coefficients u_{ij} are taken from the truncated Fourier series of the steady-state solution,

$$u_0(x, y) = u_{00} + u_{10} \cos(x) + u_{01} \cos(y) + u_{11} \cos(x) \cos(y).$$

The coefficient values of the kernel and steady-state bump solutions are shown in Tables 2 and 3, respectively. Details on how we approximate the spatial integrals of p_{ij}, r_{ij}, s_i are in Appendix C.

We show the bifurcation diagram and salient solutions of this system in Figure 10. The only bifurcations classified by AUTO are a subcritical Hopf bifurcation (HB, orange) and limit points (limit points occur at each change in stability of periodic solutions). The Hopf bifurcation leads to small amplitude unstable solutions. We attribute the existence of a subcritical Hopf bifurcation to the coarse discretization of the spatial domain in the parameters of Equation (21). Although not shown here, a finer discretization of the spatial domain using 200 intervals results in a qualitatively supercritical Hopf bifurcation.

To summarize, we find the usual types of oscillatory solutions in this truncated neural field model as we found in the neural field model. A stable limit cycle of this system is shown in the first bottom left panel (A, which corresponds to the initial conditions taken from the point A in the bifurcation diagram). A large-sloshing solution exists for slightly larger g (B,C), and eventually, for sufficiently large g , there exist only traveling bump solutions D. Additional non-periodic attractors are shown in panels E–G. The attractors shown in this figure are simply those with the largest basins of attraction. Generally, starting random initial conditions with g anywhere in the range $1.55 < g < 1.95$ (the gray shaded area labeled F in the main plot) results in solutions that qualitatively match panel F. The same holds for the shaded areas E and F, with their corresponding panels. Indeed, there exist several attractors not shown in this figure that are more difficult to find numerically. However, the focus of this study is not the thorough classification of attractors in the truncated neural field model, so we move on to the analysis of the phase model on the torus.

4.2 Approximations of the Phase Model on the Torus

We now turn to the analysis of the phase dynamics in two-dimensions and begin by reducing the number of parameters with the same rescaling used to obtain Equation (11) in the one dimensional case,

$$\frac{d\theta_i}{d\tau} = qJ_i(\boldsymbol{\theta}) - g \int_0^\infty e^{-s} H_i(\boldsymbol{\theta}(\tau - s) - \boldsymbol{\theta}(\tau)) ds, \quad i = 1, 2, \quad (22)$$

and recall that

$$H_i(\boldsymbol{\theta}) = \int_{\Omega} f'(u_0(\mathbf{x})) \partial_i u_0(\mathbf{x}) u_0(\mathbf{x} + \boldsymbol{\theta}) d\mathbf{x}.$$

Details on the numerical integration of the integro-differential equation, Equation (22), are shown in Appendix C.

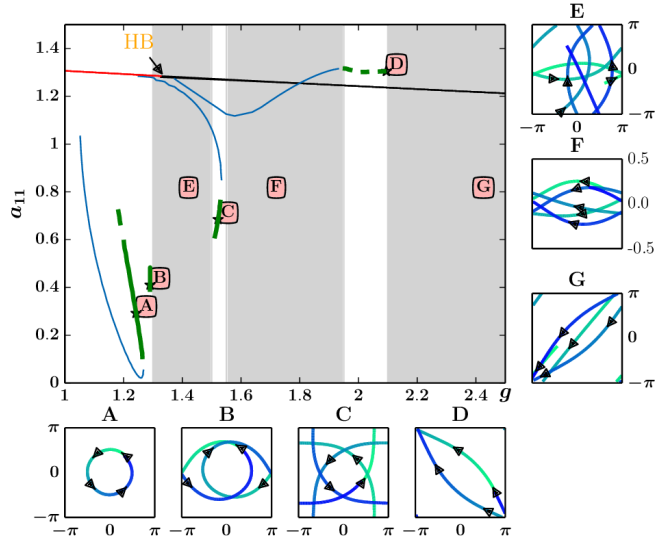


Figure 10: Bifurcation diagram of the truncated neural field model on the torus with g as a bifurcation parameter and $q = 0.1$. The stable fixed point (red line) undergoes a subcritical Hopf bifurcation (HB, orange) and becomes an unstable fixed point (black line). The green and blue lines represent stable and unstable oscillations, respectively. Thick, solid green lines represent stable oscillations that wrap around the torus. Thick, dashed green lines represent unstable periodic solutions. Stable attractors are shown in panels A–D. In panels E–G, we show solutions in parameter regimes without stable periodic attractors. These solutions are displayed in a relatively short time window after integrating for long times and travel from light to dark. In panel E ($g = 1.4$), we integrate for $t = 5000$ time units and show the last 30% of the data. In panel F ($g = 1.7$), we integrate for $t = 8000$ time units and show the last 10% of the data. In panel G ($g = 2.4$), we integrate for $t = 8000$ time units and show the last 6% of the data. We initialize the solutions of panels E–F using standard normally distributed random variables. Parameter $\varepsilon = 0.01$.

To facilitate the study of existence and stability of solutions, we consider two approximations to H_i to be used in Equation (22): the first is a high-accuracy Fourier series of H_i , and the second is a low-accuracy Fourier series of H_i . We detail these approximations in turn.

For the accurate Fourier series approximation of H_i , we use one of two

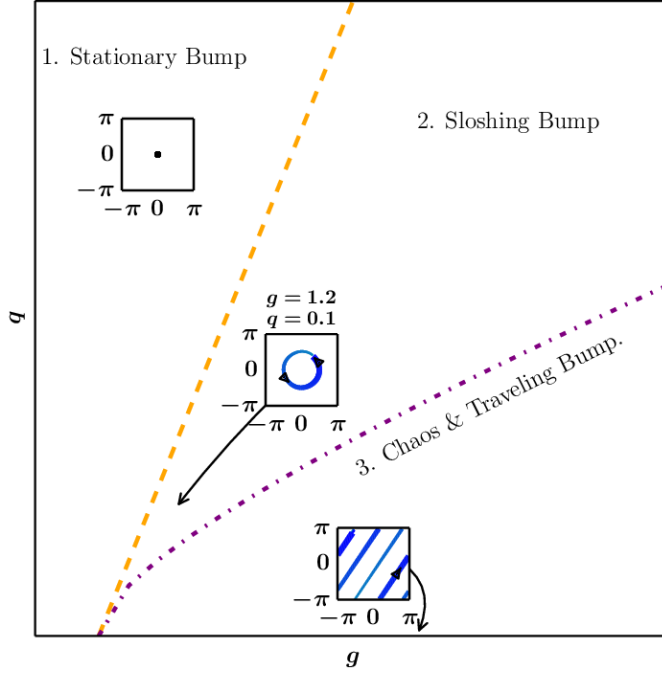


Figure 11: Cartoon of the parameter space of the approximate neural field model on the torus (Equation (21)). The most salient solutions are shown. Solutions advance in time from light to dark, thin to thin. For sufficiently small g or sufficiently large q , the bump solution tends to a stationary solution. By increasing g or decreasing q to $g = 1.2, q = 0.1$, the centroid of the bump solution oscillates about the origin. For larger g , say $g = 4, q = 0.5$, the solution begins to traverse chaotically about the domain. When $q = 0$, there exists a constant velocity traveling bump solution for g sufficiently large, e.g., $g = 3$. Parameter $\varepsilon = 0.01$.

equivalent forms

$$H_1(\boldsymbol{\theta}) = \sum_{n,m \in \mathbb{Z}} a_{nm} \sin(n\theta_1) \cos(m\theta_2), \quad (23)$$

where, due to the odd (even) property of the first (second) coordinate, the coefficients have the property that $a_{n,\pm m} = -a_{-n,\pm m}$. We can then rewrite this Fourier series into the equivalent form,

$$H_1(\boldsymbol{\theta}) = \sum_{n,m \in \mathbb{Z}} \hat{a}_{nm} \sin(n\theta_1 + m\theta_2), \quad (24)$$

where $\hat{a}_{nm} = 4a_{nm}$. This equivalent form makes integrals much easier to compute. We use both forms interchangeably as we see fit, and abuse notation in Equation (24) by removing the hats from the coefficients. We find

that 30 Fourier coefficients provides a sufficiently good approximation for simulations on a 64×64 domain (the error is on the order of 1e-7).

For the low-accuracy Fourier series, we consider a more substantial truncation of the interaction function using only 3 Fourier coefficients. While this truncation is drastic, it allows us to analyze Equation (22) more rigorously. We derive the 3 term H_i -function starting with the same Fourier truncation of the kernel as above, which leads to the same steady-state bump solution,

$$u_0(x, y) = u_{00} + u_{10} \cos(x) + u_{01} \cos(y) + u_{11} \cos(x) \cos(y),$$

which in turn leads to a truncated H_i function,

$$H_1^F(\theta_1, \theta_2) = \sin(\theta_1)(h_{10} + h_{11} \cos(\theta_2)),$$

where

$$\begin{aligned} h_{10} &= 4u_{10} \int_{\Omega} \sin^2(x)(u_{10} + 2 \cos(y)u_{11}) dx dy, \\ h_{11} &= 8u_{11} \int_{\Omega} \cos(y) \sin^2(x)(u_{10} + 2 \cos(y)u_{11}) dx dy. \end{aligned}$$

For simplicity, analysis of this H_i function uses the simpler form

$$H_1^F(\theta_1, \theta_2) = \sin(\theta_1)(1 + b \cos(\theta_2)), \quad (25)$$

where we have absorbed h_{10} into the parameter g of Equation (22), and relabeled h_{11}/h_{10} as b . Naturally, it follows that $H_2^F(x, y) = H_1^F(y, x)$ and $H_i^F = -J_i^F$.

Using the truncated interaction function H_1^F enables us to use traditional dynamical systems tools and techniques to identify qualitative dynamics of Equation (22) through a bifurcation analysis.

Finally, for H_i and all of its approximations, we require the following properties to hold:

1. $\partial H_1(0, 0)/\partial y = \partial H_2(0, 0)/\partial x = 0$,
2. $\partial H_1(0, 0)/\partial x, \partial H_2(0, 0)/\partial y > 0$,
3. $\partial J_1(0, 0)/\partial x, \partial J_2(0, 0)/\partial y < 0$.

Properties 1 and 2 follow from the evenness of the $\varepsilon = 0$ bump solution and 3 is made WLOG since we could just change the sign of q otherwise.

To summarize, we consider two approximations to H_i :

$$\begin{aligned} H_1(\boldsymbol{\theta}) &= \sum_{n,m=1}^{30} a_{nm} \sin(n\theta_1) \cos(m\theta_2) \propto \sum_{n,m=1}^{30} a_{nm} \sin(n\theta_1 + m\theta_2), \\ H_1^F(\boldsymbol{\theta}) &= \sin(\theta_1)(1 + b \cos(\theta_2)). \end{aligned}$$

We note that the second approximation, H_1^F , is a result of using the truncated kernel in Equation (19).

4.2.1 Equivalent Truncated Phase Model on the Torus

For the truncated function H_i^F , we transform the delay integro-differential equations into a system of ordinary differential equations using identical arguments used to transform the phase equation on the ring from a delay integro-differential equation into a system of ODEs. The new system is

$$\begin{aligned}\theta'_i &= qJ_i^F(\boldsymbol{\theta}) - g(\eta_{i1} + \eta_{i2}), \quad i = 1, 2 \\ N' &= -N + P \\ M' &= -M + Q\end{aligned}\tag{26}$$

where

$$\begin{aligned}(N, P) &\in \{(cx, \cos \theta_1), (cy, \cos \theta_2), (sx, \sin \theta_1), (sy, \sin \theta_2)\} \\ (M, Q) &\in \{(sxsy, \sin(\theta_1) \sin(\theta_2)), (sxcy, \sin(\theta_1) \cos(\theta_2)), \\ &\quad (cxsy, \cos(\theta_1) \sin(\theta_2)), (cxcy, \cos(\theta_1) \cos(\theta_2))\} \\ \eta_{11} &= sx \cos(\theta_1) - cx \sin(\theta_1) \\ \eta_{12} &= b[\cos(\theta_1) \cos(\theta_2) sx cy - \sin(\theta_1) \cos(\theta_2) cx cy \\ &\quad + \cos(\theta_1) \sin(\theta_2) sx sy - \sin(\theta_1) \sin(\theta_2) cx sy].\end{aligned}$$

The function η_{21} (η_{22}) is the same as η_{12} (η_{11}) with θ_1 and θ_2 flipped and each x and y flipped in the notation (for example, $sxcy$ and $\cos(\theta_2)$ in η_{12} become $sycx$ and $\cos(\theta_1)$ in η_{21} , respectively).

We show the many bifurcations and salient solutions of this system in Figure 12. We find that there exists a stable sloshing bump solution that arises from a Hopf bifurcation (solution A, bifurcation HB). Due to the symmetry of the system, there is also an unstable sloshing solution in an axial direction (G) that arises from the same Hopf bifurcation. For slightly larger parameter values, there is bistability of large-sloshing solutions (H and B), and an even larger-sloshing solution (F) that loses stability through a torus bifurcation (TR). For this choice of $q = 0.1$, the solutions are chaotic for parameter values between the first torus bifurcation (TR1) and the first period doubling bifurcation (PD1). The multitude of period doubling bifurcations beyond this point represents the onset of chaotic behavior of the system due to the Fourier truncation, the error of which is proportional to g . This error is more apparent beyond limit point LP2 where there are no more traveling bump solutions, which qualitatively disagrees with the original system where traveling bump solutions exist for even relatively large g .

The most salient bifurcations are captured in the two-parameter bifurcation in Figure 13. There are several qualitative similarities to the two parameter bifurcation diagram of the phase model on the ring. In particular the transition from the stationary bump to the sloshing bump, and from sloshing to large-sloshing. However, for the two-dimensional domain, there are much larger regions of chaotic solutions.

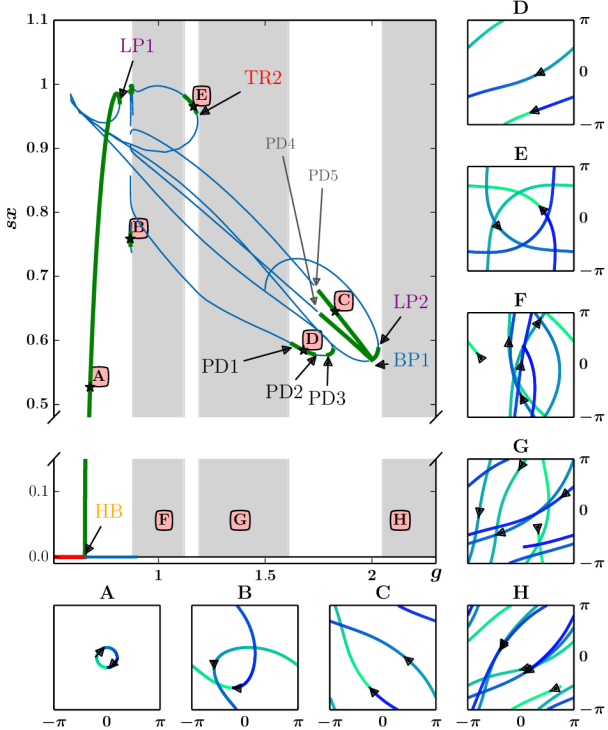


Figure 12: Bifurcation diagram of the equivalent truncated phase model on the torus over varying values of g with $q = 0.1$. Some branches refined using XPPY[26]. Sample solutions (labeled A–H in the bifurcation diagram) are shown in the subplots to the bottom and right of the diagram. Bifurcations are labeled according to the type: Hopf (HB), limit point (LP), torus (TR), period-doubling (PD), and branch point (BP). The number following each bifurcation type correspond to the same bifurcation type and number in the two parameter bifurcation in Figure 13. Panels A–E show stable attractors. In panels F–H, we show solutions in parameter regimes without stable periodic attractors. These solutions are displayed in a relatively short time window after integrating for long times and travel from light to dark. In panel F ($g = 1.05$), we integrate for $t = 500$ time units and show the last 9% of the data. In panel F ($g = 1.5$), we integrate for $t = 500$ time units and show the last 7% of the data. In panel G ($g = 2.15$), we integrate for $t = 500$ time units and show the last 5% of the data. We initialize the solutions of panels F–H using standard normally distributed random variables. Parameter $\varepsilon = 0.01$.

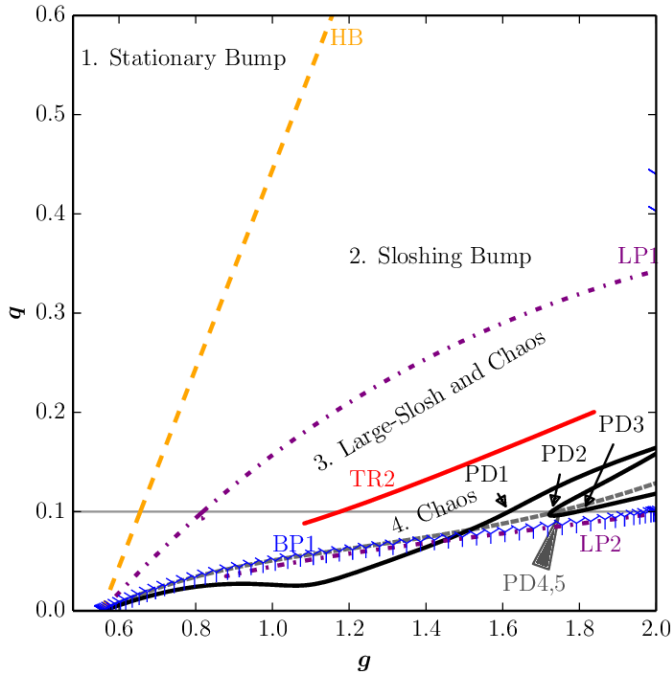


Figure 13: Two parameter bifurcation diagram of the equivalent truncated phase model on the torus. The parameter regions are separated into stationary solutions (1.), sloshing solutions (2.), large-sloshing solutions (3.), and generally chaotic solutions (4.). To the right of the curve LP2 (purple dashed) for $g \geq 1.5$, the qualitative behavior breaks down as this bifurcation point marks the end of traveling bump solutions. Parameter $b = 0.8$.

In the following sections, we study the dynamics of the original phase model and the truncated phase model and repeat most of the analysis as completed in the ring domain. In particular, using a combination of numerical and analytical methods, we analyze the existence and stability of traveling bump solutions, and the existence of a Hopf bifurcation.

4.3 Constant Velocity Bump Solution on the Torus

In this section, we analyze the existence and stability of constant velocity bump solutions on the torus for $q = 0$, the only case in which there can be constant velocity traveling bumps. Figure 14 shows the type of solutions we analyze in this section: constant velocity traveling bump solutions in the full neural field model (panel A), the reduced model with the accurate Fourier approximation (panel B), and the truncated reduced model (panel C).

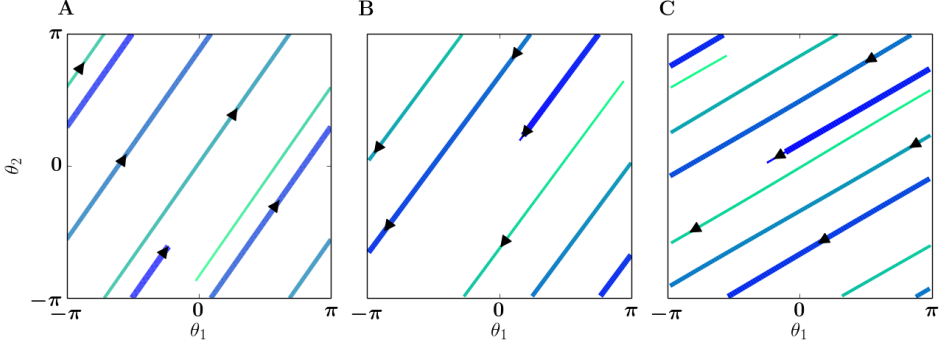


Figure 14: Constant velocity dynamics of the traveling bump on the torus. The curve that goes from light to dark and thin to thick represents the movement of the centroid over time. A: Full neural field model on the torus, $q = 0, g = 3$, simulated for $t = 7000$ time units with the last 60% of the data shown. B: Phase model on the torus with the accurate Fourier series of H_i , $q = 0, g = 2.2$, simulated for $t = 6,700$ time units with the last 10% of the data shown. C: Phase model on the torus with the truncated Fourier series H_i^F , $q = 0, g = 2.5$, simulated for $t = 3,500$ time units with the last 20% of the data shown. For these parameter choices, the axial directions are unstable and over long times converge to non-axial directions. Parameter $\varepsilon = 0.01$.

4.3.1 Existence

To show existence of solutions in the axial directions, we only need to show existence of the solution $\theta_1(\tau) = \nu\tau$ and $\theta_2(\tau) = 0$. We plug this ansatz into (22) and rearrange to yield

$$g = \Gamma(\nu) \equiv \frac{\nu}{\int_0^\infty e^{-s} H_1(\nu s, 0) ds}. \quad (27)$$

The analysis of this equation is identical to the one-dimensional case, Equation (14). By varying ν from zero, we can find the values of g where there are solutions. Values of g for which ν is nonzero imply there exists a traveling bump solution. In the case of the truncated H function, we compute this integral explicitly to derive the velocity ν as a function of adaptation strength g :

$$\Gamma(\nu) = \frac{1 + \nu^2}{1 + b}.$$

To determine the critical value for the existence of axial constant velocity bump solutions, we take the limit $\lim_{\nu \rightarrow 0} \Gamma(\nu)$:

$$g^* = \lim_{\nu \rightarrow 0} \Gamma(\nu) = \frac{1}{1 + b}.$$

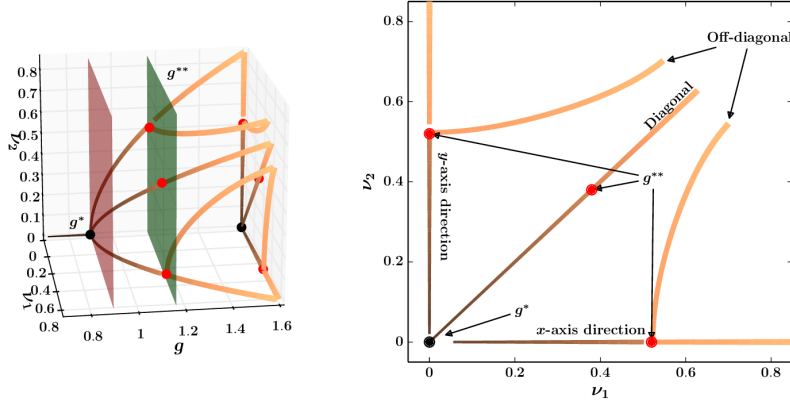


Figure 15: Existence of traveling bump solutions using the accurate approximation to the interaction function H_i . Left: After a first critical value (g^*) of the bifurcation parameter g (red plane), there exist traveling bumps in the axial directions. After a second critical value (g^{**}) (marked by a green plane), off-diagonal solutions form and continue to persist for large g . The dark to light color gradient and thin to thick thickness gradient corresponds to increasing values of g . Right: The projection of the branches on the left onto the $g = 1.6$ plane. A given point on one of these branches marks the magnitude and direction of a traveling bump. If necessary, one can approximate the parameter value g of this traveling bump by looking at the thickness and color of the chosen point and looking back at the branches in the left panel.

To show existence of non-axial solutions, we use the ansatz $\theta_1(\tau) = \nu_1\tau$ and $\theta_2(\tau) = \nu_2\tau$ where $\nu_1, \nu_2 \neq 0$. There exist non-axial traveling bump solutions if ν_1, ν_2 simultaneously satisfy

$$\begin{aligned} 0 &= -\nu_1 + gG(\nu_1, \nu_2), \\ 0 &= -\nu_2 + gG(\nu_2, \nu_1), \end{aligned} \tag{28}$$

where

$$G(\nu_1, \nu_2) = \int_0^\infty e^{-s} H_1(\nu_1 s, \nu_2 s) ds.$$

We can not compute the velocities ν_1, ν_2 explicitly as a function of g , but we can exploit the Fourier series of H_i to compute G explicitly, allowing us to use XPPAUT0 to follow the velocities as a function of the adaptation parameter g . The existence of traveling solutions using the accurate Fourier series is shown in Figure 15, and the existence of traveling solutions using the truncated Fourier series is shown in Figure 16.

In these figures, we find that the truncated model (Figure 16) exhibits a similar set of traveling bump solutions as the full phase model (Figure

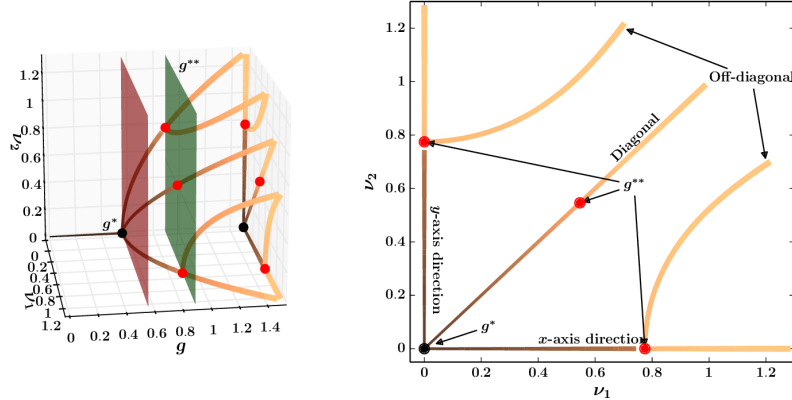


Figure 16: Existence of traveling bump solutions using the truncated interaction function H_i^F ($q = 0, b = 0.8$). Left: After a first critical value (g^*) of the bifurcation parameter g (red plane), there exist traveling bumps in the axial directions. After a second critical value (g^{**}) (marked by a green plane), off-diagonal solutions form and continue to persist for large g . The dark to light color gradient and thin to thick thickness gradient corresponds to increasing values of g . Right: The projection of the branches on the left onto the $g = 4$ plane. A given point on one of these branches marks the magnitude and direction of a traveling bump. If necessary, one can approximate the parameter value g of this traveling bump by looking at the thickness and color of the chosen point and looking back at the branches in the left panel.

15). In particular, each system at a critical value g^* , bifurcates into two axial solutions and one diagonal solution. For larger g , the system bifurcates again at another critical value g^{**} , giving rise to two non-axial, non-diagonal constant velocity directions. Indeed, negative velocity solutions exist, but as these solutions are symmetric up to multiples of a 90-degree rotation about the g -axis, we only show the positive directions. The “mixed” solutions that branch off for $g > g^{**}$ are, in general, not rationally related so that the resulting traveling bumps will densely cover the torus. As such quasi-periodic solutions are often not structurally stable, we expect to see complex and possibly chaotic behavior when $q > 0$. Indeed, looking at Figure 13, we see that most of the complex behavior occurs for a small value of q and g sufficiently large.

Now that we have shown existence of traveling bump solutions, we proceed with a stability analysis.

4.3.2 Stability

We begin this section with stability of traveling bump solutions in the axial directions. We perturb off the axial solution, $\theta_1(\tau) = \nu\tau + \varepsilon e^{\lambda_1\tau}$ and $\theta_2(\tau) = 0 + \varepsilon e^{\lambda_2\tau}$, with $\text{Re}(\lambda_i) > -1$. The first order terms yield two independent eigenvalue problems

$$\begin{aligned}\lambda_1 &= -g \int_0^\infty e^{-s} \frac{\partial H_1}{\partial x}(\nu s, 0)[e^{-\lambda_1 s} - 1]ds, \\ \lambda_2 &= -g \int_0^\infty e^{-s} \frac{\partial H_1}{\partial x}(0, \nu s)[e^{-\lambda_2 s} - 1]ds,\end{aligned}$$

which we combine with Equation (27) to yield two independent eigenvalue equations,

$$\begin{aligned}\lambda_1 &= -\frac{\nu}{\int_0^\infty e^{-s} H_1(\nu s, 0) ds} \int_0^\infty e^{-s} \frac{\partial H_1}{\partial x}(\nu s, 0)[e^{-\lambda_1 s} - 1]ds, \\ \lambda_2 &= -\frac{\nu}{\int_0^\infty e^{-s} H_1(\nu s, 0) ds} \int_0^\infty e^{-s} \frac{\partial H_1}{\partial x}(0, \nu s)[e^{-\lambda_2 s} - 1]ds.\end{aligned}$$

Using these equations, we may determine stability of a traveling bump solution as a function of its velocity. We rephrase this problem and consider the independent scalar valued functions

$$\Lambda_1(\nu, \lambda) = \lambda + \frac{\nu}{\int_0^\infty e^{-s} H_1(\nu s, 0) ds} \int_0^\infty e^{-s} \frac{\partial H_1}{\partial x}(\nu s, 0) (e^{-\lambda s} - 1) ds, \quad (29)$$

$$\Lambda_2(\nu, \lambda) = \lambda + \frac{\nu}{\int_0^\infty e^{-s} H_1(\nu s, 0) ds} \int_0^\infty e^{-s} \frac{\partial H_1}{\partial x}(0, \nu s) (e^{-\lambda s} - 1) ds. \quad (30)$$

For a given Λ_i , the zero level curves in (ν, λ) space determine stability properties of traveling bump solutions.

We begin the analysis of these equations using the accurate Fourier series of H_i and compute the integrals explicitly. The zero level set of the resulting function is shown in Figure 17. On the left panel, find that for any velocity, the x -direction is always stable. On the right, we find that for sufficiently small velocities, $\theta_2(\tau) = 0$ is a stable solution. Thus, constant velocity traveling solutions in this parameter regime will converge to the x -axis. Finally, for greater traveling bump velocities, the vertical direction loses stability, giving rise to non-axial solutions.

With the truncated H_i , which we recall to be $H_i^F(\theta_1, \theta_2) = \sin(\theta_1)(1 + b \cos(\theta_2))$, we may compute the equations $\Lambda_i = 0$ explicitly as polynomials,

$$\begin{aligned}0 &= \lambda_1^2 + \lambda_1 + 2\nu^2 \\ 0 &= \lambda_2^3 + c_2 \lambda_2^2 + c_1 \lambda_2 + c_0,\end{aligned}$$

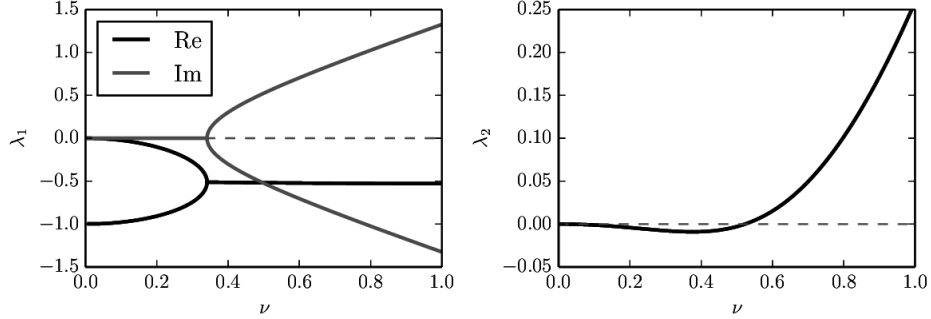


Figure 17: Stability of solutions in the horizontal axial direction (calculated using the phase model with the accurate Fourier series). Both plots show the level curves where $\text{Re}(\Lambda_i) = 0$ (black) and $\text{Im}(\Lambda_i) = 0$ (gray). For small velocities ν , both components are stable. For larger velocities, the horizontal velocity remains stable, but the vertical velocity loses stability. The dashed gray line shows where $\lambda_i = 0$.

where

$$\begin{aligned} c_0 &= \frac{(2b-1)\nu^2 - \nu^4}{b+1}, \\ c_1 &= \frac{(1+b+(2b-1)\nu^2)}{b+1}, \\ c_2 &= \frac{(2(b+1)-\nu^2)}{b+1}. \end{aligned} \quad (31)$$

The coefficients of Equation (31) determine the stability of the horizontal traveling solution. Note that for ν sufficiently small, all coefficients are positive and the product c_1c_2 dominates the coefficient c_0 . Thus, for small velocities, the coefficients have the properties $c_1c_2 > c_0$ and $c_2, c_0 > 0$, which implies stability by the Routh Hurwitz criterion. When $\nu^* = \pm\sqrt{2b-1}$, the coefficient c_0 is no longer positive and the stability condition fails.

We have found that horizontal traveling bump solutions lose stability at some critical velocity ν^* , giving rise to non-axial traveling bump solutions. By symmetry, this argument holds for vertical traveling bump solutions: after the same critical ν^* , constant velocity traveling bumps in the vertical direction lose stability and become non-axial solutions.

Now that we understand the existence of and stability of axial constant velocity traveling solutions, we turn our attention to the stability of non-axial traveling bump solutions.

To determine the stability of non-axial directions, we consider the solution, $\theta_1(\tau) = \nu\tau + \phi_1 e^{\lambda\tau}$ and $\theta_2(\tau) = \nu\tau + \phi_2 e^{\lambda\tau}$. This ansatz results in the

equations,

$$\begin{aligned}\lambda\phi_1 &= -g\phi_1 \int_0^\infty Q_1(s) (e^{-\lambda s} - 1) ds - g\phi_2 \int_0^\infty Q_2(s) (e^{-\lambda s} - 1) ds, \\ \lambda\phi_2 &= -g\phi_1 \int_0^\infty Q_3(s) (e^{-\lambda s} - 1) ds - g\phi_2 \int_0^\infty Q_4(s) (e^{-\lambda s} - 1) ds,\end{aligned}$$

where

$$\begin{aligned}Q_1(s) &= \int_0^\infty e^{-s} \frac{\partial H_1}{\partial x}(-\nu_1 s, -\nu_2 s), & Q_2(s) &= \int_0^\infty e^{-s} \frac{\partial H_1}{\partial y}(-\nu_1 s, -\nu_2 s), \\ Q_3(s) &= \int_0^\infty e^{-s} \frac{\partial H_1}{\partial y}(-\nu_2 s, -\nu_1 s), & Q_4(s) &= \int_0^\infty e^{-s} \frac{\partial H_1}{\partial x}(-\nu_2 s, -\nu_1 s).\end{aligned}$$

By rewriting the integrals in the more compact form,

$$\begin{aligned}\lambda\phi_1 &= -g\phi_1 \hat{Q}_1(\lambda) - g\phi_2 \hat{Q}_2(\lambda), \\ \lambda\phi_2 &= -g\phi_1 \hat{Q}_3(\lambda) - g\phi_2 \hat{Q}_4(\lambda),\end{aligned}$$

where $\hat{Q}_i = \int_0^\infty Q_i(s) (e^{-\lambda s} - 1) ds$, the problem reduces to finding an eigenvector $(\phi_1, \phi_2)^T$ with corresponding eigenvalue $-\lambda$:

$$g \begin{pmatrix} \hat{Q}_1(\lambda) & \hat{Q}_2(\lambda) \\ \hat{Q}_3(\lambda) & \hat{Q}_4(\lambda) \end{pmatrix} \begin{pmatrix} \phi_1 \\ \phi_2 \end{pmatrix} = -\lambda \begin{pmatrix} \phi_1 \\ \phi_2 \end{pmatrix}. \quad (32)$$

This condition holds if and only if the determinant

$$\mathcal{E}(\lambda) = \left| g \begin{pmatrix} \hat{Q}_1(\lambda) & \hat{Q}_2(\lambda) \\ \hat{Q}_3(\lambda) & \hat{Q}_4(\lambda) \end{pmatrix} + \lambda I_2 \right| \quad (33)$$

is zero. This determinant is the Evans function, and we use its roots to determine stability properties of the constant velocity solutions.

Using the accurate Fourier series of H_i , the integrals of the eigenvalue problem (32) are explicitly computable. Given a value g , it is straightforward to compute the contours of $\mathcal{E} = 0$ using a standard contour plot routine. In panels A and B of Figure 18, we show the Evans function when $g = 1.5$, and $g = 3$, respectively.

The domain values where the real part of the Evans function is zero is shown as a black contour, while the domain values where the imaginary part is zero is shown in gray. Intersections of these contours show roots of the Evans function. Generally, there exists a root of the Evans function at the origin due to translation invariance of the underlying bump solution. Thus we ignore this root and consider only those nontrivial roots with real part sufficiently greater than -1 . These nontrivial roots are marked with red dots.

We follow these roots using **XPPAUTO** and generate the bifurcation diagram shown in the right panel of Figure 18. The real part of the root

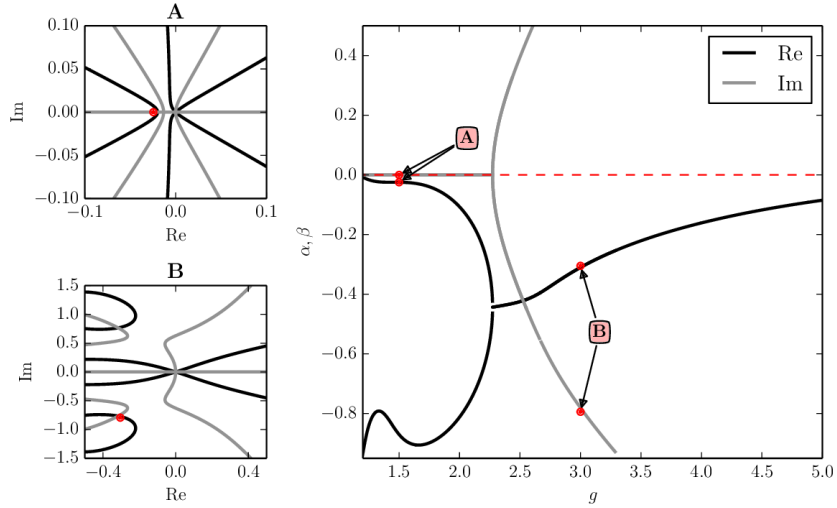


Figure 18: Evans function for the accurate Fourier series H . Left panels A and B: roots of the real (black) and imaginary (gray) parts of the evans function for $g = 1.5$ and $g = 3$, respectively. Intersections of the gray and black lines denote zeros of the Evans function. We use α and β to denote the real and imaginary part of the Evans function, respectively. Right panel: The real and imaginary parts of the nontrivial root(s) of the Evans function for various choice of g . The horizontal red dashed line denotes the real axis.

remains negative for the range of g that we consider, thus the constant traveling bump solution remains stable for a large range of adaptation strengths.

We repeat the analysis of the Evans function using the truncated Fourier interaction function, H^F . Once again, the integrals of the eigenvalue problem (32) are explicitly computable and we follow the roots of the Evans function using XPPAUTO in two parameters, b and g , the Fourier coefficient, and adaptation strength, respectively. The right panel of Figure 19 shows the result of this continuation: within the unstable region (marked in light blue), constant velocity solutions are unstable, as demonstrated by the lower inset showing θ_1 as a function of time. Because the instability arises through a Hopf bifurcation, the traveling bumps begin to “wobble”. In the stable region, bump solutions travel with constant velocity, as demonstrated by the upper inset showing θ_1 as a function of time.

The left panels (A and B) of Figure 19 demonstrates the existence of a Hopf bifurcation on the boundary between stable and unstable regions. These panels correspond to points labeled A and B on the right panel. In each case, we find a complex conjugate pair of eigenvalues that cross the imaginary axis.

In this section, we analyzed the reduced neural field model with nonzero

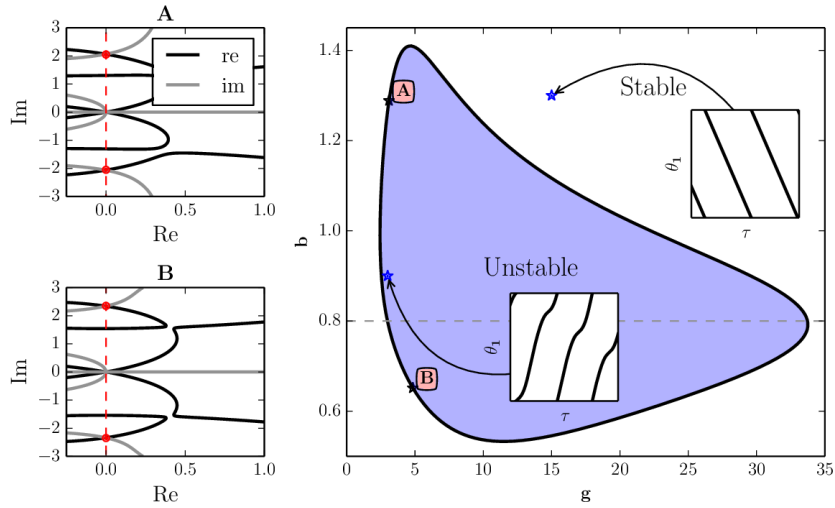


Figure 19: Evans function for the truncated interaction function H^F . Left panels A and B: roots of the real (black, $g = 3.1, b = 2.28$) and imaginary (gray, $g = 4.84, b = 0.65$) parts of the evans function demonstrating a loss of stability through a Hopf bifurcation. Intersections of the gray and black lines denote zeros of the Evans function. Right panel: the black line denotes where the real part of the Evans function is zero in b and g parameter space (i.e., where the bump solution loses stability). The points labeled A and B correspond to panels A and B, respectively. The horizontal dashed gray line shows our usual choice of the parameter value $b = 0.8$. Two insets with example solutions of $\theta_1(\tau)$ over slow time τ are shown, corresponding to the blue star in parameter space. In the stable region, the traveling bump solution moves with constant velocity (inset parameter values $g = 15, b = 1.3$ integrated over $t = 20000$ time units with the last 7.5% of the data shown). In the unstable region, the traveling bump solution loses stability through a Hopf bifurcation and begins to travel with nonconstant velocity (inset parameter values $g = 3, b = 0.9$ integrated over $t = 20000$ time units with the last 2.5% of the data shown). Parameter: $\varepsilon = 0.01$.

adaptation strength ($g > 0$) and no input current ($q = 0$). We now explore the dynamics arising from activating the time-invariant input current.

4.4 Hopf Bifurcation on the Torus

We have seen in Figures 13, 10 that for nonzero g and q , the system may produce a traveling bump solution that oscillates about the origin-centered input. For a fixed parameter value q , the origin is stable for $g = 0$, and with increasing g eventually becomes unstable through a Hopf bifurcation. We study this phenomenon with Equation (22), using the same technique

as used on the ring: linearization about the origin.

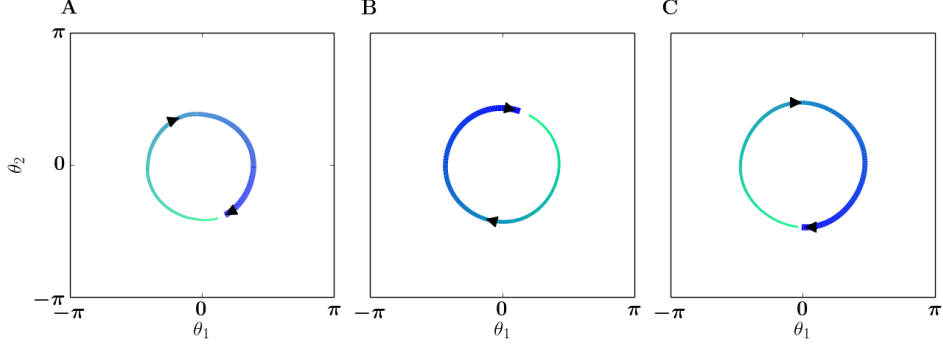


Figure 20: Limit cycle dynamics of the traveling bump on the torus. The curve that goes from light to dark and thin to thick represents the movement of the centroid over time. A: Full neural field model on the torus, $q = 2$, $g = 5$, period of $t = 805$ time units. B: Phase model on the torus with the accurate Fourier series approximation of H_i , $q = 1$, $g = 3$, period of $t = 187$ time units. C: Phase model on the torus with the truncated Fourier series H_i^F , $q = 0.2$, $g = 1$, period of $t = 370$ time units. Parameter $\varepsilon = 0.01$.

Let $(\theta_1(\tau), \theta_2(\tau)) = (e^{\lambda\tau}, e^{\lambda\tau})$. Plugging into Equation (22) results in a system of two decoupled equations,

$$\lambda = q\hat{J}_i^0 - g\hat{H}_i^0 \int_0^\infty e^{-s}(e^{-\lambda s} - 1)ds,$$

where

$$\begin{aligned}\hat{J}_i^0 &= \frac{\partial J_i}{\partial x}(0, 0) + \frac{\partial J_i}{\partial y}(0, 0), \\ \hat{H}_i^0 &= \frac{\partial H_i}{\partial x}(0, 0) + \frac{\partial H_i}{\partial y}(0, 0).\end{aligned}$$

Evaluating the integral and solving for λ yields

$$2\lambda = -(1 - q\hat{J}_i^0 - g\hat{H}_i^0) \pm \sqrt{(1 - q\hat{J}_i^0 - g\hat{H}_i^0)^2 + 4q\hat{J}_i^0}.$$

Thus, as in the case of the ring, for a fixed q and given g sufficiently large, there exists a Hopf bifurcation at the critical value

$$g = \frac{1 - q\hat{J}_i^0}{\hat{H}_i^0}.$$

For the truncated interaction function H_i^F , the critical value is

$$g = \frac{1 + q(1 + b)}{1 + b}.$$

4.5 Non-Constant Velocity Bump Solution on the Torus

As we have seen in earlier sections, stable oscillating solutions exist for particular choices of input current strength and adaptation on both the ring and torus. The similarities of solutions on the ring and torus continue as adaptation strength increases. On the ring, the oscillating solution gives way to a bump solution that travels around the ring with non-constant velocity. Similarly, with sufficiently large adaptation g , the bump solution on the torus also breaks free from the oscillating solution and traverses the domain with non-constant velocity. Figure 21 shows examples of these solutions in the full model (panel A), the phase model with the accurate Fourier series (panel B), and the phase model with the truncated Fourier series (panel C).

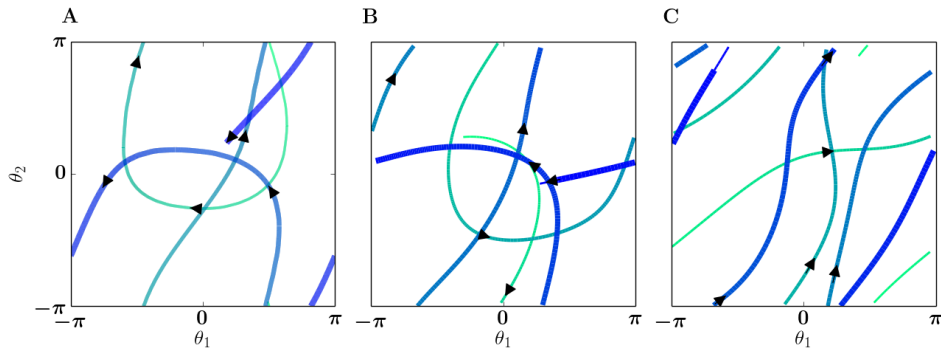


Figure 21: Non-constant velocity dynamics of the traveling bump on the torus. The curve that goes from light to dark and thin to thick represents the movement of the centroid over time. A: Full neural field model on the torus, $q = 1$, $g = 5$, simulated for $t = 5,000$ time units with the last 60% of the data shown. B: Phase model on the torus with the accurate Fourier series of H_i , $q = 1$, $g = 5$, simulated for $t = 6,700$ time units with the last 8% of the data shown. C: Phase model on the torus with the truncated Fourier series H_i^F , $q = .5$, $g = 4.5$, simulated for $t = 6,700$ time units with the last 7% of the data shown. Parameter: $\varepsilon = 0.01$.

There are plenty of other examples of these types of solutions (Figures 12, 11, 10) that are in fact chaotic. To demonstrate the existence of chaos numerically, we use the truncated phase model and a Poincaré section through $cy = 0$, as we find that generically the variable cy consistently crosses zero throughout simulations.

4.5.1 Chaos on the Torus

For a given g , we simulate the truncated phase model (Equation (26)) for $t = 150000$ time units and ignore the first 7000 time units to remove transients. By plotting the appropriate state variables, we are able to determine whether

a system is aperiodic (and possibly chaotic) or periodic. The top panel of Figure 22 shows one example of one such plot, where for each g value we plot all cy values for the duration of the simulation. The black regions of Figure 22 correspond to the gray regions of Figure 12: the approximate range $0.85 < g < 1.1$ corresponds to region **F**, the approximate range $1.18 < g < 1.61$ corresponds to region **G**, and the approximate range $g > 2.05$ corresponds to region **H**, respectively.

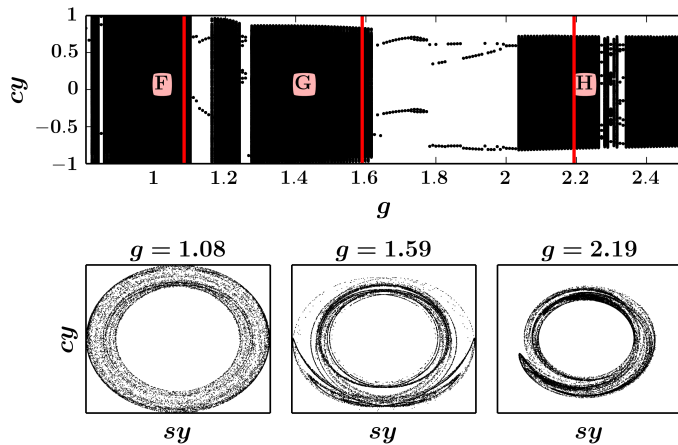


Figure 22: Chaotic attractors. Top panel: crude bifurcation diagram of cy as a function of parameter g . Black regions correspond to aperiodic and possibly chaotic behavior, while regions with dots correspond to periodic solutions. Parameter: $q = 0.1$.

We show sample solutions of the chaotic attractors in regions **F**, **G**, **H** in the bottom three panels of Figure 22. The vertical red line in the top panel denotes the parameter value corresponding to each attractor.

5 Discussion

Our motivation for this work was to understand the behavior of the model presented in [19] where the authors showed that heterogeneities in a recurrent network with adaptation produced a seemingly randomly moving bump of activity. Similar moving bump dynamics was also found in a homogeneous bump model with adaptation in [14]; here the authors report only axially moving bumps with no external inputs. The neural field model considered in this paper (Equations (1),(2)) is also capable of producing a rich variety of solutions on the ring and torus. On the ring, the centroid of the bump solution exhibits sloshing and large-sloshing behaviors (for moderate strengths of input current and adaptation) that, for stronger adaptation, lead to non-constant velocity traveling bump solutions. With

no input current and sufficient adaptation, the system generates a constant velocity traveling bump solution. We also observe chaotic solutions for a narrow range of adaptation strengths.

On the torus, the qualitative solutions are similar to those on the ring: Stationary bump solutions give rise to sloshing solutions (for moderate strengths of input current and adaptation), as well as non-constant velocity traveling bump solutions (with sufficient adaptation) and constant velocity traveling solutions (with no input current and sufficient adaptation). In this system, we do not see pulses that change in diameter with a fixed centroid (breathers) on the ring or torus.

Neural fields with nonsmooth firing rate functions (i.e., the Heaviside or rectifying nonlinearity) reproduce many of these qualitative behaviors. The existence and bifurcation of sloshing solutions on the ring are analyzed in [9, 6], and constant velocity solutions are shown to exist on the ring ([31, 6]), the real line ([24]), and the plane ([15]). Nonconstant velocity bump solutions are shown to exist in [6]. However, there are no studies showing the existence of aperiodic attractors on the torus (assuming a deterministic system with an even kernel), or the existence of chaos on the ring.

In this study, we contributed to the analysis of the known behaviors by using a smooth firing rate function and a caveat of weak and slow adaptation. This assumption on the adaptation variable allowed us to reduce the neural field model, which is a distributed partial integro-differential equation, to a system of scalar delay integro-differential equations describing the centroid of the bump solution. Moreover, our only restriction on the kernel is of Mexican-hat type. Put together, these assumptions and our results are more general than what currently exists in literature.

In one spatial dimension, for example, we derived the normal form for the Hopf bifurcation in the one-dimensional neural field model and determined the conditions for super- and sub-criticality. Although normal form calculations exist for neural field models on the ring or the real line, our calculation allows for a general choice of kernel and a smooth firing rate function (as opposed to a particular choice of kernel or a non-smooth Heaviside firing rate function [6, 9]).

As mentioned previously, existing studies require particular choices of kernels or Heaviside firing rate functions where a smooth firing rate function would be desirable ([2] note that a smooth firing rate function allows for a straightforward normal form analysis). Although these assumptions are restrictive, these studies have advantages that the current study does not address. In particular, our analysis requires that adaptation is weak and slow and that the input current is weak. As a result, we can only study phenomena that evolve on a slow timescale. These weak and slow assumptions are well-suited for studying long-lasting sequences of spatially coherent activity in the absence of changing external stimuli [27, 19], but may not be as well suited to study phenomena on a faster timescale, like the effects of

weak modulatory interactions mediated by the reciprocal, long-range *patchy connections* in primary visual cortex [9].

Generally speaking, one might ask why we need the adaptation to be both slow and weak. For example, in [28], the adaptation was slow but not weak. One could imagine doing a perturbation analysis for a weak stimulus such as in [7] where a weak slowly moving stimulus is applied to a system that has a stable traveling bump. However, strong adaptation, will always induce movement in a bump so that we can never pin the bump with *weak* inputs. Furthermore, by keeping the adaptation $O(1)$, one needs to compute the adjoint solution to a two-variable traveling bump, a difficult task in one spatial dimension, and impossible (as far as we can tell) in two spatial dimensions. Thus, by working with weak inputs and weak/slow adaptation, we have hit a sweet spot from which many of the interesting dynamics emerges.

One type of behavior that has been observed in this class of models that does not occur in our analysis is the so-called breathing solutions [11]. Breathers are periodic solutions to the neural field equations that occur when the bump solution loses stability via a *symmetric* mode. In contrast, sloshers appear when there is a Hopf bifurcation to an *anti-symmetric* mode. In the breather case, the centroid of the bump does not change, so our reduced equations cannot detect such a bifurcation. In contrast, sloshers lead to modulation of the centroid and thus our analysis can capture that. To further explore this, we were able to induce bifurcation to a breathing solution in equations (1,2) but only when ε is sufficiently large. We find that it is possible to continue this bifurcation in ε and make ε quite small, but only if we increase both the strength of adaptation g and the heterogeneity, q such that $\varepsilon q, \varepsilon g$ remain $O(1)$. That is, breathers can only occur when the adaptation and input magnitudes are large compared to the rate of adaptation. Our analysis, therefore, cannot include the appearance of breathers.

The effects of noise on the phase equations is one possible direction for future study. Several cited papers analyze the movement of bump solutions in the presence of noise. Near the drift bifurcation for traveling bump solutions with sufficiently strong linear adaptation, it is possible to derive a stochastic amplitude equation when the adaptation strength and stochastic forcing are similar in magnitude [22]. Sufficiently far from the bifurcation, the stochastic forcing leads to diffusive wandering of the bump solution. Other studies analyze the diffusive behavior of solutions to neural field models and how pinning eliminates diffusive behavior [30]. In [25], the authors compute the effects of adding noise to the normal form of the pitchfork bifurcation. As mentioned previously, these studies assume either a particular firing rate function or kernel. The general case remains unexplored.

A Normal Form for the Hopf Bifurcation on the Ring

Recall that we analyze the bifurcation to sloshing pulses for the general integral equation,

$$\frac{d\theta}{d\tau} = -qJ(\theta) - g \int_0^\infty e^{-s} H(\theta(\tau-s) - \theta(\tau)) ds \quad (34)$$

as g increases. For simplicity, we assume the expansions

$$\begin{aligned} J(\theta) &= \theta + j_3\theta^3 + \dots \\ H(\theta) &= \theta + h_3\theta^3 + \dots, \end{aligned}$$

and $q > 0$. Based on the eigenvalue equation,

$$\lambda^2 + (1 + q - g)\lambda + q = 0$$

we expect a Hopf bifurcation to occur.

To analyze the Hopf bifurcation, we use a multiple time scale expansion. We assume that $\theta(\tau)$ is a function of a “fast” time $\zeta = \tau$ and a “slow” time $\xi = \delta^2\tau$ where δ measures the amplitude of the bifurcating solution. As the nonlinearities are all odd, we can assume that

$$g = g_0 + \delta^2 g_2, \quad \theta = \delta\theta_1(\zeta, \xi) + \delta^3\theta_3(\zeta, \xi)$$

to order δ^3 . We develop a perturbation expansion to obtain the normal form. Before continuing, we need to briefly describe how the integral equation gets expanded in multiple scales. If $f(\zeta, \xi)$ is a function of the fast and slow time-like variable, then, clearly

$$\frac{df}{d\tau} = \frac{\partial f}{\partial \zeta} + \delta^2 \frac{\partial f}{\partial \xi}$$

and

$$\int_0^\infty e^{-s} f(\tau-s) ds = \int_0^\infty e^{-s} f(\zeta-s, \xi-\delta^2 s) ds.$$

We expand this expression to order δ^2 to get:

$$\int_0^\infty e^{-s} f(\tau-s) ds \approx \int_0^\infty e^{-s} f(\zeta-s, \xi) ds - \delta^2 \int_0^\infty s e^{-s} \frac{\partial f(\zeta-s, \xi)}{\partial \xi} ds. \quad (35)$$

Let

$$(Lu)(\zeta) := \frac{\partial u}{\partial \zeta} + qu + g_0 \int_0^\infty e^{-s} [u(\zeta-s) - u(\zeta)] ds.$$

By our choice of g_0 , L has a nullspace $e^{\pm i\omega\zeta}$ and since it is a scalar, so does the adjoint operator under the usual inner product

$$\langle u, v \rangle := \int_0^{2\pi/\omega} \bar{u}(s)v(s) ds.$$

We plug in all the expansions and find to first order that

$$\theta_1 = z(\xi)e^{i\omega\zeta} + c.c$$

where $z(\xi)$ is a complex function of ξ and c.c means complex conjugates. Our goal is to derive equations for z . To cubic order, we obtain:

$$\begin{aligned} (L\theta_3)(\zeta) &= z\xi e^{i\omega\zeta} \left(-1 + \frac{g_0}{1+2i\omega-\omega^2} \right) + c.c \\ &\quad + g_2 z e^{i\omega\zeta} \frac{i\omega}{1+i\omega} + c.c \\ &\quad + -qj_3 \left[ze^{i\omega\zeta} + \bar{z}e^{-i\omega\zeta} \right]^3 \\ &\quad + -gh_3 \int_0^\infty \left[z(\xi)e^{i\omega\zeta}(e^{-i\omega s}-1) + \bar{z}(\xi)e^{-i\omega\zeta}(e^{i\omega s}-1) \right]^3 ds. \end{aligned}$$

The first line comes from applying equation (35). Taking the inner product of this equation with $\exp(i\omega\zeta)$ (essentially, the Fredholm alternative), yields the equation for $z(\xi)$:

$$\alpha \frac{dz}{d\xi} = z[\hat{\gamma}_0 + \hat{\gamma}_3|z|^2] \quad (36)$$

where

$$\begin{aligned} \alpha &= 1 - \frac{g_0}{1+2i\omega-\omega^2} = \frac{2}{1+q}(q + \sqrt{q}i) \\ \hat{\gamma}_0 &= g_2 \frac{i\omega}{1+i\omega} = \frac{g_2}{1+q}(q + \sqrt{q}i) \\ \hat{\gamma}_3 &= \frac{3q}{4q+1} [[q(12h_3 - 4j_3) - j_3] + i18h_3\sqrt{q}]. \end{aligned}$$

B Computation of Functions H_i and J_i

To numerically integrate the phase models on the ring or torus, we require an approximation to the functions H_i , and J_i . These functions depend on and use lookup tables for the steady state bump u_0 (**u0ss**), the derivative of the firing rate evaluated at the steady state bump $f'(u_0)$ (**df_u0b**), and the partial derivatives of the steady state bump, $\partial u_0 / \partial x$, $\partial u_0 / \partial y$ (**ux,uy**). On the toroidal domain, each lookup table has $N \times N$ entries, where for the coefficients below, we choose $N = 64$.

To compute H_i in Equation (9), we use the following procedure

```

H1 = zeros(N,N)
H2 = zeros(N,N)
for i=1:N
    for j=1:N
        temp1 = 0
        temp2 = 0
        for n=1:N
            for m=1:N
                xn = mod(n+i+N/2,N)
                xm = mod(m+j+N/2,N)
                temp1+=ux[n,m]*df_u0b[n,m]*u0ss[xn,xm]
                temp2+=uy[n,m]*df_u0b[n,m]*u0ss[xn,xm]
            end
        end
        H1[i,j] = temp1
        H2[i,j] = temp2
    end
end
H1 *= (2*pi)^2/N^2
H2 *= (2*pi)^2/N^2

```

To compute J_i in Equation (9), we use the following procedure

```

J1 = zeros(N,N)
J2 = zeros(N,N)
for i=1:N
    for j=1:N
        temp1 = 0
        temp2 = 0
        for n=1:N
            for m=1:N
                xn = mod(n+i+N/2,N)
                xm = mod(m+j+N/2,N)
                temp1+=ux[xi,xj]*df_u0b[xn,xm]*I[n,m]
                temp2+=uy[xi,xj]*df_u0b[xn,xm]*I[n,m]
            end
        end
        J1[i,j] = temp1
        J2[i,j] = temp2
    end
end
J1 *= (2*pi)^2/N^2
J2 *= (2*pi)^2/N^2

```

On the torus, taking the difference $J_i - (-H_i)$ results in a negligible

error, revealing that $J_i = -H_i$. Thus, for all phase computations involving J_i , we use the same Fourier approximations for H_i and J_i .

On the ring, the computations are virtually identical with the obvious exception of array shapes.

B.1 Fourier Approximations

After creating the lookup tables $\mathbf{H}_1, \mathbf{H}_2$, we perform a Fourier approximation to make numerical integration easier. The following function and corresponding coefficients and frequencies (Table 1) provide an excellent approximation to the lookup tables $\mathbf{H}_1, \mathbf{H}_2$. A basic error analysis shows that the supremum norm difference between the lookup tables $\mathbf{H}_1, \mathbf{H}_2$ and their Fourier approximations, $\overline{\mathbf{H}}_1, \overline{\mathbf{H}}_2$, is $\|\mathbf{H}_1 - \overline{\mathbf{H}}_1\|_\infty \approx 3.354e-7$.

$$\overline{\mathbf{H}}_1(x, y) = - \sum_{k=1}^{26} \frac{a_k}{N^2} \sin(xn_k + ym_k). \quad (37)$$

The coefficients in Table 1 are computed using Python with Numpy by taking the Fourier transform of the lookup tables $\mathbf{H}_1, \mathbf{H}_2$.

C Numerical Integration

In this section, we detail the various numerical methods used to evaluate the many integro-delay-differential equations of this paper.

C.1 Truncated Neural Field Model on the Torus

The integration of Equation (21) requires the approximation of several double integrals. In the interest of reducing computation time, we use Riemann integrals and a relatively coarse discretization of the spatial domain. For example, for a given time t , the coefficient $p_{10}(t)$ is approximated as

$$p_{10}(t) \approx \sum_{n=1}^N \sum_{m=1}^N \cos(y_m) f(u(x_n, y_m, t)) \frac{(2\pi)^2}{N^2}.$$

Because a linear increase in N leads to a quadratic increase in the total number of operations, we keep $N = 100$, which is an acceptable compromise between speed and accuracy for this problem. All other double sums that appear in p_{ij} , r_{ij} , and s_i are computed this way.

When computing the bifurcation diagram using this system, we use **XPPAUTO** and the numerical options shown in Table 4. The most important options are **Ntst** and **Dsmin**. If **Ntst** is less than 1000, **XPPAUTO** is unreliable in determining the stability of periodic solutions. If **Dsmin** is too large, **XPPAUTO** will skip bifurcation points.

Table 1: Fourier Coefficients of H_1 for $N = 64$. The maximum pointwise difference between this approximation of H_1 and the original H_1 is $3.53733478176e-07$

k	a_k	(n_k, m_k)
0	-0.299041640592	(1,0)
1	-0.0123427222227	(2,0)
2	-2.92404662557e-07	(3,0)
3	2.92404662711e-07	(-3,0)
4	0.0123427222227	(-2,0)
5	0.299041640592	(-1,0)
6	-0.110662059947	(1,1)
7	-0.00255677958311	(2,1)
8	-1.30119169782e-07	(3,1)
9	1.30119169839e-07	(-3,1)
10	0.00255677958311	(-2,1)
11	0.110662059947	(-1,1)
12	-0.00134078962566	(1,2)
13	-8.78193375763e-06	(2,2)
14	-1.40550932909e-07	(3,2)
15	1.40550932908e-07	(-3,2)
16	8.78193375764e-06	(-2,2)
17	0.00134078962566	(-1,2)
18	-0.00134078962566	(1,-2)
19	-8.78193375764e-06	(2,-2)
20	-1.40550932907e-07	(3,-2)
21	1.4055093291e-07	(-3,-2)
22	8.78193375763e-06	(-2,-2)
23	0.00134078962566	(-1,-2)
24	-0.110662059947	(1,-1)
25	-0.00255677958311	(2,-1)
26	-1.30119169783e-07	(3,-1)
27	1.30119169839e-07	(-3,-1)
28	0.00255677958311	(-2,-1)
29	0.110662059947	(-1,-1)

Table 2: Fourier Coefficients of the steady-state coefficients. Plotting $u_{00} + 2u_{10} \cos(x) + 2u_{01} \cos(y) + 4u_{11} \cos(x) \cos(y)$ gives a reasonable approximation to the numerically computed steady-state bump solution.

k	u_k	(n_k, m_k)
0	-2.17382490474	(0, 0)
1	-0.74563470929	(0, 1)
5	-0.74563470929	(1, 0)
6	0.338867473649	(1, 1)
7	0.340507108446	(1, -1)
10	-0.74563470929	(-1, 0)
11	0.340507108446	(-1, 1)
12	0.338867473649	(-1, -1)

Table 3: Fourier Coefficients of the kernel. Plotting $k_{00} + 2k_{10} \cos(x) + 2k_{01} \cos(y) + 4k_{11} \cos(x) \cos(y)$ gives a reasonable approximation to the original periodix kernel.

k	k_k	(n_k, m_k)
0	-0.473945684407	(0, 0)
1	0.19095061386	(0, 1)
4	0.19095061386	(0, -1)
5	0.19095061386	(1, 0)
6	0.108965377668	(1, 1)
7	0.111033925698	(1, -1)
10	0.19095061386	(-1, 0)
11	0.111033925698	(-1, 1)
12	0.108965377668	(-1, -1)

Table 4: XPPAUT0 parameters for the bifurcation diagram Figure 10. XPPAUT0 version 8 has a third column of numerics options, which we left at default values.

AUTO Option	Value
Ntst	1000
Nmax	200
NPr	2
Ds	0.01
Dsmin	0.0001
Ncol	4
EPSL	0.0001
Dsmax	0.1
Par Min	0
Par Max	5
Norm Min	0
Norm Max	1000
EPSU	0.0001
EPSS	0.0001

C.2 Delay Integro-Differential Equations

We implement the right hand side of the integro-differential in Equation (22) as

$$f \begin{pmatrix} t_k \\ \vec{x}_M \\ \vec{y}_M \end{pmatrix} = \left(-g \left(\sum_{n=0}^{M-1} e^{-ndt} H_1[x_{k-n} - x_k, y_{k-n} - y_k] \right) dt + qJ_1(x_k, y_k) \right)$$

$$h \begin{pmatrix} t_k \\ \vec{x}_M \\ \vec{y}_M \end{pmatrix} = \left(-g \left(\sum_{n=0}^{M-1} e^{-ndt} H_2[x_{k-n} - x_k, y_{k-n} - y_k] \right) dt + qJ_2(x_k, y_k) \right),$$

where dt is the time step and

$$\vec{x}_M = \begin{pmatrix} x_k \\ \vdots \\ x_{k-(M-1)} \end{pmatrix}, \quad \vec{y}_M = \begin{pmatrix} y_k \\ \vdots \\ y_{k-(M-1)} \end{pmatrix}$$

are the arrays containing solution values for M previous time steps. The functions H_i and J_i are either the accurate Fourier approximation (Equations (23),(24)), or the truncated Fourier series (Equation (25)). The time step dt is the same as the discretization of the integral.

The algorithm is a straightforward Euler method. For a given time step i ,

```

th1[i+1] = th1[i] + dt*f(t[i],th1[i],...,th1[i-(M-1)],
                           th2[i],...,th2[i-(M-1)])
th2[i+1] = th2[i] + dt*h(t[i],th1[i],...,th1[i-(M-1)],
                           th2[i],...,th2[i-(M-1)])

```

The initial condition for this algorithm requires an array of M time steps. If the parameters are chosen such that a limit cycle exists, then we initialize in an arc:

```

r0 = 1
n0 = linspace(0,-.01,M)
for k = 0:M-1
    th1[k] = r0*cos(n0[k])
    th2[k] = r0*sin(n0[k]).
```

If the parameters are chosen such that a constant-velocity bump exists, then we initialize in a line:

```

x_line = linspace(0,1,M)
y_line = linspace(2,3,M)
for k = 0:M-1
    th1[k] = x[k]
    th2[k] = y[k].
```

When plotting solutions, we disregard at least the first M entries of the solution vector.

Acknowledgments

GBE would like to thank Rodia Curtu, Carina Curto, and Vladimir Itskov for early conversations about this problem.

References

- [1] R. BEN-YISHAI, D. HANSEL, AND H. SOMPOLINSKY, *Traveling waves and the processing of weakly tuned inputs in a cortical network module*, Journal of computational neuroscience, 4 (1997), pp. 57–77.
- [2] P. C. BRESSLOFF AND S. E. FOLIAS, *Front bifurcations in an excitatory neural network*, SIAM Journal on Applied Mathematics, 65 (2004), pp. 131–151, <https://doi.org/10.1137/S0036139903434481>, <http://pubs.siam.org/doi/abs/10.1137/S0036139903434481> (accessed 2016-08-19).

- [3] P. C. BRESSLOFF, S. E. FOLIAS, A. PRAT, AND Y.-X. LI, *Oscillatory waves in inhomogeneous neural media*, Physical Review Letters, 91 (2003), p. 178101, <https://doi.org/10.1103/PhysRevLett.91.178101>, <http://link.aps.org/doi/10.1103/PhysRevLett.91.178101> (accessed 2016-08-19).
- [4] S. COOMBES, *Waves, bumps, and patterns in neural field theories*, Biological cybernetics, 93 (2005), pp. 91–108.
- [5] S. COOMBES AND M. R. OWEN, *Bumps, breathers, and waves in a neural network with wpike frequency adaptation*, Physical Review Letters, 94 (2005), p. 148102, <https://doi.org/10.1103/PhysRevLett.94.148102>, <http://link.aps.org/doi/10.1103/PhysRevLett.94.148102> (accessed 2016-07-29).
- [6] G. B. ERMENTROUT, S. E. FOLIAS, AND Z. P. KILPATRICK, *Spatiotemporal pattern formation in neural fields with linear adaptation*, in Neural Fields, Springer, 2014, pp. 119–151.
- [7] G. B. ERMENTROUT, J. Z. JALICS, AND J. E. RUBIN, *Stimulus-driven traveling solutions in continuum neuronal models with a general smooth firing rate function*, SIAM Journal on Applied Mathematics, 70 (2010), pp. 3039–3064.
- [8] G. FAYE, *Existence and stability of traveling pulses in a neural field equation with synaptic depression*, SIAM Journal on Applied Dynamical Systems, 12 (2013), pp. 2032–2067.
- [9] S. E. FOLIAS, *Nonlinear analysis of breathing pulses in a synaptically coupled neural network*, SIAM Journal on Applied Dynamical Systems, 10 (2011), pp. 744–787.
- [10] S. E. FOLIAS, *Traveling waves and breathers in an excitatory-inhibitory neural field*, Physical Review E, 95 (2017), p. 032210.
- [11] S. E. FOLIAS AND P. C. BRESSLOFF, *Breathing pulses in an excitatory neural network*, SIAM Journal on Applied Dynamical Systems, 3 (2004), pp. 378–407, <https://doi.org/10.1137/030602629>, <http://pubs.siam.org/doi/abs/10.1137/030602629> (accessed 2016-08-19).
- [12] S. E. FOLIAS AND P. C. BRESSLOFF, *Breathers in two-dimensional neural media*, Physical Review Letters, 95 (2005), p. 208107, <https://doi.org/10.1103/PhysRevLett.95.208107>, <http://link.aps.org/doi/10.1103/PhysRevLett.95.208107> (accessed 2016-06-10).

- [13] S. E. FOLIAS AND P. C. BRESSLOFF, *Stimulus-locked traveling waves and breathers in an excitatory neural network*, SIAM Journal on Applied Mathematics, 65 (2005), pp. 2067–2092, <https://doi.org/10.1137/040615171>, <http://pubs.siam.org/doi/abs/10.1137/040615171> (accessed 2016-08-19).
- [14] C. A. FUNG, K. M. WONG, AND S. WU, *A moving bump in a continuous manifold: A comprehensive study of the tracking dynamics of continuous attractor neural networks*, Neural Computation, 22 (2010), pp. 752–792.
- [15] C. C. A. FUNG AND S. I. AMARI, *Spontaneous Motion on Two-Dimensional Continuous Attractors*, Neural Computation, 27 (2015), pp. 507–547, https://doi.org/10.1162/NECO_a_00711.
- [16] C. C. A. FUNG, K. Y. M. WONG, H. MAO, AND S. WU, *Fluctuation-response relation unifies dynamical behaviors in neural fields*, Physical Review E, 92 (2015), p. 022801, <https://doi.org/10.1103/PhysRevE.92.022801>, <http://link.aps.org/doi/10.1103/PhysRevE.92.022801> (accessed 2016-07-29).
- [17] C. C. A. FUNG, K. Y. M. WONG, H. WANG, AND S. WU, *Dynamical synapses enhance neural information processing: gracefulness, accuracy, and mobility*, Neural Computation, 24 (2012), pp. 1147–1185, https://doi.org/10.1162/NECO_a_00269, http://dx.doi.org/10.1162/NECO_a_00269 (accessed 2016-07-29).
- [18] D. HANSEL AND H. SOMPOLINSKY, *13 modeling feature selectivity in local cortical circuits*, (1998).
- [19] V. ITSKOV, C. CURTO, E. PASTALKOVA, AND G. BUZSÁKI, *Cell assembly sequences arising from spike threshold adaptation keep track of time in the hippocampus*, The Journal of Neuroscience, 31 (2011), pp. 2828–2834.
- [20] D. JOHNSTON AND S. M.-S. WU, *Foundations of cellular neurophysiology*, MIT press, 1994.
- [21] J. P. KEENER, *Principles of applied mathematics*, Addison-Wesley, 1988.
- [22] Z. KILPATRICK AND G. FAYE, *Pulse Bifurcations in Stochastic Neural Fields*, SIAM Journal on Applied Dynamical Systems, 13 (2014), pp. 830–860, <https://doi.org/10.1137/140951369>, <http://pubs.siam.org/doi/abs/10.1137/140951369> (accessed 2017-10-03).

- [23] Z. P. KILPATRICK AND P. C. BRESSLOFF, *Spatially structured oscillations in a two-dimensional excitatory neuronal network with synaptic depression*, Journal of Computational Neuroscience, 28 (2009), pp. 193–209, <https://doi.org/10.1007/s10827-009-0199-6>, <http://link.springer.com/article/10.1007/s10827-009-0199-6> (accessed 2016-08-19).
- [24] Z. P. KILPATRICK AND P. C. BRESSLOFF, *Effects of synaptic depression and adaptation on spatiotemporal dynamics of an excitatory neuronal network*, Physica D: Nonlinear Phenomena, 239 (2010), pp. 547–560, <https://doi.org/10.1016/j.physd.2009.06.003>, <http://www.sciencedirect.com/science/article/pii/S0167278909001833> (accessed 2016-10-25).
- [25] C. R. LAING AND A. LONGTIN, *Noise-induced stabilization of bumps in systems with long-range spatial coupling*, Physica D: Nonlinear Phenomena, 160 (2001), pp. 149–172, [https://doi.org/10.1016/S0167-2789\(01\)00351-7](https://doi.org/10.1016/S0167-2789(01)00351-7), <http://www.sciencedirect.com/science/article/pii/S0167278901003517> (accessed 2017-10-02).
- [26] J. NOWACKI, *XPPy*, 2011, <http://seis.bris.ac.uk/~enxjn/xppy/>.
- [27] E. PASTALKOVA, V. ITSKOV, A. AMARASINGHAM, AND G. BUZSÁKI, *Internally generated cell assembly sequences in the rat hippocampus*, Science, 321 (2008), pp. 1322–1327.
- [28] D. PINTO AND G. B. ERMENTROUT, *Spatially structured activity in synaptically coupled neuronal networks: I. Traveling fronts and pulses*, SIAM Journal on Applied Mathematics, 62 (2001), pp. 206–225, <https://doi.org/10.1137/S0036139900346453>, <http://pubs.siam.org/doi/abs/10.1137/S0036139900346453> (accessed 2016-08-19).
- [29] A. C. PIPKIN, *A course on integral equations*, no. 9, Springer Science & Business Media, 1991.
- [30] D. POLL AND Z. P. KILPATRICK, *Stochastic motion of bumps in planar neural fields*, SIAM Journal on Applied Mathematics, 75 (2015), pp. 1553–1577, <https://doi.org/10.1137/140999505>, <http://pubs.siam.org/doi/abs/10.1137/140999505> (accessed 2016-08-19).
- [31] L. C. YORK AND M. C. W. v. ROSSUM, *Recurrent networks with short term synaptic depression*, Journal of Computational Neuroscience, 27 (2009), p. 607, <https://doi.org/10.1007/s10827-009-0172-4>, <http://link.springer.com/article/10.1007/s10827-009-0172-4> (accessed 2016-07-29).

- [32] W. ZHANG AND S. WU, *Neural information processing with feedback modulations*, Neural Computation, 24 (2012), pp. 1695–1721, https://doi.org/10.1162/NECO_a_00296, http://www.mitpressjournals.org/doi/full/10.1162/NECO_a_00296 (accessed 2016-07-29).

A multiple timescales approach to bridging spiking- and population-level dynamics

Youngmin Park* & G. Bard Ermentrout

Department of Mathematics
University of Pittsburgh
Pittsburgh PA 15260

August 15, 2018

Abstract

A rigorous bridge between spiking-level and macroscopic quantities is an on-going and well-developed story for asynchronously firing neurons, but focus has shifted to include neural populations exhibiting varying synchronous dynamics. Recent literature has used the Ott–Antonsen ansatz (2008) to great effect, allowing a rigorous derivation of an order parameter for large oscillator populations. The ansatz has been successfully applied using several models including networks of Kuramoto oscillators, theta models, and integrate-and-fire neurons, along with many types of network topologies. In the present study, we take a converse approach: given the mean field dynamics of slow synapses, predict the synchronization properties of finite neural populations. The slow synapse assumption is amenable to averaging theory and the method of multiple timescales. Our proposed theory applies to two heterogeneous populations of N excitatory n -dimensional and N inhibitory m -dimensional oscillators with homogeneous synaptic weights. We then demonstrate our theory using two examples. In the first example we take a network of excitatory and inhibitory theta neurons and consider the case with and without heterogeneous inputs. In the second example we use Traub models with calcium for the excitatory neurons and Wang-Buzsáki models for the inhibitory neurons. We accurately predict phase drift and phase locking in each example even when the slow synapses exhibit non-trivial mean-field dynamics.

Keywords Multiple timescales, Synchrony, Mean field

*Corresponding author. Email yop6@pitt.edu

1 Lead Paragraph

Mean field theory is one of the primary tools used by physicists and mathematicians working in neuroscience. For nearly five decades, the phenomenological derivation of neural field equations that describe population-level quantities such as the mean firing rate was sufficient, in part due to its success in reproducing the diverse spatio-temporal neural activity patterns of the neocortex. However, within the past two decades, theoretical studies have re-examined the derivation of the mean field models by starting at the microscopic, single-neuron spiking level. The spiking-level approach splits in two at the very beginning. In the first approach, the degree of synchrony of the population does not matter, and spiking neurons are assumed to be entirely asynchronous. This case is most similar to the classic mean field description. In the second approach, the degree of synchrony in the population does matter, and correlations between neurons are taken into account. The present study is most akin to the second approach, and extends upon existing results by introducing methods to reduce arbitrarily complex spiking models into a set of phase values that can be used to predict population synchrony.

2 Introduction

Neural mean field models are a useful framework for studying mesoscopic and macroscopic spatio-temporal activity in the cortex. Examples include mammalian path integration, head direction tracking, visual hallucination, working memory, spatial object location, and object orientation [6, 5, 12, 3].

Existing studies derive macroscopic quantities starting at the spiking level, but require particular assumptions including asynchronous firing [19, 18, 26] and Poisson statistics [2, 1]. These studies contain no information about synchronization at the spiking level, which could underpin the loss or gain of power in electroencephalogram (EEG) frequency bands [7].

Recent studies relax the asynchronous firing assumption with the goal of predicting population synchrony, and have successfully used low-dimensional spiking models like the Kuramoto model [29], theta model [11, 7], Alder units [27], and quadratic integrate-and-fire models [21] to this end. These models are amenable to the Ott-Antonsen ansatz [24], which results in a complementary order parameter in addition to the mean field variables, e.g., firing rate.

In contrast to these studies, the goal of the present study is to derive a metric of synchrony at the spiking level for general oscillators. In particular, we derive a set of phase equations for each oscillator as a function of the mean field. Moreover, the existence of multiple timescales allows our approach to be converse to existing studies, where we derive the phase equations starting

with the the mean field dynamics, which for the present study are the same as the mean synaptic variables.

We begin with a finite network of N , n -dimensional excitatory spiking neurons and N , m -dimensional inhibitory spiking neurons connected by slow synapses (The slow synaptic assumption is one of several that allows us to apply the theory of averaging and exploit the difference in time scales to get exact mean field equations for *finite* networks of neurons [4, 10, 11]. While, generally, synapses are fast, there are certain classes of excitatory and inhibitory synapses that are slow (notably, NMDA and GABA_B [8], and experimentally observed but unidentified synapses [15]):

$$\frac{d\mathbf{x}_i}{dt} = \mathbf{F}^x(\mathbf{x}_i, s^x, s^y) + \varepsilon \mathbf{G}_i^x(\mathbf{x}_i), \quad (1)$$

$$\frac{d\mathbf{y}_i}{dt} = \mathbf{F}^y(\mathbf{y}_i, s^x, s^y) + \varepsilon \mathbf{G}_i^y(\mathbf{y}_i), \quad (2)$$

$$\mu^x \frac{ds^x}{dt} = \varepsilon \left[-s^x + \frac{1}{N} \sum_{i=1}^N \sum_j \delta(t - t_{i,j}^x) \right], \quad (3)$$

$$\mu^y \frac{ds^y}{dt} = \varepsilon \left[-s^y + \frac{1}{N} \sum_{i=1}^N \sum_j \delta(t - t_{i,j}^y) \right], \quad (4)$$

where $i = 1 \dots, N$, $t_{i,j}^x$ ($t_{i,j}^y$) is the time of the j^{th} spike of neuron i in population \mathbf{x} (\mathbf{y}). The function \mathbf{F}^k is the vector field for neuron $k = x, y$, and the function \mathbf{G}_i^k represents heterogeneity in oscillator i of vector field k . The parameters μ_x/ε , and μ_y/ε represent the time constants of the \mathbf{x} and \mathbf{y} populations. We allow the $O(1)$ parameters μ_x, μ_y to be different so that we can flexible vary the excitatory and inhibitory synaptic time scales.. For conductance-based models, we take the spike time be the up-wards zero-crossing of the membrane potential. The same notation holds for the inhibitory population \mathbf{y} . As we show next, our derivation only requires knowledge about whether or not any neuron spikes in a given population, thus we need not be precise about indexing the spike times by neuron number.

Equations (3) and (4) represent the slow synaptic dynamics. The synaptic variable s^x (s^y) resets instantaneously (with small magnitude) as $s^x \mapsto \bar{s}^x + \varepsilon/(N\mu^x)$ ($s^y \mapsto \bar{s}^y + \varepsilon/(N\mu^y)$) whenever \mathbf{x}_i (\mathbf{y}_i) spikes. The small ε assumption results in slow timescale decay of the synaptic variables s^x, s^y . Essentially, s^x, s^y are low-pass filtered versions of the firing rates of the x, y populations. With these notations defined, we turn to the assumptions.

- The term ε is small, $0 < \varepsilon \ll 1$. Thus the synapses increment instantaneously with order ε , but decay slowly between spikes.
- There is a separation of timescales into a “fast” time t and a “slow” time $\tau = \varepsilon t$.

- The mean synaptic values, \bar{s}^x and \bar{s}^y , are constant on the fast timescale and differ at most by a small amount $O(\varepsilon)$. These mean synapses represent the mean field values of Equations (1)–(4). They must be close in value since they are the mean firing rates (frequencies) of the populations x, y and in order for non-trivial phase-locking to occur between populations, their mean frequencies must be close.
- In the decoupled case without heterogeneity ($\varepsilon = 0$), we assume that there exists a T -periodic limit cycle $\Phi^k(t, \tau)$ satisfying Equations (1),(2) for a range of values $\bar{s}^k \in [s^-, s^+]$ where $k = x, y$.
- Generally, $\bar{s}^k > 0$, and there might not exist a limit cycle when $\bar{s}^k = 0$.
- The vector field dimensions are arbitrary: $\mathbf{F}^x, \mathbf{G}_i^x : \mathbb{R}^n \times \mathbb{R} \times \mathbb{R} \rightarrow \mathbb{R}^n$ and $\mathbf{F}^y, \mathbf{G}_i^y : \mathbb{R}^m \times \mathbb{R} \times \mathbb{R} \rightarrow \mathbb{R}^m$, where $n, m \geq 1$.

These assumptions appear in a similar form in Rubin et al. 2013 [28]. The authors show that when the mean synaptic values are constant with slow synaptic decay, the slow and strong coupling problem becomes a fast and weak coupling problem, and thus amenable to the classic phase reduction. However, we are also interested in the case where the synaptic variables s^x, s^y are slowly varying. Thus, we allow that

- There can exist small amplitude (order σ , small) slow oscillations in the mean slow variables \bar{s}^x, \bar{s}^y for some parameter values μ^x, μ^y satisfying the mean field description of Equations (1)–(4)

$$\begin{aligned} \mu^x \frac{d\bar{s}^x}{dt} &= \varepsilon[-\bar{s}^x + \omega^x(\bar{s}^x, \bar{s}^y)], \\ \mu^y \frac{d\bar{s}^y}{dt} &= \varepsilon[-\bar{s}^y + \omega^y(\bar{s}^x, \bar{s}^y)], \end{aligned} \quad (5)$$

where ω^k is the frequency of population $k = x, y$.

The goal of this paper is to derive a system of equations describing the phase locking properties of the network (Equations (1)–(4)). The equations will complement Equation (5), which is the mean field formulation of Equations (1)–(4). The primary contribution of the paper is to show that the phase reduction is valid when the synapses are slowly varying with small amplitude.

Before we start, we briefly summarize the derivation to follow. The first step of our analysis is a perturbation of order ε off of the uncoupled solution (Equations (1)–(4) with $\varepsilon = 0$). The order ε terms of the expansion capture the weak and slow interactions of Equations (1)–(4). In particular, we include slow timescale phase shifts $\theta_i^x(\tau)$ and $\theta_i^y(\tau)$, and explicitly write each synaptic variable as its fixed mean value plus possible non-stationary terms. The goal of the derivation below is to determine the dynamics of

the variables $\theta_i^x(\tau)$ and $\theta_i^y(\tau)$ by exploiting the separation in timescales. We find as expected that the phase dynamics exhibit all-to-all coupling, but less intuitively that small deviations of the mean synaptic values \bar{s}^x, \bar{s}^y away from the fixed point (s^*, s^*) contribute to large phase drifts. With this summary in mind, we turn to the detailed derivation.

3 Derivation of the Phase Model

We begin the reduction to phase oscillators with the ansatz

$$\begin{aligned}\mathbf{x}_i(t, \tau) &= \mathbf{x}_i(t + \theta_i^x(\tau), s^*) = \Phi^x(t + \theta_i^x(\tau), s^*) + \varepsilon \xi_i^x(t + \theta_i^x(\tau), s^*) + O(\varepsilon^2), \\ \mathbf{y}_i(t, \tau) &= \mathbf{y}_i(t + \theta_i^y(\tau), s^*) = \Phi^y(t + \theta_i^y(\tau), s^*) + \varepsilon \xi_i^y(t + \theta_i^y(\tau), s^*) + O(\varepsilon^2), \\ s^x(t, \tau) &= \bar{s}^x(\tau) + \frac{\varepsilon}{N\mu^x} \sum_i f(t + \theta_i^x(\tau)) + O(\varepsilon^2), \\ s^y(t, \tau) &= \bar{s}^y(\tau) + \frac{\varepsilon}{N\mu^y} \sum_i f(t + \theta_i^y(\tau)) + O(\varepsilon^2),\end{aligned}\tag{6}$$

where $\bar{s}^k(\tau)$ is the slowly varying mean synaptic value for $k = x, y$, f represents the effects of fast timescale, small-magnitude spikes on the synaptic variable, and $\theta_i^x(\tau), \theta_i^y(\tau)$ are the slow timescale phase shifts due to the slow synaptic interactions. Technically, the solutions, $\mathbf{x}_i, \mathbf{y}_i$, uncoupled solutions, Φ^k , and first order expansion term ξ_i^x have inputs of the form $(t + \theta_i(\tau), \bar{s}^x(\tau), \bar{s}^y(\tau))$, but because we evaluate these functions at the fixed mean value s^* , we abbreviate the notation of the redundant inputs by writing $(t + \theta_i(\tau), s^*)$.

Using the periodicity of $s^k(t, \tau)$ on the fast timescale and small delta function impulses of order ε , one can derive f explicitly as

$$f(t + \theta^k(\tau)) = \left[\left(1 - (t + \theta^k(\tau))/T \pmod{1} \right) - 1/2 \right].$$

We detail the calculations in Appendix B. For notational convenience, we do not write f explicitly for the remainder of the derivation.

Next, because the slow oscillations are small amplitude (order σ), we include an additional term in the expansion:

$$\begin{aligned}s^k(t, \tau) &= \bar{s}^k(\tau) + s^* - s^* + \frac{\varepsilon}{N\mu^k} \sum_j f(t + \theta_j^k(\tau)) \\ &= s^* + \sigma \left(\frac{\bar{s}^k(\tau) - s^*}{\sigma} \right) + \frac{\varepsilon}{N\mu^k} \sum_j f(t + \theta_j^k(\tau)),\end{aligned}$$

where s^* is the constant fixed mean values $\bar{s}^x = \bar{s}^y$. Plugging in Equation (6) into Equation (1) and grouping in terms of small order (ε and σ) results

in the system of equations,

$$\begin{aligned}
\frac{\partial \Phi^x}{\partial t} &= \mathbf{F}^x[\Phi^x(t + \theta_i^x(\tau)), s^*], \\
\frac{d\theta_i^x}{d\tau} \frac{\partial \Phi^x}{\partial t}(t + \theta_i^x(\tau), s^*) &+ \frac{d}{dt} \xi_i^x(t + \theta_i^x(\tau), s^*) \\
&= \mathbf{F}_{\Phi^x}^x(\Phi^x(t + \theta_i^x(\tau)), s^*) \xi_i^x(t + \theta_i^x(\tau), s^*) \\
&\quad + \mathbf{F}_{s^x}^x(\Phi^x(t + \theta_i^x(\tau)), s^*) \left(\frac{\sigma \bar{s}^x(\tau) - s^*}{\varepsilon} + \frac{1}{N\mu^x} \sum_j f(t + \theta_j^x(\tau)) \right) \\
&\quad + \mathbf{F}_{s^y}^x(\Phi^x(t + \theta_i^x(\tau)), s^*) \left(\frac{\sigma \bar{s}^y(\tau) - s^*}{\varepsilon} + \frac{1}{N\mu^y} \sum_j f(t + \theta_j^y(\tau)) \right) \\
&\quad + \mathbf{G}_i^x(\Phi^x(t + \theta_i^x(\tau))).
\end{aligned}$$

For an n -dimensional (m -dimensional) vector field \mathbf{F}^x (\mathbf{F}^y), the derivative $\mathbf{F}_{\Phi^x}^x$ ($\mathbf{F}_{\Phi^y}^y$) represents the Jacobian matrix. Rewriting yields,

$$\begin{aligned}
L\xi_i^x(t + \theta_i^x(\tau)) &= \frac{d\theta_i^x}{d\tau} \frac{d\Phi^x}{dt}(t + \theta_i^x(\tau), s^*) \\
&\quad - \mathbf{F}_{s^x}^x(\Phi^x(t + \theta_i^x(\tau)), s^*) \left([\bar{s}^x(\tau) - s^*]/\varepsilon + \frac{1}{N\mu^x} \sum_j f(t + \theta_j^x(\tau)) \right) \\
&\quad - \mathbf{F}_{s^y}^x(\Phi^x(t + \theta_i^x(\tau)), s^*) \left([\bar{s}^y(\tau) - s^*]/\varepsilon + \frac{1}{N\mu^y} \sum_j f(t + \theta_j^y(\tau)) \right) \\
&\quad - \mathbf{G}_i^x(\Phi^x(t + \theta_i^x(\tau))),
\end{aligned} \tag{7}$$

where

$$Lu \equiv -\frac{du}{dt} + \mathbf{F}_{\Phi^x}^x(\Phi^x(t + \theta_i^x(\tau)), s^*)u.$$

Note that we have already collected terms in order ε , so we have no need to keep the σ/σ term and neglect it from now on. It is straightforward to show that the adjoint of L is

$$L^*v = v' + [\mathbf{F}_{\Phi^x}^x(\Phi^x(t + \theta_i^x(\tau)), s^*)]^T v.$$

We find that a function \mathbf{z}^x in the nullspace of this adjoint operator satisfies

$$\frac{d\mathbf{z}^x}{dt}(t + \theta_i^x(\tau)) = -[\mathbf{F}_{\Phi^x}^x(\Phi^x(t + \theta_i^x(\tau)), s^*)]^T \mathbf{z}^x(t + \theta_i^x(\tau)),$$

and

$$\mathbf{z}^x \cdot \frac{d\Phi^x}{dt} = 1.$$

The function \mathbf{z}^x is the same as the infinitesimal phase response curve of the oscillator Φ^x [10].

Next, we require the existence of a bounded periodic function ξ_i^x satisfying Equation (7). Because the operator L has a closed range defined on the space of real-valued T -periodic functions, it follows that there exists a function u satisfying $Lu = b$ if and only if $\langle u, v \rangle = 0$ for all v in the nullspace of L^* [14], where

$$\langle u, v \rangle = \int_0^T u \cdot v \, dt.$$

Applying the existence condition directly to the right hand side of Equation (7) yields (with a bit of rearrangement)

$$\begin{aligned} & \int_0^T \frac{d\theta_i^x}{d\tau} \frac{d\Phi^x}{dt}(t, s^*) \cdot \mathbf{z}^x(t, s^*) \, dt \\ &= \int_0^T \mathbf{F}_{s^x}^x(\Phi^x(t), s^*) \cdot \mathbf{z}^x(t, s^*) \left(\frac{\bar{s}^x(\tau) - s^*}{\varepsilon} + \frac{1}{N\mu^x} \sum_j f(t + \theta_j^x - \theta_i^x) \right) \, dt \\ &+ \int_0^T \mathbf{F}_{s^y}^x(\Phi^x(t), s^*) \cdot \mathbf{z}^x(t, s^*) \left(\frac{\bar{s}^y(\tau) - s^*}{\varepsilon} + \frac{1}{N\mu^x} \sum_j f(t + \theta_j^y - \theta_i^x) \right) \, dt \\ &+ \int_0^T \mathbf{G}_i^x(\Phi^x(t), s^*) \cdot \mathbf{z}^x(t, s^*) \, dt. \end{aligned}$$

Simplifying and rewriting, we arrive at the phase equations:

$$\begin{aligned} \frac{d\theta_i^x}{d\tau} &= [\bar{s}^x(\tau) - s^*]\beta^{xx}/\varepsilon + [\bar{s}^y(\tau) - s^*]\beta^{xy}/\varepsilon + B_i^x \\ &+ \frac{1}{N\mu^x} \sum_{j=1}^N H^{xx}(\theta_j^x(\tau) - \theta_i^x(\tau)) + \frac{1}{N\mu^x} \sum_{j=1}^N H^{xy}(\theta_j^y(\tau) - \theta_i^x(\tau)), \end{aligned} \quad (8)$$

where

$$\begin{aligned} \beta^{xy} &= \frac{1}{T} \int_0^T \mathbf{F}_{s^y}^x(\Phi^x(t), s^*) \cdot \mathbf{z}^x(t, s^*) \, dt, \\ \beta^{xx} &= \frac{1}{T} \int_0^T \mathbf{F}_{s^x}^x(\Phi^x(t), s^*) \cdot \mathbf{z}^x(t, s^*) \, dt, \\ H^{xx}(\phi) &= \frac{1}{T} \int_0^T \mathbf{F}_{s^x}^x(\Phi^x(t), s^*) \cdot \mathbf{z}^x(t, s^*) f(t + \phi) \, dt, \\ H^{xy}(\phi) &= \frac{1}{T} \int_0^T \mathbf{F}_{s^y}^x(\Phi^x(t), s^*) \cdot \mathbf{z}^x(t, s^*) f(t + \phi) \, dt, \\ B_i^x &= \frac{1}{T} \int_0^T \mathbf{G}_i^x(\Phi^x(t), s^*) \cdot \mathbf{z}^x(t, s^*) \, dt. \end{aligned}$$

The vigilant reader may notice a possible issue with the term $(\bar{s}^x(\tau) - s^*)/\varepsilon$, where ε is small. We require that the deviations of $\bar{s}^x(\tau)$ from s^* to be small, in particular to be of order σ . In our derivation, the order σ term cancels so that we can treat the difference $(\bar{s}^x(\tau) - s^*)$ as order ε . Thus, the term $(\bar{s}^x(\tau) - s^*)/\varepsilon$ is order $O(1)$.

Using the same arguments, we arrive at the phase equations for the y population,

$$\begin{aligned} \frac{d\theta_i^y}{d\tau} &= [\bar{s}^x(\tau) - s^*]\beta^{yx}/\varepsilon + [\bar{s}^y(\tau) - s^*]\beta^{yy}/\varepsilon + B_i^y \\ &+ \frac{1}{N\mu^y} \sum_{j=1}^N H^{yx}(\theta_j^x(\tau) - \theta_i^y(\tau)) + \frac{1}{N\mu^y} \sum_{j=1}^N H^{yy}(\theta_j^y(\tau) - \theta_i^y(\tau)), \end{aligned} \quad (9)$$

where

$$\begin{aligned} \beta^{yx} &= \frac{1}{T} \int_0^T \mathbf{F}_{s^x}^y(\Phi^y(t), s^*) \cdot \mathbf{z}^y(t, s^*) dt, \\ \beta^{yy} &= \frac{1}{T} \int_0^T \mathbf{F}_{s^y}^y(\Phi^y(t), s^*) \cdot \mathbf{z}^y(t, s^*) dt, \\ H^{yx}(\phi) &= \frac{1}{T} \int_0^T \mathbf{F}_{s^x}^y(\Phi^y(t), s^*) \cdot \mathbf{z}^y(t, s^*) f(t + \phi) dt, \\ H^{yy}(\phi) &= \frac{1}{T} \int_0^T \mathbf{F}_{s^y}^y(\Phi^y(t), s^*) \cdot \mathbf{z}^y(t, s^*) f(t + \phi) dt, \\ B_i^y &= \frac{1}{T} \int_0^T \mathbf{G}_i^y(\Phi^y(t), s^*) \cdot \mathbf{z}^y(t, s^*) dt. \end{aligned}$$

Note that in the phase equations (8) and (9), the synaptic variables are exogenous and do not depend on the microscopic solutions – only the microscopic solutions depend on the mean field. Thus, the microscopic dynamics are fully described by properties of the individual oscillators (the iPRC \mathbf{z}^k , the vector field \mathbf{F}^k), and the mean synaptic variables \bar{s}^k .

When analyzing solutions, we use the phase differences $\phi_i^x = \theta_i^x - \theta_1^x$, $\phi_i^y = \theta_i^y - \theta_1^y$, where $i = 1, \dots, N$, and $\phi^z = \theta_1^y - \theta_1^x$. By definition, $\phi_1^x = \phi_1^y = 0$ and $d\phi_1^x/d\tau = d\phi_1^y/d\tau = 0$, so we only plot phase differences for $j > 1$. As we have shown in our derivation, our theory tolerates order ε heterogeneities in the vector fields. The phase difference dynamics are then

$$\begin{aligned} N\mu^x \frac{d\phi_i^x}{d\tau} &= \sum_{j=1}^N [H^{xx}(\phi_j^x - \phi_i^x) - H^{xx}(\phi_j^x)] + B_i^x - B_1^x \\ &+ \sum_{j=1}^N [H^{xy}(\phi_j^y - \phi_i^x + \phi^z) - H^{xy}(\phi_j^y + \phi^z)], \end{aligned} \quad (10)$$

$$N\mu^y \frac{d\phi_i^y}{d\tau} = \sum_{j=1}^N \left[H^{yy} (\phi_j^y - \phi_i^y) - H^{yy} (\phi_j^y) \right] + B_i^y - B_1^y \\ + \sum_{j=1}^N \left[H^{yx} (\phi_j^x - \phi_i^y - \phi^z) - H^{yx} (\phi_j^x - \phi^z) \right], \quad (11)$$

$$\frac{d\phi^z}{d\tau} = [\bar{s}^x(\tau) - s^*](\beta^{yx} - \beta^{xx})/\varepsilon + [\bar{s}^y(\tau) - s^*](\beta^{yy} - \beta^{xy})/\varepsilon \\ + \frac{1}{N\mu^y} \sum_{j=1}^N \left[H^{yx} (\phi_j^x - \phi^z) + H^{yy} (\phi_j^y) \right] \\ - \frac{1}{N\mu^x} \sum_{j=1}^N \left[H^{xx} (\phi_j^x) + H^{xy} (\phi_j^y + \phi^z) \right] \\ + B_1^y - B_1^x \quad (12)$$

where $i = 1, \dots, N$. When the mean synaptic variables are slowly varying, the terms $\bar{s}^k(\tau) - s^*$ in the right hand side of $d\phi^z/d\tau$ are what contribute to large phase drifts between the populations.

To aid in the numerics and analysis, we make note of some facts, starting with the relationship between constant mean synapses and frequency.

3.1 Relationship Between Constant Mean Synapses and Frequency

Suppose that the mean \bar{s}^k is constant and $\bar{s}^k = s^*$. Recall that for the synaptic variable s^k following a spike,

$$s^k(t) = s^k(0)e^{-\varepsilon t/\mu^k}, t < T^-,$$

where T^- is the period of the fast oscillator up to and not including the spike. We may determine the initial condition by solving

$$s^k(T^+) = s^k(0)e^{-\varepsilon T/\mu^k} + \varepsilon/\mu^k = s^k(0),$$

which yields

$$s^k(0) = \frac{\varepsilon}{\mu^k} \frac{1}{1 - e^{-\varepsilon T/\mu^k}}.$$

Taking the mean value of $s^k(t)$ over one period,

$$\bar{s}^k = \frac{1}{T} \int_0^T s^k(t) dt,$$

we find that

$$\bar{s}^k = \frac{1}{T}. \quad (13)$$

That is, $s^* = \bar{s}^k$ is the same as the fast frequency.

3.2 Fourier Approximation

Because the domain of each function H^{jk} is periodic, we can use a Fourier series approximation to make the numerics tractable. We extract the Fourier coefficients using the fast Fourier transform (FFT) and construct an approximation by writing

$$H^{jk}(x) = \sum_{n=0}^M (a_n \cos(nx/T) + b_n \sin(nx/T)).$$

All right hand sides can be written as a sum of sines and cosines, thus amenable to a bifurcation analysis using **XPPAUT0**. Constructing the Jacobian matrix using derivatives of H^{jk} is also straightforward, since we only need to take the derivative of sines and cosines:

$$\frac{dH^{jk}}{dx}(x) = \sum_{n=0}^M [-na_n \cos(nx/T)/T + nb_n \sin(nx/T)/T].$$

See Tables 3, 4 for the values of the Fourier coefficients.

4 Results

We now turn to the simulation of neural models to test our theory. We begin by considering a population of excitatory and inhibitory theta neurons [11] and look at two cases: first when the mean synaptic values are fixed, and second when the mean synaptic values are slowly varying with small amplitude about a fixed point. In the first case we show the existence and stability of various phase locked solutions. In the second case we use numerics to demonstrate the accuracy of our phase model.

We conclude by repeating the same comparison using biophysically realistic models. The models we consider are excitatory Traub models with calcium [30], and inhibitory Wang-Buzsáki models [31].

4.1 Theta Neurons

Consider a network of excitatory and inhibitory theta neurons with all-to-all coupling,

$$\begin{aligned}\frac{dx_j}{dt} &= \pi(1 - \cos(x_j) + (1 + \cos(x_j))[a^x + b^x s^x - c^x s^y]), \\ \frac{dy_j}{dt} &= \pi(1 - \cos(y_j) + (1 + \cos(y_j))[a^y + b^y s^x - c^y s^y]), \\ \mu^x \frac{ds^x}{dt} &= \varepsilon \left[-s^x + \frac{1}{N} \sum_j \delta(x_j - \pi) \right], \\ \mu^y \frac{ds^y}{dt} &= \varepsilon \left[-s^y + \frac{1}{N} \sum_j \delta(y_j - \pi) \right],\end{aligned}\tag{14}$$

where $a^{x,y}$, $b^{x,y}$, and $c^{x,y}$ are positive constants chosen such that the main assumptions of this paper are satisfied. In this system, the dynamics of both populations are virtually identical, but the distinguishing features are the parameters b^x, b^y and c^x, c^y . Whenever a neuron in population \mathbf{x} (\mathbf{y}) spikes, it will positively (negatively) contribute to the dynamics of both populations, due to the $b^x, b^y > 0$ ($-c^x, -c^y < 0$) terms. Given values \bar{s}^x and \bar{s}^y , the period of the oscillators is given by the solution to the integral

$$T^k = \frac{1}{\pi} \int_{-\pi}^{\pi} \frac{dx}{1 - \cos(x) + (1 + \cos(x))I^k}, \quad k = x, y,$$

where $I^k = a^k + b^k \bar{s}^x - c^k \bar{s}^y$. The reciprocal of the solution is the frequency,

$$f^k(\bar{s}^x, \bar{s}^y) = \sqrt{[I^k]_+},$$

where $[x]_+ = \max\{0, x\}$. Thus, the averaged dynamics are

$$\mu^x \frac{ds^x}{dt} = \varepsilon \left(-s^x + \sqrt{[I^x]_+} \right), \tag{15}$$

$$\mu^y \frac{ds^y}{dt} = \varepsilon \left(-s^y + \sqrt{[I^y]_+} \right). \tag{16}$$

For this system, the limit cycle and iPRC are, respectively,

$$\Phi^i(t, s^*) \equiv \Phi(t, s^*) = 2 \arctan(s^* \tan(s^* \pi(t + T/2))),$$

$$Z^i(t, s^*) \equiv Z(t, s^*) = [\cos^2(s^* \pi(t + T/2)) + (s^*)^2 \sin^2(s^* \pi(t + T/2))] / (2(s^*)^2 \pi),$$

where s^* is the fixed point $\bar{s}^x = \bar{s}^y$. To compute the H functions, we note that

$$\begin{aligned}\mathbf{F}_{sx}^x(\Phi(t, s^*), s^*) &= b^x \pi [1 + \cos(\Phi(t, s^*))], \\ \mathbf{F}_{sy}^x(\Phi(t, s^*), s^*) &= -c^x \pi [1 + \cos(\Phi(t, s^*))], \\ \mathbf{F}_{sx}^y(\Phi(t, s^*), s^*) &= b^y \pi [1 + \cos(\Phi(t, s^*))], \\ \mathbf{F}_{sy}^y(\Phi(t, s^*), s^*) &= -c^y \pi [1 + \cos(\Phi(t, s^*))].\end{aligned}$$

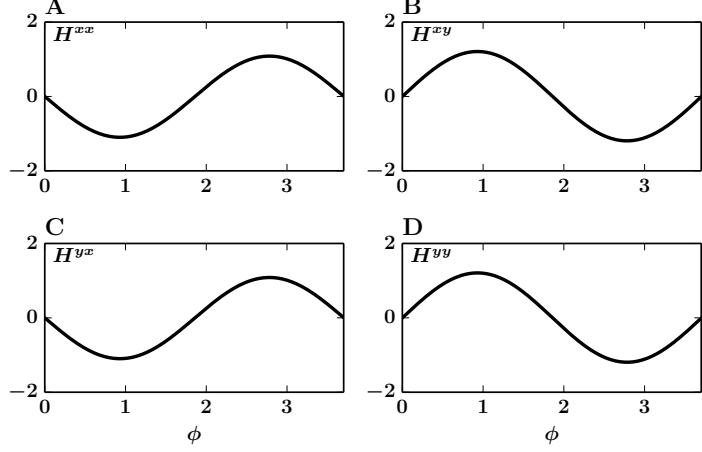


Figure 1: Example H -functions of the theta model. Panel A: H^{xx} . Panel B: H^{xy} . Panel C: H^{yx} . Panel D: H^{yy} . In all panels, parameter values are $a^x = a^y = 0.1$, $b^x = b^y = 1$, $c^x = c^y = 1.1$, and $\mu^x = \mu^y = 1$.

Thus the H functions of Equations (8) and (9) for this system are given by

$$\begin{aligned}
H^{xx}(\phi) &= \frac{b^x \pi}{T \mu^x} \int_0^T Z(t, s^*) [1 + \cos(\Phi(t, s^*))] f(t + \phi) dt, \\
H^{xy}(\phi) &= -\frac{c^x \pi}{T \mu^y} \int_0^T Z(t, s^*) [1 + \cos(\Phi(t, s^*))] f(t + \phi) dt, \\
H^{yx}(\phi) &= \frac{b^y \pi}{T \mu^x} \int_0^T Z(t, s^*) [1 + \cos(\Phi(t, s^*))] f(t + \phi) dt, \\
H^{yy}(\phi) &= -\frac{c^y \pi}{T \mu^y} \int_0^T Z(t, s^*) [1 + \cos(\Phi(t, s^*))] f(t + \phi) dt.
\end{aligned} \tag{17}$$

We show examples of the H -functions in Figure 1. For clarity in the calculations to follow, we define a new function \hat{H}^{jk} in order to write the parameters explicitly.

$$\begin{aligned}
b^x \hat{H}^{xx}(\phi) / \mu^x &= H^{xx}(\phi), \\
-c^x \hat{H}^{xy}(\phi) / \mu^y &= H^{xy}(\phi), \\
b^y \hat{H}^{yx}(\phi) / \mu^x &= H^{yx}(\phi), \\
-c^y \hat{H}^{yy}(\phi) / \mu^y &= H^{yy}(\phi).
\end{aligned}$$

Note that the slope of \hat{H}^{ky} is the opposite of the slope of H^{ky} for $k = x, y$.

Using the tools developed up to this point, we can begin to explore the limitations of the mean field description and test if our phase reduction successfully captures the spiking-level synchronization. For a rudimentary

demonstration of a mean field description that carries no information about microscopic dynamics, we direct our attention to Figure 2.

In this figure, we simulate a small network of $N = 2$ excitatory and $N = 2$ inhibitory theta neurons (for simplicity we define $\phi^x = \theta_2^x - \theta_1^x$, $\phi^y = \theta_2^y - \theta_1^y$, and $\phi^z = \theta_1^y - \theta_1^x$). In the left column, panel A represents the dynamics of the mean field description ($\bar{s}^{x,y}$) overlaid on the full network synaptic variables ($s^{x,y}$) plotted in gray. Panel C shows the synchronization properties of the spiking model, and panel E shows our proposed theory. The theory correctly predicts synchronization of all oscillators. In the right column, panels B, D, and F show the mean field model, spiking model, and proposed theory, respectively. All panels A–F use the same parameters as in Figure 1, except for the right column (panels B, D, and F) where we take $\mu^y = 1.4$. The antiphase lines representing $T^x/2$ (gray solid) and $T^y/2$ (gray dashed) are hard to distinguish because they happen to nearly coincide.

Strikingly, we observe changes in the microscopic synchronization despite virtually no change in the mean field description. There is a slight quantitative change in the mean field descriptions when μ^y changes from $\mu^y = 1$ to $\mu^y = 1.4$. In particular, when $\mu^y = 1$, the fixed point is an asymptotically stable node with real negative eigenvalues. When we increase μ^y to $\mu^y = 1.4$, the fixed point remains stable but becomes a spiral node with small imaginary eigenvalues. Thus, the fixed point remains asymptotically stable and a numerical analysis of the mean field does not reveal any bifurcation points. Moreover, prior knowledge of this quantitative difference gives no indication with regards to the change in synchronization properties.

4.2 Existence of Synchronous Solutions

The existence of synchronous solutions is straightforward to show. Generically, the synchronous solution $\phi_i^x = \phi_i^y = 0$ for $i = 2, \dots, N$ exists independent of ϕ^z (all right-hand-side terms cancel with these values), even when the mean synaptic variables are slowly varying. However, in this slowly varying case, there is synchrony within each excitatory or inhibitory population, but not between populations – the variable ϕ^z undergoes a large phase drift.

Similar solutions are just as straightforward to show. For example, $\phi_i^x = 0$ ($\phi_i^y = 0$) for $i = 1, \dots, N$ gives us $d\phi_i^x/d\tau = 0$ ($d\phi_i^y/d\tau = 0$) independent of the dynamics of ϕ_i^y (ϕ_i^x) and ϕ^z . Thus, it is possible for the excitatory (inhibitory) population to remain synchronous despite a phase drift between populations and possibly asynchronous behavior in the inhibitory (excitatory) population. This behavior is not restricted to the theta model and exists generically.

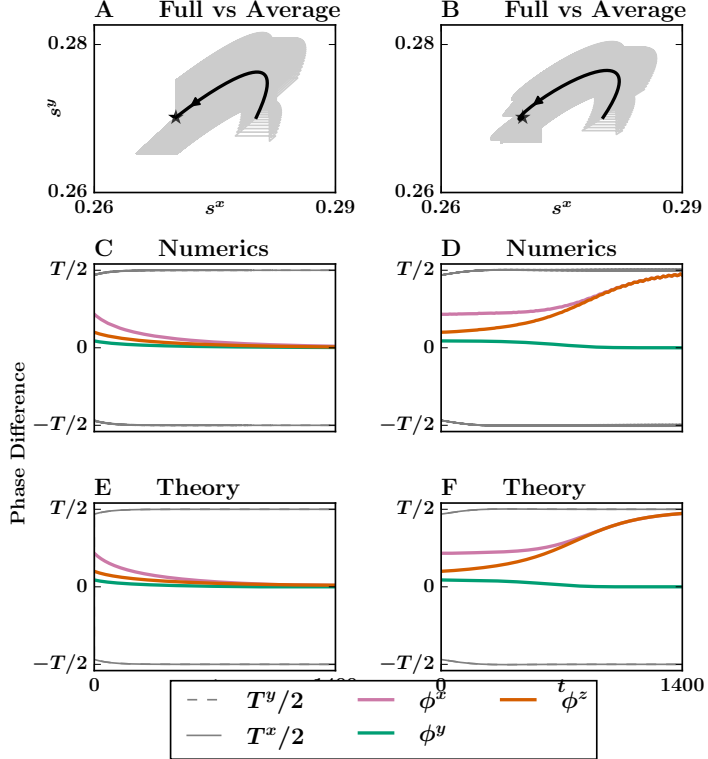


Figure 2: Mean field and microscopic behavior with constant mean synapses. Panel A: mean field synaptic variables ($\bar{s}^{x,y}$, black) plotted on top of the full network synaptic variables ($s^{x,y}$, gray). The black star denotes a stable fixed point. Panel C: phase difference at the spiking level in the full simulation. The estimated anti-phase value is shown in gray solid ($T^x/2$) and gray dashed ($T^y/2$) (they happen to overlap substantially and are almost impossible to distinguish). Panel E: phase difference using our proposed phase reduction. Parameters are the same as in Figure 1 with $\mu^x = \mu^y = 1$ and $\varepsilon = 0.01$. In the right column (panels B, D, and F), we increase $\mu^y = 1$ to $\mu^y = 1.4$ and plot data in the same order as panels A, C, and E, respectively,

4.3 Existence and Stability of Phase-Locked Solutions (Fixed Mean)

We now determine the stability of a given phase-locked solution to Equations (10), (11), and (12) in the case of a fixed mean. To this end, we begin with the most general case of a generic phase-locked solution and construct the Jacobian matrix using the following derivatives:

$$\left[\frac{\partial}{\partial \phi_2^x} \cdots \frac{\partial}{\partial \phi_N^x}, \quad \frac{\partial}{\partial \phi_2^y} \cdots \frac{\partial}{\partial \phi_N^y}, \quad \frac{\partial}{\partial \phi^z} \right].$$

First, consider the partial derivatives with respect to ϕ_k^x , ϕ_k^y , and ϕ^z of the right hand side of $d\phi_i^x/d\tau$:

$$\begin{aligned} N \frac{\partial}{\partial \phi_k^x} \frac{d\phi_i^x}{d\tau} &= \sum_{j=1}^N \left[H_\phi^{xx}(\phi_j^x - \phi_i^x)(\delta_{jk} - \delta_{ik}) - H_\phi^{xx}(\phi_j^x)\delta_{jk} \right], \\ &\quad + \sum_{j=1}^N H_\phi^{xy}(\phi_j^y - \phi_i^x + \phi^z)(-\delta_{ik}), \\ N \frac{\partial}{\partial \phi_k^y} \frac{d\phi_i^x}{d\tau} &= \sum_{j=1}^N \left[H_\phi^{xy}(\phi_j^y - \phi_i^x + \phi^z)\delta_{jk} - H_\phi^{xy}(\phi_j^y + \phi^z)\delta_{jk} \right], \\ N \frac{\partial}{\partial \phi^z} \frac{d\phi_i^x}{d\tau} &= \sum_{j=1}^N \left[H_\phi^{xy}(\phi_j^y - \phi_i^x + \phi^z) - H_\phi^{xy}(\phi_j^y + \phi^z) \right]. \end{aligned} \tag{18}$$

The Kronecker delta functions are defined as

$$\delta_{ij} = \begin{cases} 1, & \text{if } i = j, \\ 0, & \text{else,} \end{cases}$$

and H_ϕ denotes the derivative of H with respect to its independent variable. Next, the partials with respect to ϕ_k^x , ϕ_k^y , ϕ^z of the right hand side of $d\phi_i^y/d\tau$:

$$\begin{aligned} N \frac{\partial}{\partial \phi_k^x} \frac{d\phi_i^y}{d\tau} &= \sum_{j=1}^N \left[H_\phi^{yx}(\phi_j^x - \phi_i^y - \phi^z)\delta_{jk} - H_\phi^{yx}(\phi_j^x - \phi^z)\delta_{jk} \right], \\ N \frac{\partial}{\partial \phi_k^y} \frac{d\phi_i^y}{d\tau} &= \sum_{j=1}^N H_\phi^{yx}(\phi_j^x - \phi_i^y - \phi^z)(-\delta_{ik}), \\ &\quad + \sum_{j=1}^N \left[H_\phi^{yy}(\phi_j^y - \phi_i^y)(\delta_{jk} - \delta_{ik}) - H_\phi^{yy}(\phi_j^y)\delta_{jk} \right], \\ N \frac{\partial}{\partial \phi_k^z} \frac{d\phi_i^y}{d\tau} &= \sum_{j=1}^N \left[H_\phi^{yx}(\phi_j^x - \phi_i^y - \phi^z)(-1) - H_\phi^{yx}(\phi_j^x - \phi^z)(-1) \right]. \end{aligned} \tag{19}$$

Finally, the partials with respect to ϕ_k^x , ϕ_k^y , ϕ^z of the right hand side of $d\phi_i^z/d\tau$:

$$\begin{aligned} N \frac{\partial}{\partial \phi_k^x} \frac{d\phi_i^z}{d\tau} &= \sum_{j=1}^N \left[H_\phi^{yx}(\phi_j^x - \phi^z)\delta_{jk} - H_\phi^{xx}(\phi_j^x)\delta_{jk} \right], \\ N \frac{\partial}{\partial \phi_k^y} \frac{d\phi_i^z}{d\tau} &= \sum_{j=1}^N \left[H_\phi^{yy}(\phi_j^y)\delta_{jk} - H_\phi^{xy}(\phi_j^y + \phi^z)\delta_{jk} \right], \\ N \frac{\partial}{\partial \phi_k^z} \frac{d\phi_i^z}{d\tau} &= \sum_{j=1}^N \left[H_\phi^{yx}(\phi_j^x - \phi^z)(-1) - H_\phi^{xy}(\phi_j^x + \phi^z) \right]. \end{aligned} \tag{20}$$

The synchronous solution, $\phi_i^y = \phi_i^x = 0$ is most straightforward to analyze. In this case, all off-diagonal terms cancel except the last row, so the Jacobian matrix is lower-triangular with diagonal entries

$$\begin{aligned} NJ_{ii} &= -b^x \hat{H}_\phi^{xx}(0)/\mu^x + c^x \hat{H}_\phi^{xy}(0)/\mu^y, \quad i = 1, \dots, N-1 \\ NJ_{ii} &= -b^y \hat{H}_\phi^{yx}(0)/\mu^x + c^y \hat{H}_\phi^{yy}(0)/\mu^y, \quad i = N, \dots, 2N-2 \\ NJ_{2N-1, 2N-1} &= -b^y \hat{H}_\phi^{yx}(0)/\mu^x + c^x \hat{H}_\phi^{xy}(0)/\mu^y. \end{aligned} \quad (21)$$

These entries form the eigenvalues of the Jacobian matrix. We have seen in Figure 1 that $H^{kx}(0)$ has negative slope for $k = x, y$ (panels A,C) and $H^{ky}(0)$ has positive slope (and hence negative slope for $\hat{H}^{ky}(0)$) for $k = x, y$ (panels B,D). Then, for μ^y sufficiently large, the negative contributions from functions H^{ky} are small and the eigenvalues may become positive, indicating a loss of stability to the synchronous solution. This loss of stability confirms our observation in Figure 2.

We found that non-synchronous fixed point attractors of this network take the form $(\phi^x, 0, 0)$, or $(\phi^x, 0, \phi^z)$. For the remainder of this subsection, we analyze the existence and stability of fixed points starting with the synchronous solution $\phi^x = \phi^y = \phi^z = 0$.

We can show that the bifurcation point occurs at $\mu^y = 1.1$ by writing down the eigenvalues of this system (Equation (21) with $N = 2$):

$$\begin{aligned} \lambda_1 &= \left[-H_\phi^{xx}(0) - H_\phi^{xy}(0) \right], \\ \lambda_2 &= \left[-H_\phi^{yx}(0) - H_\phi^{yy}(0) \right], \\ \lambda_3 &= \left[-H_\phi^{yx}(0) - H_\phi^{xy}(0) \right]. \end{aligned}$$

These H functions are identical except for the choice of parameters $b^x = b^y = 1$, and $c^x = c^y = 1.1$ (Equation (17)). By inspection, the eigenvalues are zero when $\mu^x = 1$ and $\mu^y = 1.1$ indicating a change of stability at $\mu^y = 1.1$. This change in stability is shown in Figure 3. When the fixed point loses stability through a transcritical bifurcation, the stable attractor becomes a fixed point of the form $(\phi^x, 0, 0)$, where $\phi^x \neq 0$. For $\mu^y \approx 1.4$, the stable solution approximately takes the form $(-T/2, 0, 0)$, indicating that the excitatory population is stable near anti-phase.

We now turn to the final stable branch, which takes the form $(\phi^x, 0, \phi^z)$ (Figure 4). In panel A, we show the ϕ^x coordinate value as a function of μ^y and panel B shows the ϕ^z coordinate value as a function of μ^y . Initially, synchrony is stable, until the bifurcation at $\mu^y = 1.1$, which leads to a stable branch that asymptotically approaches anti-phase as a function of μ^y , and an unstable branch at the origin. We used XPPAUT to follow the equilibria as a function of μ^y . There exist no other stable fixed points, concluding our analysis of existence and stability in the case of the fixed mean.

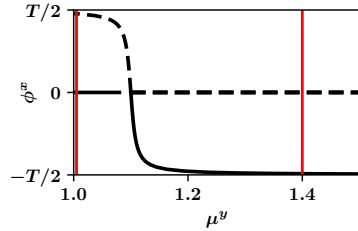


Figure 3: Stability of the fixed point taking the form $(\phi^x, 0, 0)$. The solution $\phi^x = 0$ is stable when $\mu^y = 1$, and becomes unstable as μ^y increases through $\mu^y = 1.1$. When $\mu^y = 1.4$, the stable solution is of the form $(-T/2, 0, 0)$ indicating anti-phase solutions are stable in the excitatory population.

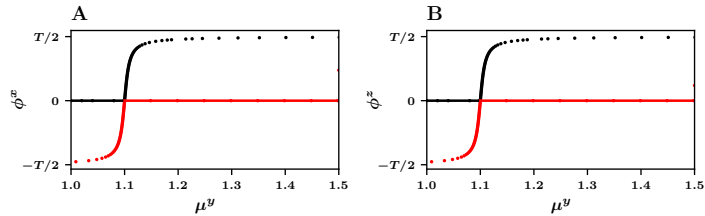


Figure 4: Stability analysis of phase-locked solutions of the form $(\phi^x, 0, \phi^z)$ using parameters from Figures 2 and 1. Black dots and lines: stable fixed points. Red dots and lines: unstable fixed points. A: x-coordinate values of fixed points. B: z-coordinate values of fixed points.

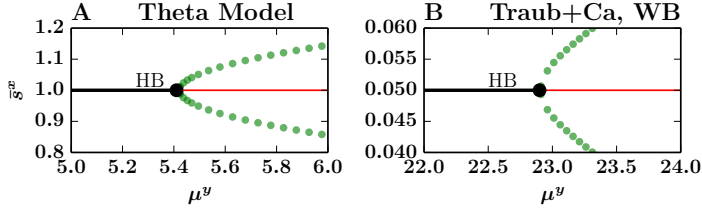


Figure 5: Hopf bifurcations in the mean field (Equation (5)). A: Supercritical Hopf bifurcation in the mean field of the theta network Equations (15) and (16). Parameters $a^x = 0.5, b^x = 7, c^x = 6.5, a^y = 1.1, b^y = 25, c^y = 25.1, \mu^x = 1$. Black: stable fixed point. red solid: unstable fixed point. Green: stable periodic solution. B: Supercritical Hopf bifurcation in the mean field of the Traub+Ca and Wang-Buzsáki network. Parameters $I^{xx} = 101.5 \mu\text{A}/\text{cm}^2, I^{xy} = 104 \mu\text{A}/\text{cm}^2, I^{yx} = 13 \mu\text{A}/\text{cm}^2, I^{yy} = 10.5 \mu\text{A}/\text{cm}^2, \mu^x = 1\text{ms}$

4.4 Existence and Stability of Phase-Locked Solutions (Slowly Varying Mean)

With particular coupling parameter choices, the mean field undergoes a supercritical Hopf bifurcation and gives rise to slow, stable oscillations (Figure 5A). This slowly varying mean has the effect of forcing the excitatory population to spike at a different frequency from the inhibitory population. The goal of this section is to analyze the existence and stability of fixed points of the phase model in this case.

4.4.1 Hopf Bifurcation in the Slowly Varying Case

Figure 6A shows slow, periodic behavior in the mean synaptic values. This periodic solution is a stable limit cycle solution arising from a supercritical Hopf bifurcation. By using the mean field in Equations (15) and (16), we show existence of of a Hopf bifurcation and its criticality numerically.

4.4.2 Phase Models Modulated by Slowly Varying Synapses

Figure 6B shows the results of the numerical simulation in terms of phase differences for $N = 5$ neurons per population. Due to the slowly varying synaptic variables, the period of the oscillators change (as shown by the dashed gray and solid gray anti-phase lines). Generally, the phase differences in the excitatory population, $\phi_1^x, \dots, \phi_4^x$, tend toward non-synchronous phase-locked activity. In contrast, the phase differences in the inhibitory population, $\phi_1^y, \dots, \phi_4^y$, tend toward synchrony. The difference in periods of the oscillators contributes to the phase drift between populations, quantified by ϕ^z (orange).

Figure 6C shows the results of the phase model simulation in terms of the same set of phase differences. We see the same general trends. Excitatory neurons tend to non-synchronous phase-locked solutions, inhibitory neurons tend to synchronize, and there exists a large phase drift between the populations.

4.5 Theta Models with Input Heterogeneities

In this section, we consider the same theta neurons as above with $N = 2$ with an additional input heterogeneity:

$$\begin{aligned} \frac{dx_j}{dt} &= \pi(1 - \cos(x_j) + (1 + \cos(x_j))[(a^x + \varepsilon\eta_j^x) + b^x s^x - c^x s^y]), \\ \frac{dy_j}{dt} &= \pi(1 - \cos(y_j) + (1 + \cos(y_j))[(a^y + \varepsilon\eta_j^y) + b^y s^x - c^y s^y]), \\ \mu^x \frac{ds^x}{dt} &= \varepsilon \left[-s^x + \frac{1}{N} \sum_j \delta(x_j - \pi) \right], \\ \mu^y \frac{ds^y}{dt} &= \varepsilon \left[-s^y + \frac{1}{N} \sum_j \delta(y_j - \pi) \right]. \end{aligned} \quad (22)$$

We place no restriction on the heterogeneities η_j^k , so long as they are chosen such that $\varepsilon\eta_j^k$ remains order ε . In this example, we draw η_j^k from a uniform distribution on the interval $[-1, 1]$. With the numpy [13] random seed set to 0, the four randomly chosen numbers are $[0.09762701, 0.43037873, 0.20552675, 0.08976637]$. We show an example of a simulation in Figure 7.

In Figure 7A, the full network simulation of the synaptic variables (transparent blue, red labeled $s^{x,y}$) differs slightly in mean from the mean field approximation without input heterogeneities (time-averaged synaptic variables solid blue, red labeled $\bar{s}^{x,y}$). In Figure 7B, the input heterogeneity results in a phase drift in the excitatory population (pink). Figure 7C shows our proposed theory, which accurately captures the transient dynamics as well as the phase drift in the excitatory population.

4.6 Wang-Buzsáki and Traub with Calcium

We now repeat the analysis above using biophysically realistic models. In this section, we consider the synchronization properties in two populations of excitatory and inhibitory conductance-based models. The Excitatory population consists of the Traub model [30] with calcium current, while the inhibitory population consists of the Wang Buzsáki model [31]. As in the previous section, we consider two cases. In the first case, the synaptic mean

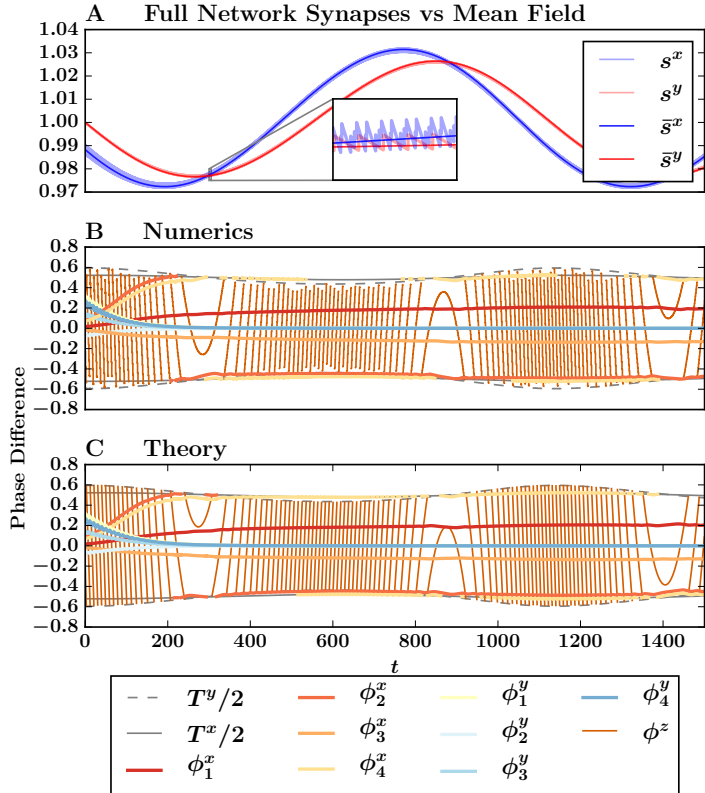


Figure 6: Numerics and theory for the theta model with slowly varying synapses for $N = 5$. A: Mean field solutions $\bar{s}^{x,y}$ (solid lines) vs full network synaptic variables $s^{x,y}$ (opaque lines). Inset: Example of mean field solution plotted over the numerically simulated synaptic solutions. B: Theta model simulation. C: Phase model simulation. The legend at the bottom indicates which variables correspond to which colors. Gray solid and gray dashed lines denote antiphase values $T^x/2$ and $T^y/2$ over time, respectively. Parameters as in Figure 5 and $\varepsilon = 0.005$.

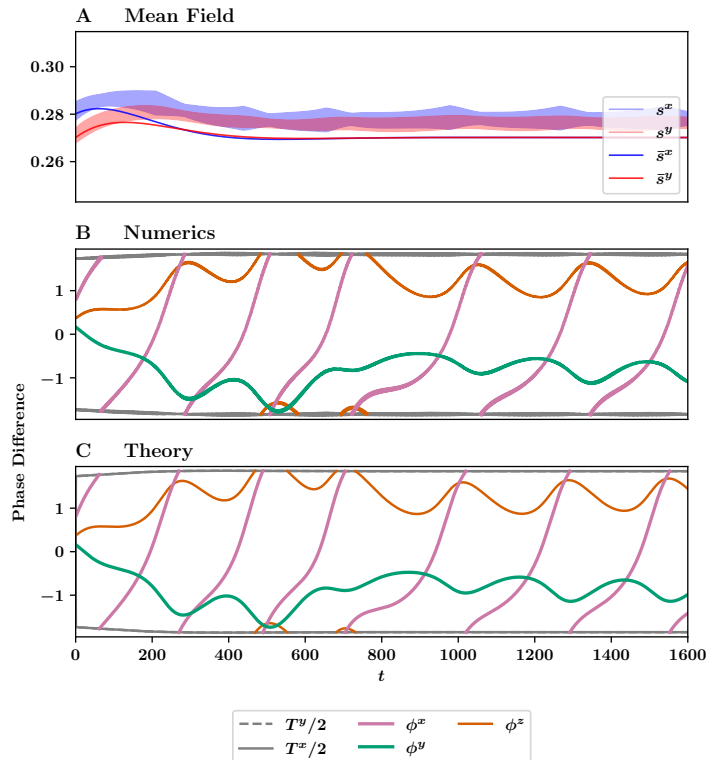


Figure 7: Effects of input heterogeneity. A: The full network simulation of the synaptic variables (transparent blue, red labeled $s^{x,y}$) and the mean field approximation without input heterogeneities (solid blue, red labeled $\bar{s}^{x,y}$). B: Oscillator phase differences in the full network simulation. C: Predicted oscillator phase differences in the reduced model. Parameter values are the same as in Figure 1 and Figure 2, with $\mu^y = 1.5$, $\varepsilon = 0.01$.

values are fixed, and in the second case, the synaptic mean values are slowly varying.

The Traub model with calcium is defined by the system

$$\dot{\mathbf{x}} = \frac{d}{dt} \begin{pmatrix} V \\ x \\ w \\ [\text{Ca}] \end{pmatrix} = \begin{pmatrix} (-I_{\text{ionic}} + I_{\text{ext}})/C \\ a_x(V)(1-x) - b_x(V)x \\ (w_\infty(V) - w)/\tau_w(V) \\ (-\alpha I_{\text{Ca}} - [\text{Ca}]/\tau_{\text{Ca}}) \end{pmatrix} = \mathbf{F}^x(\mathbf{x}, I_{\text{ext}}) \quad (23)$$

where x represents the dynamics of gating variables h, m , and n . The ionic currents are listed in Equation (27) of Appendix A.1.

The Wang-Buzsáki system is given by

$$\dot{\mathbf{y}} = \frac{d}{dt} \begin{pmatrix} V \\ x \end{pmatrix} = \begin{pmatrix} -I_{\text{ionic}} + I_{\text{ext}} \\ \phi(x_\infty - x)/\tau_x \end{pmatrix} = \mathbf{F}^y(\mathbf{y}, I_{\text{ext}}), \quad (24)$$

where x represents the dynamics of gating variables h and n . The ionic currents are listed in Equation (28) of Appendix A.1.

We introduce coupling through currents:

$$\begin{aligned} \frac{d\mathbf{x}_i}{dt} &= \mathbf{F}^x(\mathbf{x}_i, I^x + I^{xx}s^x - I^{xy}s^y), \\ \frac{d\mathbf{y}_i}{dt} &= \mathbf{F}^y(\mathbf{y}_i, I^y + I^{yx}s^x - I^{yy}s^y), \\ \mu^x \frac{ds^x}{dt} &= \varepsilon \left[-s^x + \frac{1}{N} \sum_{i=1}^N \sum_j \delta(t - t_{i,j}^x) \right], \\ \mu^y \frac{ds^y}{dt} &= \varepsilon \left[-s^y + \frac{1}{N} \sum_{i=1}^N \sum_j \delta(t - t_{i,j}^y) \right], \end{aligned} \quad (25)$$

where just as in Equations (1)–(4), $t_{i,j}^x$ ($t_{i,j}^y$) is the time of the j^{th} spike of neuron i in population \mathbf{x} (\mathbf{y}).

Aside: While we also could include synaptic coupling using conductance-based synapses, the mean field equations are more complex as they are not just functions of sums of excitatory and inhibitory currents. Thus, we will use the simpler type of coupling shown in Equation (25).

The synapses s^x, s^y (dimensionless) increment each time the voltage variable of the neural models cross $V = 0$ from negative to positive. Unless otherwise stated, we choose $s^* = 1/T = 0.05$ cycles/ms = 50 Hz.

The mean field dynamics obey Equation (5), where ω^x is given by the frequency-input current (FI) function shown by the black curve in Figure 8 and ω^y is shown by the FI curve given by the dashed curve in the same figure. We compute both curves numerically using XPPAUT0 [9].

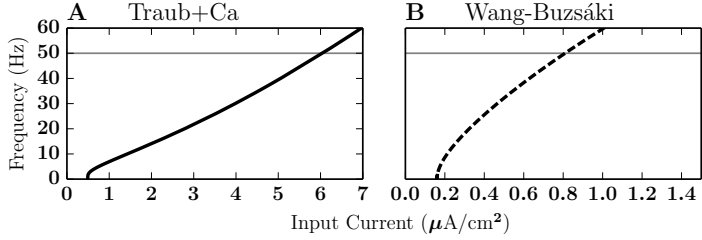


Figure 8: The frequency-current (FI) curves of the Traub with calcium model (solid black) and Wang-Buzsaki model (dashed black). Frequency is in units of cycles per second. The horizontal gray line through the frequency value 0.05 denotes our choice of fixed mean synaptic current. Small and slow oscillations of the synaptic variables in this network are about this mean value and are fully determined by the values of these FI curves.

This choice of coupling in Equation (25) results in scalar derivatives:

$$\begin{aligned}\mathbf{F}_{sx}^x(\Phi^x(t), s^*, s^*) &= (I^{xx}, 0, 0, 0, 0, 0, 0)^T, \\ \mathbf{F}_{sy}^x(\Phi^x(t), s^*, s^*) &= (-I^{xy}, 0, 0, 0, 0, 0, 0)^T, \\ \mathbf{F}_{sx}^y(\Phi^y(t), s^*, s^*) &= (I^{yx}, 0, 0)^T, \\ \mathbf{F}_{sy}^y(\Phi^y(t), s^*, s^*) &= (-I^{yy}, 0, 0)^T.\end{aligned}$$

Thus the H functions of Equations (8) and (9) for this system are given by

$$\begin{aligned}H^{xx}(\phi) &= \frac{I^{xx}}{T\mu^x} \int_0^T Z^x(t, s^*) f(t + \phi) dt, \\ H^{xy}(\phi) &= -\frac{I^{xy}}{T\mu^y} \int_0^T Z^x(t, s^*) f(t + \phi) dt, \\ H^{yx}(\phi) &= \frac{I^{yx}}{T\mu^x} \int_0^T Z^y(t, s^*) f(t + \phi) dt, \\ H^{yy}(\phi) &= -\frac{I^{yy}}{T\mu^y} \int_0^T Z^y(t, s^*) f(t + \phi) dt.\end{aligned}\tag{26}$$

We show plots of these H functions in Figure 9.

In Figure 10, we simulate 2 excitatory Traub with calcium conductance-based models (Traub with calcium, Equation (23)), and 2 inhibitory conductance-based models (Wang-Buzsaki, Equation (24)) with constant mean-field dynamics. All parameter values are the same except the parameter $\mu^y = 1$ (left column) and $\mu^y = 2.5$ (right column).

We plot the mean field in panels A and B using the same scale to emphasize the qualitative difference in the mean field description. The stability remains the same between the left and right columns (negative real eigenvalues in both cases). The double-headed red arrow indicates the magnitude

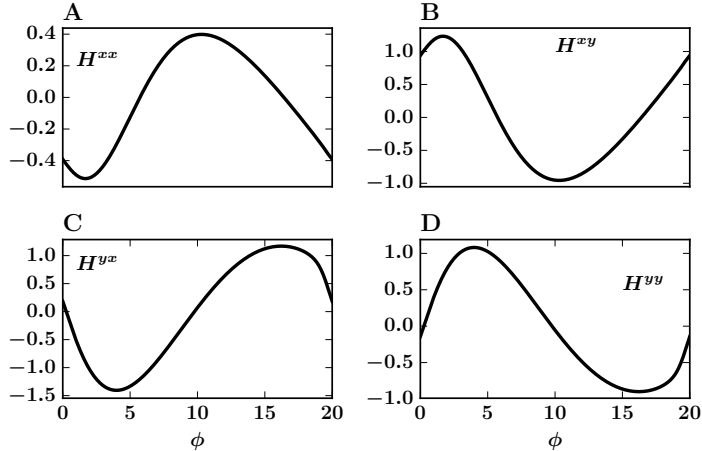


Figure 9: The H functions of the Traub with calcium and Wang-Buzsáki network. A: H^{xx} . B: H^{xy} . C: H^{yx} . D: H^{yy} . Parameter values $I^{xx} = 10\mu\text{A}/\text{cm}^2$, $I^{xy} = 14\mu\text{A}/\text{cm}^2$, $I^{yx} = 13\mu\text{A}/\text{cm}^2$, $I^{yy} = 10\mu\text{A}/\text{cm}^2$, $\mu^x = \mu^y = 1\text{ms}$.

of the perturbation off the fixed point. In both columns we choose to perturb the s^x variable by magnitude $\varepsilon/4$, where $\varepsilon = 0.0025$. Interestingly, this system exhibits similar features in the mean field description shown in Figure 2, and the microscopic dynamics reach different steady-states despite no detectable changes to the stability of the mean field model.

Panel C shows that the excitatory (ϕ^x , purple) and inhibitory populations (ϕ^y , green) approach synchrony. In panel D, we re-initialize the simulation with the same initial conditions for all variables with only one change in the synaptic time constant from $\mu^y = 1$ to $\mu^y = 2.4$. The excitatory population reaches a non-synchronous steady-state phase locked value, indicating nearly a quarter-period difference in spike times. Panels E and F show that our theory correctly predicts the differing steady state dynamics in panels C and D, respectively.

4.6.1 Existence and Stability of Phase-Locked Solutions (Fixed Mean)

We now analyze the phase locked solutions of this system in the case of constant-mean synapses. As in the network of theta neurons, we use coupling parameters that lead to changes in the synchronization properties of the oscillators as a function of μ^y , while the mean field remains invariant. We show the existence and stability of phase locked solutions of Figure 10 in Figure 11.

In Figure 11 we plot the value of each coordinate as a function of μ^y (ϕ^x in panel A and ϕ^z in panel B). We do not show ϕ^y because $\phi^y = 0$

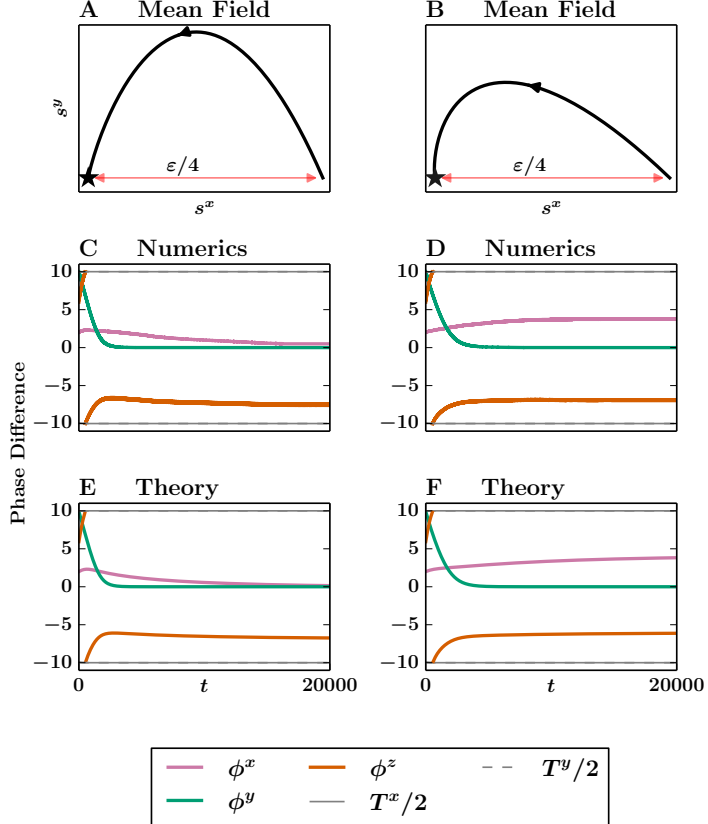


Figure 10: Mean field description and microscopic behavior with constant mean synapses. A: mean synaptic variables ($\bar{s}^{x,y}$, black). The star denotes a stable fixed point. C: phase difference at the spiking level in the full conductance-based model simulation. The estimated half-period is shown in gray solid ($T^x/2$) and gray dashed ($T^y/2$) (they happen to overlap substantially and are almost impossible to distinguish). E: phase difference using our proposed phase reduction. Parameters are the same as in Figure 9, and $\mu^x = \mu^y = 1$. In the right column, we increase $\mu^y = 1$ to $\mu^y = 2.5$ and plot the same data in the same order with the same initial conditions. Other parameters: $\varepsilon = 0.0025$, $I^x = 6.74\mu\text{A}/\text{cm}^2$, $I^y = 0.66\mu\text{A}/\text{cm}^2$.

for this parameter range. As expected, the point $(\phi^x, \phi^y, \phi^z) \approx (0, 0, 3T/4)$ is stable for $\mu^y = 1$. As we increase μ^y , the system undergoes a pitch-fork bifurcation, resulting in two stable fixed points. The fixed point we see in Figure 10 corresponds to the upper branch of both panels, where $(\phi^x, \phi^y, \phi^z) \approx (T/4, 0, 3T/4)$.

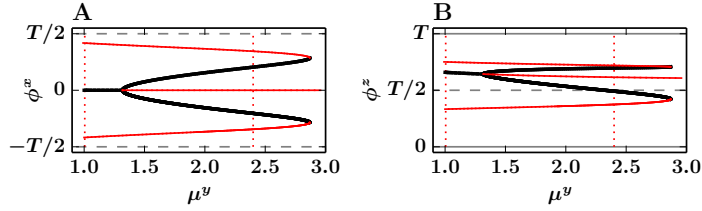


Figure 11: Existence and stability of phase locked solutions in the Traub Wang-Buzsáki network. Vertical red dotted lines denote the two parameter values corresponding to the left and right columns of Figure 10. Black curves denote stable values and solid red curves denote unstable values. A: Branches of ϕ^x fixed point values. B: Branches of ϕ^z fixed point values. Generally, $\phi^y = 0$ (data not shown). Note that for $\mu^y = 1$, the only fixed point that exists agrees with the steady-state in Figure 10. For $\mu^y = 2.4$, the fixed point corresponding to the lower stable branch of panel A and the upper stable branch of panel B coincides with the right column of Figure 10. Parameter values are identical to Figure 10.

4.6.2 Phase Locked Solutions (Slowly Varying Mean)

Finally, as in the theta network, the mean field of the Traub+Ca and Wang-Buzsáki network may undergo a supercritical Hopf bifurcation (Figure 5B). In this section, we demonstrate that our theory accurately predicts the phase locking properties in this case of a slowly varying mean (Figure 12). We show the synaptic variables and mean field approximations in the top panel, the full numerical simulation in the middle panel, and our proposed theory in the bottom panel. We find that our theory correctly predicts the general trend of ϕ^x (pink) which tends towards antiphase, and of ϕ^y (green) which remains close to its initial condition.

5 Discussion

In the current study, we have shown that in an all-to-all, homogeneously coupled network of heterogeneous oscillators, there are two cases of the mean synaptic values that make the oscillators amenable to a phase reduction. In the first case, the mean synaptic values are fixed and equal, or fixed and different up to a small difference of order ε . In the second case, the mean synaptic values are slowly varying with small amplitude up to order ε . Using neurophysiologically motived models, we demonstrate that the phase reduction is accurate for at least order $1/\varepsilon$ time. Moreover, we are able to explore the existence and stability of phase locked solutions in both cases.

Our choice of coupling in the Traub, Wang-Buzsáki network also simplifies the analysis, but we need not restrict the form of the input current. In

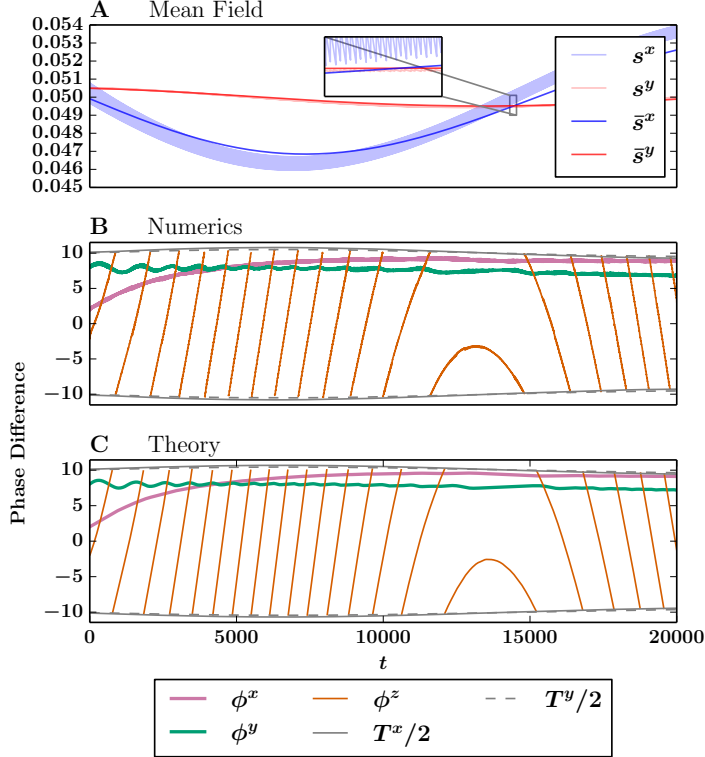


Figure 12: Numerics and theory for the Wang-Buzsáki and Traub with calcium models with nonconstant mean synapses $\bar{s}^{x,y}$. A: Mean field solutions ($\bar{s}^{x,y}$, solid lines) vs numerical synaptic variables ($s^{x,y}$, opaque lines). Inset: Example of mean field solution plotted over the numerically simulated synaptic solutions. B: Theta model simulation. C: Phase model simulation. Parameters $I^{xx} = 101.5\mu\text{A}/\text{cm}^2$, $I^{xy} = 104\mu\text{A}/\text{cm}^2$, $I^{yx} = 13\mu\text{A}/\text{cm}^2$, $I^{yy} = 10.5\mu\text{A}/\text{cm}^2$, $\mu^x = 1\text{ms}$, $\mu^y = 24.79\text{ms}$, $\varepsilon = 0.00125$.

fact, a biophysically realistic synaptic input current of the form $s^k g(V - V^k)$, where g represents a conductance, V^k the reversal potential, and s^k the synaptic variable, is well within the scope of this study. In this case, we would add more complexity to the H functions in Equation (26) and in the mean field equations, but the analysis remains otherwise unchanged.

Particular elements and motives of the current study are similar to existing works. Early studies in bridging spiking models to the mean field description use leaky integrate-and-fire (LIF) models with Poisson statistics [2, 1]. Later studies derive additional statistics like the coefficient of variation in the interspike interval [26]. However, deriving equations measuring the degree of synchrony in a population of neurons (the order parameter [17]) is more recent. This reduction was first shown in Ott and Antonsen 2008[23], where the authors use what is now called the Ott-Antonsen ansatz

to reduce an infinite number of Kuramoto oscillators into a simple pair of differential equations for the order parameter.

In Montrio et al. 2015[21], the authors derive a pair of ordinary differential equations for other macroscopic observables like the mean membrane potential and the firing rate by starting at the spiking level. They then show that the network is also amenable to the order parameter reduction using the Ott-Antonsen ansatz. Thus, it is possible to derive a complementary set of equations describing the mean field activity and the associated degree of synchronization. This derivation has also been applied to theta neurons in Coombes and Byrne 2016[7], where the authors derive a complementary set of ordinary differential equations describing the population firing rate and the degree of synchrony.

The excitatory-inhibitory network structure has also been studied previously. In Roulet and Mindlin 2016[27], they use the Ott-Antonsen ansatz to derive low dimensional differential equations for the order parameters of networks of excitatory and inhibitory Alder units:

$$\begin{aligned}\dot{\theta}_i &= \omega_i - \cos \theta_i + I(\theta_j, \tilde{\theta}_j), \\ \dot{\tilde{\theta}}_i &= \tilde{\omega}_i - \cos \tilde{\theta}_i + \tilde{I}(\theta_j, \tilde{\theta}_j),\end{aligned}$$

where the untilded variables refer to units in the excitatory population and the tilded variables refer to units in the inhibitory population. The coupling functions are defined as

$$I(\theta_j, \tilde{\theta}_j) = \frac{k_E}{N} \sum_{j=1}^N (1 - \cos \theta_j) - \frac{k_I}{\tilde{N}} \sum_{j=1}^{\tilde{N}} (1 - \cos \tilde{\theta}_j),$$

where $k_E, k_I > 0$ denote the coupling strengths, N and \tilde{N} denote the number of neurons in each of the two populations.

Roulet and Mindlin then derive low dimensional differential equations for the order parameters of excitatory and inhibitory theta models:

$$\begin{aligned}\dot{\theta}_i &= 1 - \cos \theta_i + (1 + \cos(\theta_i))[\eta_i + I(\theta_j, \tilde{\theta}_j)], \\ \dot{\tilde{\theta}}_i &= 1 - \cos \tilde{\theta}_i + (1 + \cos \tilde{\theta}_i)[\tilde{\eta}_i + \tilde{I}(\theta_j, \tilde{\theta}_j)],\end{aligned}$$

with the same coupling functions as above. The equations are similar to the theta model we consider in this paper, except that the mean of the input current is slaved to the fixed parameters η_i and thus the mean can not drift over time.

Aspects of our results have been considered in various studies, which we now summarize. In So et al. 2008[29], the authors consider the effects of time-varying coupling on the synchronization properties of a network of Kuramoto oscillators. In particular, they show that with sufficiently fast

binary switching of coupling strengths, the network exhibits behavior characteristic of a static network. In contrast, our results apply only to slow, continuous changes in input current. Next, although slow synapses exist in neural networks, synapses are not generally slow. Indeed, the problem of slow synapses has been addressed in Laing 2014, 2015[19, 18], where he derives a mean-field description of theta models while allowing for arbitrarily fast synaptic transmission. However, our results are a step in two important directions. One, we give our synapses their own dynamics, as is often the case in chemical synapses (as opposed to gap junction synapses), and two, the synaptic variables are additionally allowed to vary independently. Granted, they are only allowed to vary within a small neighborhood of a fixed point, but to the best of our knowledge, this independence is novel and generalizes existing studies [28].

Another aspect of the our results that have been studied in the past includes pulse coupled oscillators. Pazó and Montbrió[25], use the Winfree model with a smooth pulse-like coupling of the form $P(x) = a_n(1 + \cos(x))^n$. Combined with the Ott-Antonsen ansatz, they derive a pair of differential equations for the order parameter. In Chandra et al. 2017[4], the authors consider a network of theta models with similar pulse-like coupling and derive the order parameter using the Ott-Antonsen ansatz. In addition, they relax the all-to-all coupling hypothesis and apply the Ott-Antonsen ansatz to a randomly generated network given an arbitrary degree distribution. General network structure satisfying classic weak coupling assumptions are studied in Kori et al. 2009[16]. In Laing 2018[20], the author considers all-to-all pulse-like coupling of theta neurons with and without synaptic delay and derives the order parameter using the Watanabe-Strogatz ansatz [33, 32].

Generalizing the synaptic weights is also a natural next step of the current study. In this case, the system becomes

$$\begin{aligned} \frac{d\mathbf{x}_i}{dt} &= \mathbf{F}^x \left(\mathbf{x}_i, \sum_{j=1}^N w_{ij}^{xx} s_j^x, \sum_{j=1}^N w_{ij}^{xy} s_j^y \right), \\ \frac{d\mathbf{y}_i}{dt} &= \mathbf{F}^y \left(\mathbf{y}_i, \sum_{j=1}^N w_{ij}^{yx} s_j^x, \sum_{j=1}^N w_{ij}^{yy} s_j^y \right), \\ \mu_i^x \frac{ds_i^x}{dt} &= \varepsilon \left[-s_i^x + \sum_j \delta(t - t_{i,j}^x) \right], \\ \mu_i^y \frac{ds_i^y}{dt} &= \varepsilon \left[-s_i^y + \sum_j \delta(t - t_{i,j}^y) \right], \quad i = 1 \dots, N. \end{aligned}$$

The time values $t_{i,j}^x$ and $t_{i,j}^y$ are as in Equations (1)–(4). To ensure that all neurons have the same firing rate when the synaptic variables are constant

and identical, we require that

$$\sum_j w_{ij}^{jk} = \bar{w}^{jk}, \quad i = 1, \dots, N, \text{ for } j, k = x, y,$$

where \bar{w}^{jk} is a constant for each $j, k = x, y$. We are then free to choose coupling types of the form $W_{ij} = K(|i - j|\Delta x)$, where K is a typical even kernel, like a Gaussian or difference of Gaussians, and $\Delta x = 1/N$. This type of modification brings us closer to classic spatially distributed neural field models and the resulting system remains amenable to the methods of the current study. This direction also ties in with Laing 2014, 2015[19, 18], where bump-type solutions are shown to exist *a priori* in large networks of theta models. Our method could show the same results with more general models.

The Ott-Antonsen ansatz is an undoubtedly powerful tool for understanding oscillator models. However, it has some limitations which the current paper addresses directly. Our proposed theory offers a general dimension reduction of a finite number of N - and M -dimensional coupled oscillators. While our theory tolerates only small heterogeneities, we place no restrictions on how the heterogeneities are distributed. However, our theory is restrictive in that the interactions must be on a slow timescale.

Another natural next step to consider involves the effects of noise on synchronization. In Nagai and Kori 2010[22], where a network of these oscillators are driven by a common Gaussian noise signal, the authors analytically show noise-induced synchronization, and suggest that weak common noise generally promotes synchronization of weakly coupled oscillators. We have shown to a limited extent the effects of noise by introducing input heterogeneities drawn from a uniform distribution. However, analyzing the effects of a single time-dependent noisy input signal in our framework requires different techniques beyond the scope of this paper, and warrants close study in its own right.

Acknowledgments

GBE and YMP were partially supported by NSF DMS 1712922, and the Andrew Mellon predoctoral fellowship.

A Model Equations and Parameters

A.1 Traub With Calcium

$$\dot{\mathbf{x}} = \frac{d}{dt} \begin{pmatrix} V \\ x \\ w \\ [\text{Ca}] \end{pmatrix} = \begin{pmatrix} (-I_{\text{ionic}} + I_{\text{ext}})/C \\ a_x(V)(1-x) - b_x(V)x \\ (w_\infty(V) - w)/\tau_w(V) \\ (-\alpha I_{\text{Ca}} - [\text{Ca}]/\tau_{\text{Ca}}) \end{pmatrix} = \mathbf{F}^x(\mathbf{x}, I_{\text{ext}})$$

where x represents the dynamics of gating variables h, m , and n , and

$$\begin{aligned} I_{\text{ionic}} &= I_{\text{Na}} + I_{\text{K}} + I_{\text{Ca}} + I_{\text{ahp}} + I_{\text{M}} + g_{\text{L}}(V - E_{\text{L}}) \\ I_{\text{Na}} &= g_{\text{Na}}m^3h(V - E_{\text{Na}}) \\ I_{\text{K}} &= g_{\text{K}}n^4(V - E_{\text{K}}) \\ I_{\text{Ca}} &= g_{\text{Ca}}M_{\infty}(V)(V - E_{\text{Ca}}) \\ I_{\text{ahp}} &= \frac{g_{\text{ahp}}[\text{Ca}](V - E_{\text{K}})}{[\text{Ca}] + K_{\text{d}}} \\ I_{\text{M}} &= g_{\text{M}}w(V - E_{\text{K}}) \end{aligned} \tag{27}$$

The voltage variable V has dimensions of mV, all currents are in dimensions of $\mu\text{A}/\text{cm}^2$, time is in units of milliseconds, the variables n, m, h , and w are dimensionless, and the variable $[\text{Ca}]$ represents the intracellular calcium concentration in millimolar units. We show dimensions of all model parameters in Table 1.

$$\begin{aligned}
a_m(V) &= \frac{0.32(V + 54)}{1 - \exp(-(V + 54)/4)} \\
b_m(V) &= \frac{0.28(V + 27)}{\exp((V + 27)/5) - 1} \\
a_h(V) &= 0.128 \exp(-(V + 50)/18) \\
b_h(V) &= \frac{4}{1 + \exp(-(V + 27)/5)} \\
a_n(V) &= \frac{0.032(V + 52)}{1 - \exp(-(V + 52)/5)} \\
b_n(V) &= 0.5 \exp(-(V + 50)/40) \\
\tau_w(V) &= \frac{\tau_w}{3.3 \exp((V - V_{wt})/20) + \exp(-(V - V_{wt})/20)} \\
w_\infty(V) &= \frac{1}{1 + \exp(-(V - V_{wt})/10)} \\
M_{L\infty}(V) &= 1/(1 + \exp(-(V - V_{L\text{th}})/V_{\text{shp}}))
\end{aligned}$$

A.2 Wang-Buzsáki

$$\dot{\mathbf{y}} = \frac{d}{dt} \begin{pmatrix} V \\ x \end{pmatrix} = \begin{pmatrix} -I_{ionic} + I_{ext} \\ \phi(x_\infty - x)/\tau_x \end{pmatrix} = \mathbf{F}^y(\mathbf{y}, I_{ext}),$$

where x represents the dynamics of gating variables h and n , and

$$\begin{aligned}
I_{ionic} &= g_L(V - E_L) + I_{Na} + I_K \\
I_{Na} &= g_{Na} m_\infty^3 h (V - E_{Na}) \\
I_K &= g_K n^4 (V - E_K)
\end{aligned} \tag{28}$$

As in the Traub model above, the variable V has dimensions of mV, time units of milliseconds, the variables h and n are dimensionless, and currents are in units of $\mu\text{A}/\text{cm}^2$. We show dimensions of all model parameters in Table 2.

Table 1: Traub with calcium parameter values

Parameter	Value
C	1 $\mu\text{F}/\text{cm}^2$
E_K	-100mV
E_{Na}	50mV
E_L	-67mV
E_{Ca}	120mV
g_L	0.2mS/cm ²
g_K	80mS/cm ²
g_{Na}	100mS/cm ²
g_m	0mS/cm ²
g_{Ca}	1mS/cm ²
g_{ahp}	0.5mS/cm ²
K_d	1mM
α	0.002mmol/(cm \times nC)
τ_{Ca}	80ms
V_{shp}	2.5mV
V_{Lth}	-25mV
V_{sshp}	2mV
V_{th}	-10mV
V_{wt}	-35mV
τ_w	100ms

Table 2: Wang-Buzsáki parameter values

Parameter	Value
E_K	-90mV
E_{Na}	55mV
E_L	-65mV
g_L	0.1mS/cm ²
g_{Na}	35mS/cm ²
g_K	9mS/cm ²
ϕ	5

$$\begin{aligned}
\alpha_m(V) &= \frac{0.1(V + 35)}{1 - \exp(-(V + 35)/10)} \\
\beta_m(V) &= 4 \exp(-(V + 60)/18) \\
\alpha_h(V) &= 0.07 \exp(-(V + 58)/20) \\
\beta_h(V) &= \frac{1}{1 + \exp(-(V + 28)/10)} \\
\alpha_n(V) &= \frac{0.01(V + 34)}{1 - \exp(-(V + 34)/10)} \\
\beta_n(V) &= 0.125 \exp(-(V + 44)/80) \\
x_\infty &= x_1/(x_1 + x_2) \\
\tau_x &= 1/(x_1 + x_2)
\end{aligned}$$

where x in the last two lines represents m , h , or n and x_1, x_2 may be α_x and β_x , respectively.

B Derivation of Spiking Term

Recall our starting ansatz for the phase equation,

$$\begin{aligned}
\mathbf{x}_i(t, \tau) &= \mathbf{x}_i(t + \theta_i(\tau), s^*) = \Phi^x(t + \theta_i^x(\tau), s^*) + \varepsilon \xi_i^x(t + \theta_i^x(\tau), s^*) + O(\varepsilon^2), \\
\mathbf{y}_i(t, \tau) &= \mathbf{y}_i(t + \theta_i(\tau), s^*) = \Phi^y(t + \theta_i^y(\tau), s^*) + \varepsilon \xi_i^y(t + \theta_i^y(\tau), s^*) + O(\varepsilon^2), \\
s^x(t, \tau) &= s^*(\tau) + \frac{\varepsilon}{N\mu^x} \sum_j f(t + \theta_j^x(\tau)) + O(\varepsilon^2), \\
s^y(t, \tau) &= s^*(\tau) + \frac{\varepsilon}{N\mu^y} \sum_j f(t + \theta_j^y(\tau)) + O(\varepsilon^2),
\end{aligned}$$

where f represents the small-magnitude, fast-timescale effects of the variables $\mathbf{x}_i(t, \tau)$ and $\mathbf{y}_i(t, \tau)$ on the synaptic variables. In this section, we derive

the order ε term f :

$$f(t + \theta) = [(1 - (t + \theta)/T \pmod{1}) - 1/2].$$

For simplicity, consider a network consisting of one excitatory neuron \mathbf{x}_1 with one synaptic variable $s^x(t, \tau)$. Note that following a spike, the solution \mathbf{x}_1 increments by $\varepsilon_k \equiv \varepsilon/\mu^k$ and decays exponentially. Moreover, each s^k is periodic with $s^k(T^+) = s^k(0)$, where $k = x, y$. Putting these facts together, we have that

$$s^k(T^+) = s^k(0)e^{-\varepsilon_k T} + \varepsilon_k = s^k(0).$$

Solving for $s^k(0)$ reveals

$$s^k(0) = \frac{\varepsilon_k}{1 - e^{-\varepsilon_k T}}.$$

Therefore, $s^k(t)$ after a spike is

$$s^k(t) = \frac{\varepsilon_k}{1 - e^{-\varepsilon_k T}} e^{-\varepsilon_k t}.$$

Using Taylor expansions, we can rearrange the equation as

$$s^k(t) = \frac{\varepsilon_k}{1 - e^{-\varepsilon_k T}} e^{-\varepsilon_k t} = \frac{1}{T} + \varepsilon_k f(t),$$

which after a trivial rearrangement yields

$$\varepsilon_k f(t) = \frac{\varepsilon_k}{1 - e^{-\varepsilon_k T}} e^{-\varepsilon_k t} - \frac{1}{T}.$$

Since ε_k is small, we take a Taylor expansion of the exponential and simplify in a series of algebraic steps:

$$\begin{aligned} \varepsilon_k f(t) &= \frac{\varepsilon_k(1 - \varepsilon_k t + O(\varepsilon_k^2))}{1 - (1 - \varepsilon_k T + (\varepsilon_k T)^2/2 + O(\varepsilon_k^3))} - \frac{1}{T} \\ &= \frac{1 - \varepsilon_k t + O(\varepsilon_k^2)}{T - \varepsilon_k T^2/2 + O(\varepsilon_k^2)} - \frac{1}{T} \\ &= \frac{1}{T} \frac{1 - \varepsilon_k t + O(\varepsilon_k^2)}{1 - \varepsilon_k T/2 + O(\varepsilon_k^2)} - \frac{1}{T} \\ &= \frac{1}{T} \left(\frac{1 - \varepsilon_k t + O(\varepsilon_k^2)}{1 - \varepsilon_k T/2 + O(\varepsilon_k^2)} - \frac{1 - \varepsilon_k T/2 + O(\varepsilon_k^2)}{1 - \varepsilon_k T/2 + O(\varepsilon_k^2)} \right) \\ &= \frac{1}{T} \frac{\varepsilon_k T/2 - \varepsilon_k t + O(\varepsilon_k^2)}{1 - \varepsilon_k T/2 + O(\varepsilon_k^2)} \frac{1 + \varepsilon_k T/2 + O(\varepsilon_k^2)}{1 + \varepsilon_k T/2 + O(\varepsilon_k^2)} \\ &= \frac{1}{T} \frac{\varepsilon_k T/2 - \varepsilon_k t + O(\varepsilon_k^2)}{1 + O(\varepsilon_k^2)} \\ &\approx \frac{1}{T} \varepsilon_k (T/2 - t). \end{aligned}$$

Thus,

$$f(t) = \left(\frac{1}{2} - \frac{t}{T} \right),$$

over one period. For multiple periods, the resulting function is a sawtooth. In our implementations we write

$$f(t) = ((1 - t/T) \pmod 1) - 1/2,$$

because it is the most natural formulation for computer simulations. In general, we need to account for possible slow timescale phase shifts $\theta_j^k(\tau)$ and the contributions from multiple spikes. We simply sum these contributions to arrive at the desired form:

$$\frac{\varepsilon}{N\mu^x} \sum_j f(t + \theta_j^x(\tau)).$$

C Fourier Coefficients

Table 3: H-function coefficients of the theta model. The series takes the form $\sum_{i=1}^n a_i \cos(ix) + b_i \sin(ix)$. Error = 7e-3.

Coefficient	H^{xx}	H^{xy}	H^{yx}	H^{yy}
a_1	0.006693442	-0.00736278	0.006693442	-0.00736278
b_1	-1.09191412	1.201105540	-1.09191412	1.201105540

Table 4: H -function coefficients of the Traub with calcium (H^{xx}, H^{xy}) and Wang-Buzsáki (H^{yx}, H^{yy}). $a_0 + \sum_{i=1}^n a_i \cos(ix) + b_i \sin(ix)$. Maximum pointwise error = 1e-2.

Coefficient	H^{xx}	H^{xy}	H^{yx}	H^{yy}
a_0	-0.00014179	0.000340298		
a_1	-0.40559133	0.973419204	0.014799680	-0.01138436
a_2	-0.00296584	0.007118019	0.120314654	-0.09254973
a_3	0.008194908	-0.01966778	0.045877649	-0.03529049
a_4	0.003950934	-0.00948224	0.016650161	-0.01280781
a_5	0.001870675	-0.00448962	0.004690780	-0.00360829
a_6	0.000941694	-0.00226006	-0.00025889	0.000199148
a_7	0.000497815	-0.00119475	-0.00214311	0.001648549
a_8	0.000271530	-0.00065167	-0.00264425	0.002034040
a_9	0.000151095	-0.00036262	-0.00253634	0.001951034
a_{10}	8.560764307	-0.00020545	-0.00218981	0.001684474
b_1	-0.14512093	0.348290252	-1.29140450	0.993388080
b_2	-0.07327966	0.175871190	-0.22112111	0.170093167
b_3	-0.01561869	0.037484866	-0.07939645	0.061074193
b_4	-0.00449755	0.010794122	-0.03842115	0.029554737
b_5	-0.00168564	0.004045538	-0.02107670	0.016212846
b_6	-0.00073921	0.001774105	-0.01208433	0.009295643
b_7	-0.00034753	0.000834072	-0.00691601	0.005320008
b_8	-0.00016011	0.000384282	-0.00380417	0.002926287
b_9	-6.11449933	0.000146747	-0.00190524	0.001465571
b_{10}	-5.59280546	1.342273311	-0.00075672	0.000582099

References

- [1] Daniel J Amit and Nicolas Brunel. Dynamics of a recurrent network of spiking neurons before and following learning. *Network: Computation in Neural Systems*, 8(4):373–404, 1997.
- [2] Daniel J Amit and Nicolas Brunel. Model of global spontaneous activity and local structured activity during delay periods in the cerebral cortex. *Cerebral cortex (New York, NY: 1991)*, 7(3):237–252, 1997.
- [3] Michael Breakspear. Dynamic models of large-scale brain activity. *Nature neuroscience*, 20(3):340–352, 2017.
- [4] Sarthak Chandra, David Hathcock, Kimberly Crain, Thomas M. Antonsen, Michelle Girvan, and Edward Ott. Modeling the network dynamics of pulse-coupled neurons. *Chaos: An Interdisciplinary Journal of Nonlinear Science*, 27(3):033102, March 2017.
- [5] S. Coombes and M. R. Owen. Bumps, breathers, and waves in a neural network with wpike frequency adaptation. *Physical Review Letters*, 94(14):148102, apr 2005.
- [6] Stephen Coombes. Waves, bumps, and patterns in neural field theories. *Biological cybernetics*, 93(2):91–108, 2005.
- [7] Stephen Coombes and Áine Byrne. Next generation neural mass models. *arXiv preprint arXiv:1607.06251*, 2016.
- [8] Peter Dayan, LF Abbott, et al. Theoretical neuroscience: computational and mathematical modeling of neural systems. *Journal of Cognitive Neuroscience*, 15(1):154–155, 2003.
- [9] Bard Ermentrout. *Simulating, analyzing, and animating dynamical systems: a guide to XPPAUT for researchers and students*. SIAM, 2002.
- [10] G Bard Ermentrout and David H Terman. *Mathematical foundations of neuroscience*, volume 35. Springer Science & Business Media, 2010.
- [11] George Bard Ermentrout and Nancy Kopell. Frequency plateaus in a chain of weakly coupled oscillators, I. *SIAM Journal on Mathematical Analysis*, 15(2):215–237, 1984.
- [12] Stefanos E Folias and Paul C. Bressloff. Breathers in two-dimensional neural media. *Physical Review Letters*, 95(20):208107, nov 2005.
- [13] Eric Jones, Travis Oliphant, Pearu Peterson, et al. SciPy: Open source scientific tools for Python, 2001–.

- [14] James P Keener. *Principles of applied mathematics*. Addison-Wesley, 1988.
- [15] D Kleinfeld, F Raccuia-Behling, and HJ Chiel. Circuits constructed from identified aplysia neurons exhibit multiple patterns of persistent activity. *Biophysical journal*, 57(4):697–715, 1990.
- [16] Hiroshi Kori, Yoji Kawamura, Hiroya Nakao, Kensuke Arai, and Yoshiki Kuramoto. Collective-phase description of coupled oscillators with general network structure. *Physical Review E*, 80(3):036207, 2009.
- [17] Yoshiki Kuramoto and Ikuko Nishikawa. Statistical macrodynamics of large dynamical systems. case of a phase transition in oscillator communities. *Journal of Statistical Physics*, 49(3):569–605, Nov 1987.
- [18] C. Laing. Exact Neural Fields Incorporating Gap Junctions. *SIAM Journal on Applied Dynamical Systems*, 14(4):1899–1929, January 2015.
- [19] Carlo R Laing. Derivation of a neural field model from a network of theta neurons. *Physical Review E*, 90(1):010901, 2014.
- [20] Carlo R. Laing. The dynamics of networks of identical theta neurons. *The Journal of Mathematical Neuroscience*, 8(1):4, Feb 2018.
- [21] Ernest Montbrió, Diego Pazó, and Alex Roxin. Macroscopic Description for Networks of Spiking Neurons. *Physical Review X*, 5(2):021028, June 2015.
- [22] Ken H Nagai and Hiroshi Kori. Noise-induced synchronization of a large population of globally coupled nonidentical oscillators. *Physical Review E*, 81(6):065202, 2010.
- [23] Edward Ott and Thomas M Antonsen. Low dimensional behavior of large systems of globally coupled oscillators. *Chaos: An Interdisciplinary Journal of Nonlinear Science*, 18(3):037113, 2008.
- [24] Edward Ott and Thomas M. Antonsen. Long time evolution of phase oscillator systems. *Chaos: An Interdisciplinary Journal of Nonlinear Science*, 19(2):023117, May 2009.
- [25] Diego Pazó and Ernest Montbrió. Low-dimensional dynamics of populations of pulse-coupled oscillators. *Physical Review X*, 4(1):011009, 2014.
- [26] Alfonso Renart, Rubén Moreno-Bote, Xiao-Jing Wang, and Néstor Parga. Mean-driven and fluctuation-driven persistent activity in recurrent networks. *Neural computation*, 19(1):1–46, 2007.

- [27] Javier Roulet and Gabriel B. Mindlin. Average activity of excitatory and inhibitory neural populations. *Chaos: An Interdisciplinary Journal of Nonlinear Science*, 26(9):093104, September 2016.
- [28] Jonathan J. Rubin, Jonathan E. Rubin, and G. Bard Ermentrout. Analysis of synchronization in a slowly changing environment: How slow coupling becomes fast weak coupling. *Physical Review Letters*, 110:204101, May 2013.
- [29] Paul So, Bernard C Cotton, and Ernest Barreto. Synchronization in interacting populations of heterogeneous oscillators with time-varying coupling. *Chaos: An Interdisciplinary Journal of Nonlinear Science*, 18(3):037114, 2008.
- [30] RD Traub. Simulation of intrinsic bursting in ca3 hippocampal neurons. *Neuroscience*, 7(5):1233–1242, 1982.
- [31] Xiao-Jing Wang and György Buzsáki. Gamma oscillation by synaptic inhibition in a hippocampal interneuronal network model. *Journal of neuroscience*, 16(20):6402–6413, 1996.
- [32] Shinya Watanabe and Steven H Strogatz. Integrability of a globally coupled oscillator array. *Physical review letters*, 70(16):2391, 1993.
- [33] Shinya Watanabe and Steven H Strogatz. Constants of motion for superconducting josephson arrays. *Physica D: Nonlinear Phenomena*, 74(3-4):197–253, 1994.